PhD thesis

Presented at the Department of Process Engineering

For obtaining the degree of

DOCTORAT

Domain: Sciences and Technology

Stream: Process Engineering   **Specialty: Chemical engineering**

By

Oualid ALIOUI

TITLE

EXPERIMENTAL AND THEORETICAL ANALYSIS OF DRY METHANE REFORMING:

IN-SILICO FORMULATION OF ACTIVE CATALYSTS

Presented publicly on   17/07 /2023 , Jury:

Mohamed Tahar BENANIBA	**Professor**	**Univ. Ferhat Abbas Sétif 1**	**President**
Yacine BENGUERBA	**Professor**	**Univ. Ferhat Abbas Sétif 1**	**Supervisor**
Mirella VIRGINIE	**M.C.A**	**Univ. Lille-1**	**Co-supervisor**
Embarek BENTOUHAMI	**Professor**	**Univ. Ferhat Abbas Sétif 1**	**Examiner**
Slimane MEROUANI	**Professor**	**Univ. Constantine 3**	**Examiner**

Abstract

Carbon dioxide and methane are known as the two largest greenhouse gases (GHG) responsible for climate change and temperatures rise. Dry reforming of methane (DRM) is a chemical process that allows reducing CH_4 and CO_2 emissions into the atmosphere and converts them into a valuable syngas containing CO and H_2. Recently, DFT calculations have been increasingly used to provide more insights into the DRM process to open new and better ways to control existing reactions, to obtain additional information on specific aspects of the catalytic process and to deliver practical strategies for rational *in silico* catalyst design. This thesis discusses the role of DFT in the DRM process and the recent research accomplished, including the reaction mechanism, coke formation, metal sintering and metal support interactions. Combining the experimental and DFT approach, we have found that adding a small amount of cobalt (1:10) to Ni/Al_2O_3 catalyst has a significant impact in improving the stability and catalyst performances by avoiding metal sintering and carbon deposition as well as enhance the H_2 selectivity.

Keywords: Greenhouse gas; Dry reforming of methane; Ni-based catalyst; Methane dissociation; Density functional theory.

الملخص

يُعرف ثاني أكسيد الكربون والميثان بأنهما أكبر غازين من غازات الاحتباس الحراري المسؤولة عن تغير المناخ وارتفاع درجات الحرارة. إعادة التكوين الجاف للميثان (DRM) هي عملية كيميائية تسمح بتقليل انبعاثات الميثان وثاني أكسيد الكربون في الغلاف الجوي وتحويلها إلى غاز تقيم يحتوي على أحادي أكسيد الكربون وغاز الهيدروجين. في الآونة الأخيرة ، تم استخدام حسابات DFT بشكل متزايد لتوفير المزيد من الأفكار حول عملية DRM لفتح طرق جديدة وأفضل للتحكم في التفاعلات الحالية ، للحصول على معلومات إضافية حول جوانب محددة من العملية التحفيزية ولتقديم استراتيجيات عملية لعقلانية في تصميم محفز محاكى. تناقش هذه الأطروحة دور DFT في عملية DRM والبحث الأخير الذي تم إنجازه ، بما في ذلك آلية التفاعل وتكوين فحم الكوك وتلبيد المعادن وتفاعلات دعم المعادن. من خلال الجمع بين النهج التجريبي ونهج DFT ، وجدنا أن إضافة كمية صغيرة من الكوبالت (1:10) إلى محفز Ni / Al$_2$O$_3$ له تأثير كبير في تحسين الاستقرار وأداء المحفز عن طريق تجنب تلبيد المعادن وتعزيز الانتقائية.

الكلمات المفتاحية: غازات الاحتباس الحراري ؛ إصلاح الميثان الجاف محفز قائم على النيكل ؛ تفكك الميثان نظرية الكثافة الوظيفية.

Acknowledgments

Table of Contents

CHAPTER I: Overview on dry reforming of methane

CHAPTER II: Density functional theory (DFT)

CHAPTER III: Alumina support and Ni nano-clusters

CHAPTER IV: Experimental and DFT calculation work

List of figures

List of tables

Introduction

Introduction

Fossil fuels are currently the main energy source in the world which contribute the global economic development during the last decades. However, due to the rapid growth of world population, energy demand is expected to increase by 2030 to achieve 57% [1-3]. Yet fossil fuels are limited sources of energy, and their widespread use can significantly cause irreparable harm to the environment and human health. According to the recent statistics report from the International Energy Agency (IEA) [4] the global CO_2 emission resulting from fuel burning attained an historical high in 2018 by 33.5 $GtCO_2$, whereas it has slightly decreased with less than 1% in 2019. This gas is known as the greenhouse gas GHG and is the major cause responsible for global warming phenomenon which can also cause a catastrophic change in the Earth's climate. Thus, finding alternative energy sources that ensure the stability of industrial and economic activities as well as improve the quality of life without endangering the environmental and human health is considered as a serious challenge facing both industrial and scientific communities at present[5-7].

To this aim, among emerging renewable energy sources, biomass and hydrogen can significantly contribute in reducing the greenhouse gases (GHGs) emission rates [8].

Biogas is a renewable energy source that is generated by anaerobic digestion of organic materials (biomass) such as food waste, dung, sewage sludge, forestry and agricultural residues in the absence of oxygen, which makes its exploitation financially and environmentally beneficial [6, 9, 10]. This type of energy obtained from a biomass source is largely subsidized by governments to avoid the massive use of crops for energy production [11]. The main components of biogas are carbon dioxide (CO_2) and methane (CH_4), whose concentrations range from 50% to 75% and 25% to 50% by vol.,

respectively, in addition to some traces of water, hydrogen sulfide (H_2S), halogens and ammonia [9].Recently, many efforts are being made to convert carbon dioxide as an alternative fuel source to different chemical products and materials such as methanol, ethanol, carbon fiber and dimethyl carbonate [12].

Methane, the main component of biogas and natural gas, is considered as one of the most dangerous greenhouse gases with a much higher global warming potential than carbon dioxide [13].

One of the reliable ways to mitigate this problem is to convert these gases (CH_4 and CO_2) into syngas (H_2 and CO) using different techniques and processes such as dry reforming (CO_2), steam reforming (H_2O), partial oxidation, autothermal, and membrane reforming to produce chemicals and fuel products further. Reforming techniques differ in many parameters, such as the oxidant used, the H_2/CO ratio obtained and the involved reaction energies.

The steam reforming process yields a high hydrogen production with a molar ratio of 3:1 (H_2: CO), which can be further used to synthesize other required products such as methanol and ammonia. Another emerging methane reforming technique is mixed reforming, which adopts various combinations and ratios of O_2, H_2O, and CO_2 to control the H_2/CO ratio in the product stream [14].

Among these methods, steam and dry reforming processes performed in presence of nickel-based catalysts are essential techniques that are proposed to mitigate greenhouse gas emissions and produce synthesis gases [13]. Dry reforming of methane (DRM) is an attractive and environmentally friendly process for energy vectors production. It allows reducing the emissions of CH_4 and CO_2 by converting them into CO and H_2 (syngas) with

an H_2/CO molar ratio close to 1 suitable for chemical processes such as the Fisher-Tropsch synthesis to generate different hydrocarbon products [15, 16].

On the other hand, a thorough comprehension of the detailed reaction mechanism occurring in the catalytic process is still lacking. Contextually, the adoption of computational modelling methods such as density functional theory (DFT) represents an emerging area of investigation to gain deeper insights in complex reaction processes at the molecular scale.

In this context, the present work aims to discuss the results obtained on Ni-based catalysts for dry reforming of methane (DRM) process combining the experimental and DFT tool to better describe and understand the catalytic DRM process. The overviews of DRM and DFT are first presented in chapter 1. Subsequently, the detailed reaction mechanism of DRM using DFT is discussed in terms of energy, together with other catalyst issues such as the rate limiting steps, the transition states of the elementary reactions, coke formation, sintering, and metal-support interaction in the chapter 2. In chapter 3 we have presented detailed structural properties of the alumina since it plays a critical role in the catalytic process. Then, we presented the experimental and theoretical methodology and discussed the obtained results in Chapter 4, And finally, we summed up with conclusion and perspectives. The results presented in this work provide insights into the catalyst design combining the experimental and the DFT approach and open new pathways towards the development of DRM catalysts.

Chapter I

Overview on dry reforming of methane

I. Overview on dry reforming of methane

DRM is an endothermic process that requires high-temperature conditions to reach the reaction equilibrium and consequently high conversion levels, generally between 600°C and 900°C, and a molar ratio of CH_4/CO_2 in the feed varying from 1 to 1.5 to obtain about 50% of H_2 production [17]. The reaction governing DRM is:

$$CH_4(g) + CO_2(g) \leftrightarrow 2CO(g) + 2H_2(g) \qquad \Delta H_{298K} = +247 \text{ kJ mol}^{-1} \qquad (1.1)$$
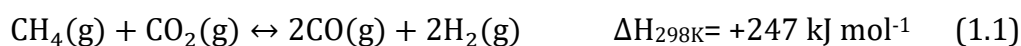
Despite the environmental advantages of DRM, the quick catalyst deactivation by coke deposition resulting from both methane dissociation (2.1) and Boudouard reaction (3.1) remains the major problem for this process [18]

$$CH_4(g) \leftrightarrow C(s) + 2H_2(g) \qquad \Delta H_{298} = +74.9 \text{ kJ mol}^{-1} \quad (2.1)$$

$$2CO(g) \leftrightarrow CO_2(g) + C(s) \qquad \Delta H_{298} = -172.5 \text{ kJ mol}^{-1} \quad (3.1)$$

The DRM reaction could be simultaneously accompanied by the methanation reaction (4.1) and reverse water-gas shift reaction (RWGS) (5.1)

$$CO_2(g) + 4H_2(g) \leftrightarrow CH_4(g) + 2H_2O(g) \quad \Delta H_{298} = +165.0 \text{ kJ. mol}^{-1} \qquad (4.1)$$

$$CO(g) + H_2O(g) \leftrightarrow CO_2(g) + H_2(g) \qquad \Delta H_{298} = +41.0 \text{ kJ. mol}^{-1} \quad (5.1)$$
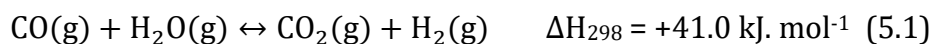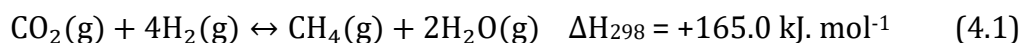
The use of a catalyst for DRM process is necessary to reduce the high kinetic energy barrier of the process so to achieve the desired methane and carbon dioxide conversion and H_2 yield. Several types of catalysts have been studied in the literature for the DRM process, such as noble metals, transition metals, spinels, perovskites (BaZr (1-x) MexO₃), hydrotalcite, and metals basic supported [19, 20]. However, catalyst deactivation at high temperatures via coke deposition and particles sintering remains the main problem for DRM process, which causes an active site blockage leading to pore blockage of catalyst

and reactor, respectively [16]. Recently, many efforts and strategies have been developed to design high-performance catalysts that can tolerate carbon deposition at low temperatures [9].

I.1. Effect of metal

Noble metals such as Ru, Rh, Pt, Pd, and Ir showed a high activity towards the DRM process and a higher carbon deposition resistance compared to the other metals. However, the prohibitive cost remains the leading cause of the limited use of these metals [14, 18]. The strategy of promotion, which consists of adding a metal promoter to the different metal-based catalysts to form a bimetallic catalyst, represents one of the possible solutions that has turned out to be an efficient technique to enable high catalyst performance and to reduce the coke formation. Thus, noble metals can be used in limited amounts (with associated economic advantages) as promotors of non-noble metals (Co, Ni, Cu, Fe), which helps to enhance their catalytic performance by increasing their stability, particle dispersion and provide the additional active sites, thus determining high reaction rates [21]. Furthermore, because of their cost-effectiveness, non-noble metals have also been investigated as promoters of non-noble metal-based catalysts, and they exhibited a similar activity of noble metal-based catalysts. However, the rapid deactivation due to the carbon deposition and metal sintering remains the central issue [18].

In addition, it is known that the activity and stability of catalysts are affected by the dimension of Ni particles [22]. Some authors [23-26] analyzed the relationship between the catalyst particle size and the amount of carbon deposited. The results showed that the large-sized nickel particles, which are resulting from the metal aggregation, could

enhance the coke deposition and decrease the catalyst activity to a larger extent when compared to finer catalysts particles.

I.2. Effect of support

Recently, a wide range of supports and their influence on catalytic activity has also been investigated [27-30], in order to obtain nanometric dispersed particles with high catalytic activity and stability, also reducing the aforementioned coke deposition and sintering issues [31]. The chemico-physical and porosimetric properties of the support material can significantly influence the catalyst characteristics in terms of acid-base properties, particles dispersion and metal-support interactions [30, 32].

The high surface area and highly porous nature provided by the support can enhance the dispersion and reduce the size of the dispersed active metal particles. In this context, Therdthianwong et al. [33] investigated the use of Ni/Al_2O_3 stabilized by ZrO_2 for the DRM process. They found that the supported Ni particles on Al_2O_3 exhibit a small size compared to those supported on ZrO_2, where they observed a larger particles size. Furthermore, by adding a high amount of ZrO_2 (15%) to the Al_2O_3 support, the dispersion of Ni particles decreases. However, a small amount of ZrO_2 (5%) leads to high dispersion of Ni particles. These results lead to conclude that the large surface area of Al_2O_3 and ZrO_2 (5%)/ Al_2O_3 enhance the high dispersion of Ni particles, and thus, reduce their size. On the contrary, the low surface area of ZrO_2 and of ZrO_2 (15%)/Al_2O_3 composite causes the agglomeration of Ni particles and increases their size.

Moreover, the authors reported that the stabilized Ni/Al_2O_3 by a small amount of ZrO_2 not only exhibits a high dispersion of Ni particles but also yields to a high $CO:H_2$ ratio and a coke resistance by enhancing the dissociation of CO_2, which generates oxygen that reacts with the deposited carbon to form CO.

Also, the support exhibits different physicochemical properties such as oxygen storage capacity, basicity (CaO, MgO, and La_2O_3), and reducibility (CeO_2 and ZrO_2), which influence their intrinsic behavior in catalytic reactions, on the formation of coke. Carbon atoms can diffuse in the presence of a reduced number of oxygen atoms on the support surface, to promote the coke formation or interact with external carbon to form graphene islands. Thus, various metals and oxides such as CeO_2, ZrO_2, and TiO_2 have been investigated to increase the amount of surface oxygen atoms, which can reduce the coke formation by converting the deposited carbon to carbon monoxide CO [18, 34, 35].

Additionally, in their published papers on the use of MgO-Ni/ZrO_2 and Ni-based catalysts, respectively, García et al. and Özdemir [36, 37] observed that increasing the basicity of the catalysts fosters the RWGS and reverse Boudouard reactions, which also lead to carbon oxidation and thus avoid the catalyst deactivation by coke [38].

Strong metal-support interaction (SMSI)[39], which was initially explained as a transfer of electrons between the support and the active metal [31], can play an essential role in enhancing the reducibility of the catalyst and obtain highly dispersed active metal sites.

In the case of Ni monometallic catalyst, surface particles were oxidized and covered with a monolayer of Ni^{2+} ions due to the presence of oxygen, which showed a low activity towards methane reforming [8, 40]. Turlier et al. [41] reported that the nature of the support strongly affects the reducibility of the active metal also by acting as promoters in the case of CeO_2 and ThO_2. This effect may be related to different factors such as the size of the Ni^{2+} precursor particles, back spillover of hydrogen which can act as Ni^{2+} reducing agent after its activation over the support into atomic hydrogen, and also the basicity of the support that can trap protons, thus promoting the reduction of nickel (II) ions:

$$Ni^{2+} + H_2 \leftrightarrow 2H^+ + Ni^0 \qquad (6.1)$$
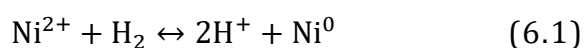
Furthermore, it is worth to mention that the synthesis method [27, 42], pre-treatment and calcination temperature [43], metal content [44], and the molar feed ratio [45] have a significant effect on the DRM process.

For an overview of the different nickel-based catalysts used in DRM, we summarize in the table below (Table 1) the recent catalysts applied in this field with different preparation methods, temperature of the reactions, conversion results of the reactants and the stability obtained.

Table 1. Most recent catalysts used in DRM.

Catalyst	Metal Loading (%wt.)	Preparation method	T(°C)	Notes	CO_2 conversion (%)	CH_4 conversion (%)	Stability (h)	ref
Ni-Mo/MgO	10%Ni 2% Mo	Wet impregnation	800	Adding Mo improves conversion yields of the catalyst, even though Mo is not active for DRM	80	75	500	[46]
Ni/La$_2$O$_3$-MgAl$_2$O$_4$	10%Ni	Modified incipient wetness	DBD plasma	La$_2$O$_3$ was added to improve the basicity of the mixed-matrix support since La$_2$O$_3$ is a strong basic oxide	83	82	/	[47]
Ni/SiO$_2$	5%Ni	Impregnation	600	Strong metal-support interaction and high resistance for coke	53	51	100	[48]
Ni-Co/MgO	8%Ni, 2%Co	Incipient wetness impregnation	750	Adding Co to Ni enhances the oxidation of surface carbon and reduce carbon deposition	91 / 89	85 / 83	48	[49]
Ni/CeZrO$_2$	4%Ni	Incipient wetness impregnation	700	Adding Zr exhibits significantly improved catalyst activity and H$_2$ selectivity	66	51	/	[50]
Ni/CeO$_2$	4%Ni		750	CeO$_2$ anchores and activates metal phase with high chemical	44	28	/	
Ni-CeO$_2$	5.5%Ni	Impregnation		High surface area and porous structure of CeO$_2$ flowers leads to	90	92	200	[51]
Ni-Fe/Al$_2$O$_3$	9.6%Ni, 4.2%Fe	mEISA method + microwave treatment and EISA process	550	The addition of Fe improves CH$_4$ and CO$_2$ conversion as well as H$_2$/CO ratio	31 / 38	22 / 87	20	[52]
Ni/Al$_2$O$_3$	15.7%Ni		800	High surface area and porosity of Al$_2$O$_3$	85	80	20	
Ni-Co/CeO$_2$	10%Ni,	Incipient wetness	700	Co promoted the adsorption of surface oxygen enhances stability			10	
Ni/DFSBA-	10%Ni	Ultrasonicated	700	High catalytic activity performance and less coke deposition	96	94	30	
Ni/Al$_2$O$_3$	6%Ni	Incipient wetness impregnation	750	Confined spaces on Al$_2$O$_3$ and steady chemisorption behavior	90	93	10	[55]
Ni/HAP	4.5%Ni	Urea-hydrolysis precipitation	750	Hydroxyapatite (HAP) presents macropores which enhance the mass transfer of reactants and products, whereas mesopores	63	56	12	[56]
Ni/MFI	N/A	Wetness impregnation	800	MFI inclinations to high dispersion and stabilization of metal particles	75	70	30	[57]
Ni-La$_2$O$_3$/SiO$_2$	N/A	One-pot colloidal solution	700	Abundant interface between Ni and La$_2$O$_3$ Good resistance to carbon deposition	90	85	50	[58]

9

Chapter II

Density functional theory (DFT) application in DRM

II.1. Insights on density functional theory (DFT)

Due to the several pathway reactions involved in DRM, although many studies have been performed in the last decades, the process remains complicated and challenging to understand. Therefore, the exploration of the reaction mechanism using computational methods such as kinetic modelling and density functional theory (DFT) can provide further insights on the process mechanism and gives additional information, which can help to develop useful strategies for the in silico design of high performance catalysts with reduced issues related to poisoning and sintering phenomena [59].

In this regard, several publications and kinetic models have been discussed in the literature to describe the reaction mechanism of the DRM process [8, 40, 60]. Recently, computational chemistry has evolved into one of the critical components of catalysis science, placing itself alongside experimental work in the field of catalysis. Microkinetic modelling and molecular simulations using DFT density functional theory have significantly contributed to improve the fundamental understanding of heterogeneous catalytic processes and their elementary stages and mechanisms at the atomic level by predicting several properties that directly related to the catalytic activity such as activation energy, adsorption energy, determination of the reaction's rate-limiting step using transition states of elementary reaction as well as the mechanism of formation of by-products [61-64].

DFT was first formalized (in 1964) by Hohenberg & Kohn (H-K)[65]. The fundamental theory of DFT is that the system's ground-state properties are assumed to be a particular feature of the electron density, implying that there is no need to quantify the system's complete multi-body wave function. The precise functional dependence of the energy on the density is unclear, though.

Subsequently, Kohn–Sham (1965) developed the H-K equations[66]. These equations consist of Schrödinger-like three-dimensional (one-electron) equations with modified effective potential that are simple to solve compared to the original multi-body problem. The adjusted potential is identical to that of the modified potential being the same as the total particle density function, and it involves a contribution from the particles' quantum-mechanical interaction and correlation. Nonetheless, no expression can explain this potential for exchange-correlation (XC) energy. Still, the fractional error caused by its approximation is minimal relative to the single-particle kinetic and Coulomb terms. The XC concept remains relevant and cannot be trivial because it is key to the achievements of the DFT.

The differences of chemical reactions energy, bonding and adsorption energies are small, which makes the choice of XC approximations that gives a chemical accuracy, among those available (e.g., LDA, GGA, HF, B3LYP and many more), a constant challenge. The construction of in-silico catalysts using electronic-structure calculations remains a longstanding goal for theoretical materials science. DFT calculations have shown useful insights in the field of the catalytic activity of different transition-metal surfaces for several reactions.

Recently, various attempts were made using DFT to obtain linear correlations between different descriptors, such as adsorption energy, the energy-barrier of reactions, atomic binding energy, preference site for adsorption, etc. Accuracy in describing the quantum nature of matter and an intricate many-body system using XC functional, and adopting electron density as a single particle formalism, is the main reason behind the success of DFT [67]. For an update overview and more specific details on different DFT functionals currently used in computational chemistry, the reader is invited to consult the following reviews [68-71].

In the following section, we will underline some of the key advances that construct the modern DFT to further gain insights and understand both the foundations and limitations of the theory.

II.2. Approximating correlation and exchange

It is obvious that the formal definition of XC energy is not helpful to solve practical issues, and hence the need for an approximation of this quantity is essential.

The differences of chemical reactions energy, bonding and adsorption energies are small, which makes the choice of XC approximations that gives a chemical accuracy, among those available (e.g., LDA, GGA, HF, B3LYP and many more), a constant challenge. The construction of in-silico catalysts using electronic-structure calculations remains a longstanding goal for theoretical materials science. DFT calculations have shown useful insights in the field of the catalytic activity of different transition-metal surfaces for several reactions.

Recently, various attempts were made using DFT to obtain linear correlations between different descriptors, such as adsorption energy, the energy-barrier of reactions, atomic binding energy, preference site for adsorption, etc.

Accuracy in describing the quantum nature of matter and an intricate many-body system using XC functional, and adopting electron density as a single particle formalism, is the main reason behind the success of DFT [67].

In this section, we will underline some of the key advances that construct the modern DFT to further gain insights and understand both the foundations and limitations of the theory.

II.2.1. Local-Density Approximation (LDA)

The Local-Density Approximation (LDA) is the basis of all approximate exchange-correlation functionals. It was firstly proposed by Dirac in 1930[72], it is one of the most

standard and famous approximation for the exchange-correlation interaction. The assumption in this functional suggests that the exchange-correlation energy of the system is the same as that of one homogenous electron gas with the density n(r). this relationship is described as following:

$$E_{xc}[n] = \int n(r) \, \varepsilon_{xc}^{hom} [n(r)] dr \quad (1.2)$$

Where ε_{xc}^{hom} represent the exchange-correlation energy per electron of a homogeneous electron gas of density (n). LDA approximation is sufficient for a system with a low spatial varying electron density and further for several varieties of materials. However, for the calculation of d and f compounds properties and binding energies estimation, the description using LDA still needs to improvements and its errors are larger than the absolute values of the correlation energies of atoms [73]. In this field, many developments have been proposed by Wang [74] and Voskoet[75].

II.2.2. Generalized Gradient Approximation (GGA)

The improvements series mad by Wang et al. [76, 77] and becke[78] on LDA approximation by including a term that depends on the gradient corrections of electron density led to the emergence of Generalized Gradient Approximation (GGA) on exchange-correlation approximations as a useful functional that can satisfy different known exact hole constrains[79, 80]. It has been reported[80] that the GGA can significantly improves on the LDA approximation and reduces three times the typical energy errors (Figure1). GGAs have also been improved for correlation. The alternative method is to construct a correlation energy functional by modelling the correlation hole[81]. The GGA is currently being applied to calculate structural and electronic properties for a large number of atoms and molecules [82-86]and the obtained results look promising.
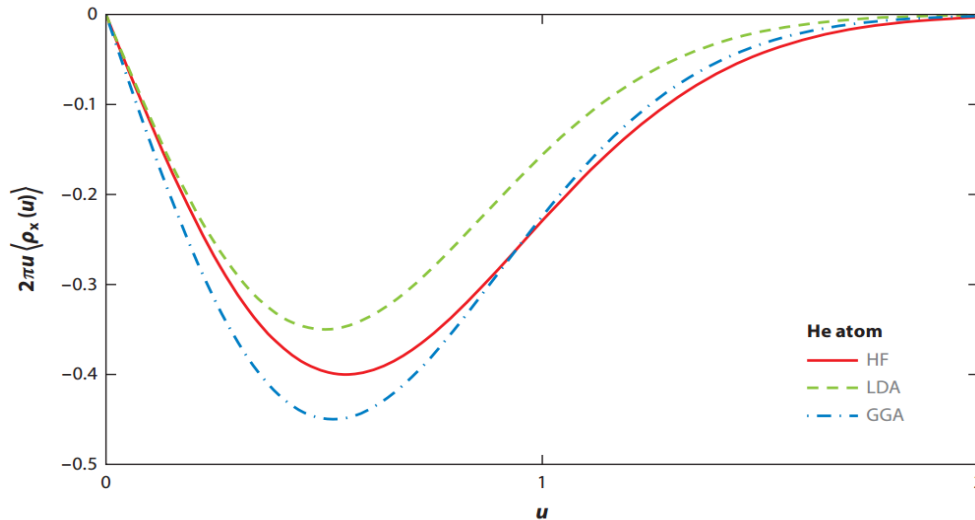
Figure 1.Comparison between GGA, LDA and HF functionals (system-averaged radial exchange holes for the He atom) [58].

Perdew-Burke-Ernzerhof functional (PBE-GGA)[87] which represents the nonempirical GGA approximation is considered as the most common exchange-correlation functional. It is recommended specially to investigate molecule-metal surface interaction; however, it showed a good accuracy in predicting some molecular systems properties such as electron affinity, ionization potential and bond distances[88]. Moreover, The results obtained using this functional in theoretical investigations showed that the PBE provides total energy dependent properties in agreement with the experimental results[87, 89]. However, comparing the PBE functional to other empirical functionals it has been found that PBE yields large errors in the prediction of reaction barrier and atomization energy[90]. Another frequently used GGA functional is PW91[91]. This approximation was developed by the same author, combines both exchange and correlation functionals and gives similar values for exchange energy as PBE in the case where the density is neither too small nor too rapidly changed. As the same, B88 functional designed by A.D. Becke [92] in order to reduce the gradient expansion approximation form (GEA) in the limit of small gradients. The B88 functional has one empirical parameter that is fitted to Hartree-Fock (HF) exchange energies for the noble gas atoms.

II.2.3. *Hybrid functionals approximation*

Hybrid functions are created by mixing a part of exact-exchange (from HF theory) into a semi-local exchange functional and combining it with a semi-local correlation functional. This idea was first proposed by A.D. Becke [93] in order to improve the calculations of many molecular properties such as vibration frequencies and atomization energies that have been poorly described by classical functionals. The most popular and widely used hybrid functional is Becke 3-Parameter, (B3LYP)[94] which uses both B88 exchange and LYP correlation functionals. The reason for the success of this functional is the good compromise between computational cost , coverage, and accuracy results[95]. Other hybrid functionals such as PBE_0[96], HSE(Heyd–Scuseria–Ernzerhof)[97], Meta-Hybrid GGA[98] are also emerged besides 200 functionals approximation for DFT XC.

For an update overview and more specific details on different DFT functionals currently used in computational chemistry, the reader is invited to consult the following reviews[68-71].

II.3. Key descriptors at the DFT level

One of the main factors that makes DFT a useful approach to understand the catalytic phenomena is the emergence of descriptor concept. A descriptor is one of catalytic system properties which is linked to the catalyst activity performance. This concept is based on the search of a suitable microscopic property that allows to make a qualitative prediction to a given system and a rapid screening of potential catalysts, which can help to better understand the changes occurring at the mechanistic level, and thus, lead to develop and design new catalysts with heigh catalytic performance [99-101]. Thus, finding a suitable descriptor by taking into consideration the thermodynamics and kinetics parameters will be helpful to simplify the complicity of various reaction mechanisms and into the catalyst

design and development. Therefore, finding descriptors to study any reaction has become a crucial step in theoretical investigations. Descriptor-based catalyst has been used on a large scale in the last decade [102-105].

II.3.1. Descriptors of catalytic activity

Typically, descriptor-based approaches have been used to obtain the catalytic trends of many vital reactions. Recent studies[104, 106] have successfully arrived to design new transition metal based-catalysts with superior activity performance and even comparable or better then noble based-catalysts using the concept of descriptor-based approach. The choice of the best descriptor to predict the catalyst behavior significantly depends on which catalyst property has a significant impact on the catalytic activity. However, when the number of descriptors is relatively high (e.g. in the case of the existence of more than two important reactions) or there is no clear idea about the system mechanism, the use of semi-empirical methods to determine the optimal descriptor such as QSAR, Neural network[107], and SISSO method[108] is necessary[109, 110]. Several descriptors have been considered in the literature. Previous studies[111, 112], have demonstrated that the oxygen vacancy formation energy (E_{vac}) strongly related to the catalytic activity in autothermal reforming reaction of solid oxide fuel cell. It has been also reported that the oxygen vacancy formation energy can be directly correlated to the oxygen p-band center energy for considerable number of solid oxides which enables the prediction of perovskites catalytic performance towards the oxygen reduction and evolution reactions using first-principles descriptor. J. Rossmeisl et al.[113] showed that the binding energy of oxygen atoms to the Pt and Au catalyst surfaces is a good descriptor for the direct splitting of water reaction, due to the fact that binding energies of various intermediates are correlated for a number of metals.

Research groups[114-116] have used the band-gap energy which represent the difference between HOMO and LOMO to rationalize the reactivity of molecular systems, since it provides the information about the frontier molecular orbitals in crystalline materials. Moreover, based on the BEP concept [117, 118] and the reported result by Norskov et al [110], it has been found that there is an linear fit between adsorption energy and the energy barrier of the chemical reactions and the strength of interaction between the reactants species and the catalyst surface is can be described by the adsorption energy. Thus, many researchers [100, 119-121] have used the adsorption energy as a key descriptor to study the catalytic activity performance. In DRM, Koustuv Ray et al [100] have used both dissociation energy E_{diss} of CH_4 and adsorption energy E_{ads} of carbon, to study the activity and stability of Ni based alloy catalysts. Their results showed a linear correlation between turnover frequency (ToF) and (E_{diss}), and between the percentage of deactivation of catalyst and E_{ads} of carbon, respectively. Same author [99] has used the d-band center (ε_d) and d-density of states (N_{E_F}) as a protentional descriptors into CO_2 methanation and DRM reactions over Ni- based alloys catalysts to predict the activity of the used catalysts. The obtained results showed an excellent fit between N_{E_F} descriptor and ToF_{CH4} with R^2=0.96 for the CO_2 methanation reaction and R^2= 0.81 between (ε_d) descriptor and ToF_{DRM} for DRM reaction. Z. Zuo et al[122] have calculated the activation energy barriers of different intermediate reaction steps of overall DRM reaction as a key descriptor to predict the activity and selectivity of different species over Ni/MgO catalyst. Furthermore, B. Wang and his collaborators[123] have added more insights to reduce the complexity of DRM reaction mechanism network over Ni(111) and Pt(111) catalysts combining both microkinetic and DFT approaches and using formation energies (E_f) of surface species, transition states (TS) of elementary reactions, and adsorption energies (E_{ads}) of different species as a key descriptors. Their investigation allowed to identify with

high confidence the possible reaction pathways of DRM mechanism network, the surface dominate species, as well as the rate-controlling steps in the overall reaction which can further accelerate the design of future catalysts. For further overview about descriptors applied in the catalyst field, we summarize in Table 2 the main potential descriptors used to predict the physicochemical properties of different catalyst systems.

Table 2. A set of descriptors used to predict various properties of catalysts.

Catalyst	Descriptor	Predicted property	ref
Ni_3M (M = Fe, Co, Cu)	Carbon dissociation energy (E_{ads}) CH_4 dissociation energy (E_{diss})	stability of the catalysts activity of the catalysts	[100]
Ni_4/MgO (100)	Activation energy (E_a)	Conversion and selectivity	[124]
PtA3d (3d = Fe, Co,Ni, Cu)	Binding energy (E_b) Carbon Binding energy (E_b) Nitrogen Binding energy (E_b)	hydrogenation activity the thermodynamics and kinetics of the HCN synthesis process	[102] [103]
Fe, Co, Ni, Cu, Mo, Ru, Rh, Pd, Ag, W, Ir, Pt and Au	number of d-electrons, S_E, first ionization potential and atomic radius,V and M, HOMO–LUMO, energy gap, molecular volume, and mass	H_2, HO^*, N_2, CO, NO, O_2, H_2O, CO_2, NH_3 and CH_4 adsorption on metals	[125]
Au nanoparticles	work function Φ of the bare support	geometry and charge of the deposited Au cluster	[105]
Pt < FeS2 < CuFeS2 < PbS < ZnS	oxygen binding energy (E_b)	oxygen reduction reaction mechanism	[126]
$BiFeMo_2O_{12}$,$Bi_2Mo_{2.5}W_{0.5}O_{12}$,and $Bi_{1-x}/3V_{1-x}Mo_xO_4$, where 0 ≤x≤ 1)	Band-Gap Energy	Catalytic Activity for Propene Oxidation	[116]
Au, Pd, Pt TMCs; WC, W_2C, and Mo_2C AuPd	Surface Energy d-charge at the Pd sites	Catalytic Activity entropy changes and activities in the oxidation of alcohols	[127] [128]
Ag-Cu alloy catalysts	E_b of reactants, intermediates, and products	Reaction mechanism on the thin oxide layer structures and establish the reasons for the improved selectivity.	[129]

Graphene-Based Materials	$p_z$electron-based descriptors	- catalytic activity of nitrogen-, boron-, and co-doped graphene. - model of free energies of OH adsorption (ΔG_{OH}) at any site of nitrogen/ boron-doped graphene	[130]
Pt(111)	oxygen binding energy (E_b) on metal electrodes	Turnover frequency (ToF) of the oxygen reduction reaction (ORR)	[131]
Nobel and transition metals based-catalysts Ni, Rh and Pt based-catalysts	Chemisorption energy (E_Δ) structure-energy	The overall rate of the reaction -The chemisorption energies of C, O and NO -Design alloy catalysts	[132] [106]
Ni-M/Al$_2$O$_3$,(M= Fe, Cu, Co)	Total d-density of states (N_{E_F})	CO_2 methanation where step sites are preferred for catalytic activity.	[99]
	d-band center (ε_d)	DRM reaction where terrace sites are preferred	

II.4. DFT applications and current challenges

Given the tremendous development of computational power and ease of access to high-performance computing systems, it is rare to find any of the life sciences field without applying computational modelling. Thus, Molecular Dynamic simulation (MD), ab intio methods, microkinetic modelling as well as DFT have been extensively emerged [133-138]. Herein, we will highlight the most used areas for DFT including catalysis field and the challenges it faces. In this regard, since two last decades, many research groups have reported different potential applications in several fields such as prediction of reactivity indices (electronic chemical potential, electrophilicity, chemical hardness and softness …etc.) in Organic Chemistry [139], calculation of electronic properties and structure of biomolecules, in addition to typical issues of enzymes and metalloproteins in Biological and Bioinorganic Chemistry [140, 141], development of new formulation techniques and

synthesis method for polymorph and provide more insights on solvation and crystallization processes in pharmaceutical Sciences[142]. Moreover, DFT has been widely applied nowadays in the biomedical field with the hope of discovering a drug design against the novel coronavirus (Covid-19) which is considered as a global health pandemic [143-145]. In physical sciences field, DFT has also been widely used especially in solid state, condensed matter, mineralogy, and photovoltaic materials through the modelling of optoelectronic and structural properties of semiconductors [146, 147]. Furthermore, in chemical engineering and environmental sciences, the implementation of DFT has been beneficial in improving filtration techniques for fluids and gases, adsorption processes, as well as reducing the pollution of air and water [148, 149]. Otherwise, DFT has emerged as a new successful approach in geoscience areas for the last decade. The aim of using this approach is to understand the properties of minerals under Earth's pressure and temperature (360GPa and 6000K respectively) conditions since the experimental work at these conditions is extremely difficult. Thus, the DFT computations in this filed have been applied to estimate the physical parameters which are of vital importance to understand the evolution and dynamics of the Earth [150, 151]. DFT finds significantly broad application in chemistry and materials science for predicting and interpreting the behavior of complex systems at electronic level. A complementary aspect to this topic is represented in Figure 2, which shows the number of citations of the term ''Density Functional Theory '' in the last 20 years given by google scholar.
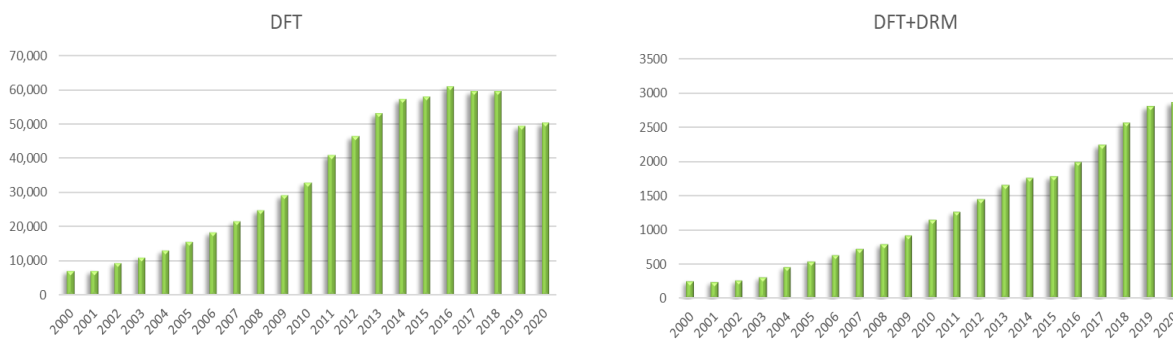
Figure 2. Number of citations of ''DFT'' and ''DFT + DRM'' per year in the last 20 years (from google scholar; access 16 december 2020).

The application of DFT in catalysis field especially in DRM process, which we will discuss in detail in the present literature review, has gained a particular importance since it has succussed to establish a good background to understand heterogeneous catalysts and provided useful information that can help in understanding which properties are the key for certain reactions to be able to design new catalysts with high performance. However, finding a new catalyst for a given reaction is only the first step in a series of necessary conditions to put the technical catalyst into the framework. Thus, the ability of the designed catalyst to be active in the realistic conditions of the reaction, its stability for an acceptable lifetime and avoidance the deactivation by carbon deposition and sintering routes, as well as its capacity to achieve a good conversion of reactants and high selectivity, remain the crucial challenge facing the *in-silico* investigation in DRM process. Hence, the intrinsic development of catalysts properties simulation as well as methodological improvement are required [152]. In the end, only experimental work can confirm the performance of the designed catalyst.

Nowadays, many codes [153-155], [156] [157] [158, 159], employ DFT to simulate the properties of solids, interfaces, adsorption energies and reactions mechanism. Within DFT, it is possible to investigate catalytic systems at the molecular scale, which general trends and concepts can be extracted [160].

II.5. Dissociation mechanisms of dry reforming of methane

Dry reforming of methane (DRM) is a process that involves the dissociation of methane (CH_4) and carbon dioxide (CO_2). These two critical steps have been examined on several catalytic metallic surfaces [161]. Moreover, other parallel phenomena occur during DRM. All these reactions are detailed at atomic level, focusing on the dissociation mechanisms and bounds involved, in the following.

II.5.1. CH_4 dissociation

Methane is a stable molecule due to its high C-H binding energy and its strictly symmetrical structure [162]. Thus, activation and dissociation of CH_4 are the most energetically demanding steps in the DRM process. Furthermore, recent literature [163-165] has reported that the activation of methane is the rate-determining step in the DRM process. Therefore, the dissociation of CH_4 to CH_X (x = 0–3) and H over different catalysts was firstly calculated step by step, based on the stable adsorption configurations of the possible species.

The DFT calculations on the adsorption and dissociation properties reveal that the nature of the support has a significant impact on the surface interactions between the catalyst and the adsorbed CH_4 molecules. In fact, the support can modify both the electronic distributions at the surface and the local surface chemical environment, such as the formation of oxygen or hydroxy (OH) vacancies, which can affect the surface chemistry and activity of the DRM process as well as determine the pathway of the CH_4 dissociation mechanism on different catalysts.

Li et al. [166] have studied the adsorption and dissociation mechanism of CH_4 by DFT on both spinel and non-spinal Ni_4 clusters supported on Al_2O_3 (100). Their results confirmed the physisorption nature of CH_4 onto the catalyst [159, 167, 168]. They indicated that CH_4

preferentially absorbs and dissociates at the metal-support interface of both the catalysts, since these steps are characterized by fast rates. At the same time, the transition state (TS) analysis (Figure.3) showed that the final configuration, as the more energetically stable, is represented by the adsorption of the methyl fragment (CH_3) on the metal-support interface (Ni_2) and the H atom on the neighbor bridge site. Adsorption results showed that the adsorption of CH_3 and H occurs at the metal-support interface of S(Ni_4) and NS (Ni_4) clusters due to the stabilized site by Al (donor)− Ni–adsorbates (acceptor) complex formation.

A: Ni_4/γ-Al_2O_3 Spinel model

B: Ni_4/γ-Al_2O_3 Non-spinel model
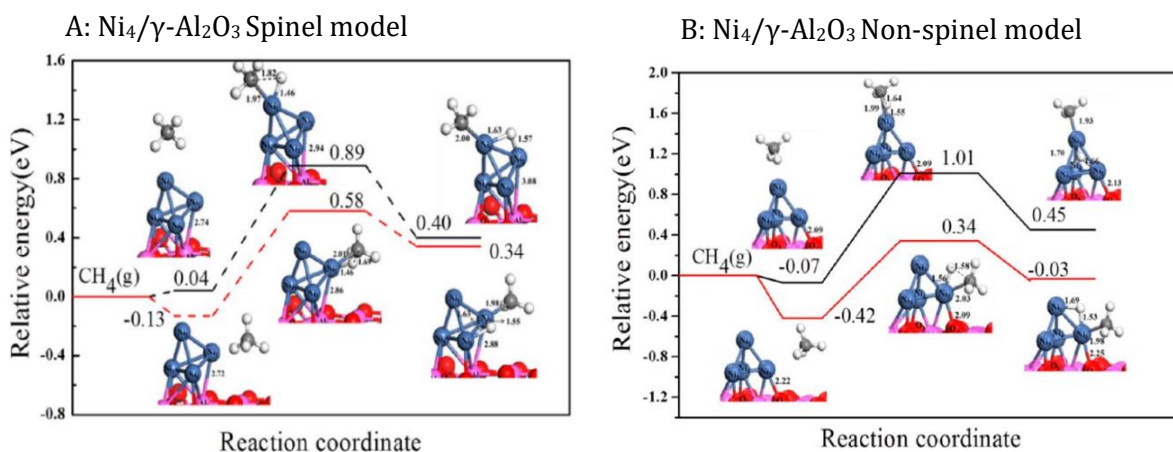
Figure 3. Potential energy profile and geometric structures of the initial state (I.S), transition state (T.S), and final state (F.S) for CH_4 dissociation over both spinel (A) and non-spinel (B) Ni_4/γ-Al_2O_3 (100) surface model. Dark blue (Ni), gray (C), white (H) [166].

Jiang et al. [169] studied the reaction mechanism of DRM over the NiO-MgO catalyst and confirmed the physisorption nature of methane adsorption process. It is further found that the CH_3 and H fragments remain on the active Ni upper surface. For methyl dissociation, H stays at the top of Ni while CH_2 absorbs at the site located in bridge position. Because of the stretched C-H bond, the adsorbed CH_2 then dissociates into CH and H atom. The H is at the top site and the resulting CH migrates to a 3-fold site.

Moreover, like CH_2, the resulting CH dissociates to form the co-adsorbed carbon. Here the C-H bond elongates in the TS and then breaks off, giving the activated metal a carbon atom deposited on a 3-fold site and an H atom, which still goes up. Moreover, the energy barriers of CH_4 decomposition are reported to be slightly weak. Hence, the carbon formed is the product of the CH_4 dissociation process.

For the first time, a theoretical study of the nitride-based catalyst was carried out by Das et al. [170]. They studied the methane dissociation over three Ni-based catalysts $(Ni_3N+AlN+Al_2O_3)$, $(Ni_3N+Al_2O_3)$ and (Ni_3N+AlN) The obtained results were surprising and difficult to explain, as they observed that the CH_4 dissociation occurred on the Al atom instead of the Ni atom over cat1 and $(Ni_3N+Al_2O_3)$, while, no dissociation occurred over (Ni_3N+AlN). Following this observation, they investigated the CH_4 dissociation over pure alumina, but no dissociation was recorded. To get further insights, they tested the role of AlN and observed that the dissociation energy was higher in $(Ni_3N+Al_2O_3)$ than in $(Ni_3N+AlN+Al_2O_3)$. Moreover, the orbital analysis showed that the lone pair of N atom is given to Ni atom, which leads to reduced Ni potential. This fact was further confirmed from HOMO energies that were in the order $(Ni_3N+AlN+Al_2O_3)< (Ni_3N+Al_2O_3) < (Ni_3N+AlN)$, which means that if the HOMO are unstable then the catalyst is more active towards dissociation. Hence, they concluded that the presence of AlN reduces the dissociation of CH_4.

Recently, Dou et al. [171] have studied the CH_4 dissociation on both Ni (111) surface and Ni_{15}/ZrO_2 catalyst surface. They found that CH_4 adsorb on the top site of Ni (111) surface then dissociates to CH_3 and H atom, which are located on the top and the hcp site respectively, in the TS_1 with a shortened C-Ni bond and a stretched C-H bond. Then they transfer to adsorb on fcc and hcp site in the final state. This process was neutral in thermodynamics. Furthermore, the adsorbed CH_3 dissociates through TS_2 to form CH_2

and H, where the resulting H atom moves to the adjacent top site, while the CH_2 species prefers to adsorb at the fcc site. In the final state, the CH_2 and H species were found to adsorb at the fcc and hcp site, respectively, with a slight endothermic reaction energy. For the next dissociation step, the CH_2 further dissociates into CH fragment, followed by its dissociation into C and H, in TSs, the final C-H bond lengths are 1.715 and 1.779 Å for the dissociated CH_2 and CH, respectively.

On Ni_{15}/ZrO_2, CH_4 adsorbs and dissociates to CH_3 and H on top of Ni_1 through TS_1. The CH_3 and H are bonded to the Ni_1 atom with a shrinkage of the C-Ni bond and stretching of the CH bond. However, the resulting CH_3 and H species transferred to the two adjacent 3-fold hollow sites, respectively, in the final state. In the TS_2, the methyl can dissociate into CH_2, and H species absorbed at the bridge site. Whereas, in the final state, the resulting CH_2 and H move to adsorb to the two adjacent 3-fold hollow sites. Regarding the dissociation of CH_2, it has been found that the resulted H binds to the Ni_1-Ni_{11} bridge site while the CH fragment locates at the 3-fold hollow site. In the final state, H atom moves to adsorb on the 3-fold hollow site, while CH locates on the 4-fold hollow site. In TS_4, the bond length of CH species first elongates than dissociates into C and H atom, where the left C atom remains located at the 4-fold hollow site, whereas the H atom moves to adsorb on the adjacent 3-fold hollow site. The potential energy profiles for CH_4 sequential dissociation over Ni(111) and Ni_{15}/ZrO_2, catalysis are presented in Figure 4.

25
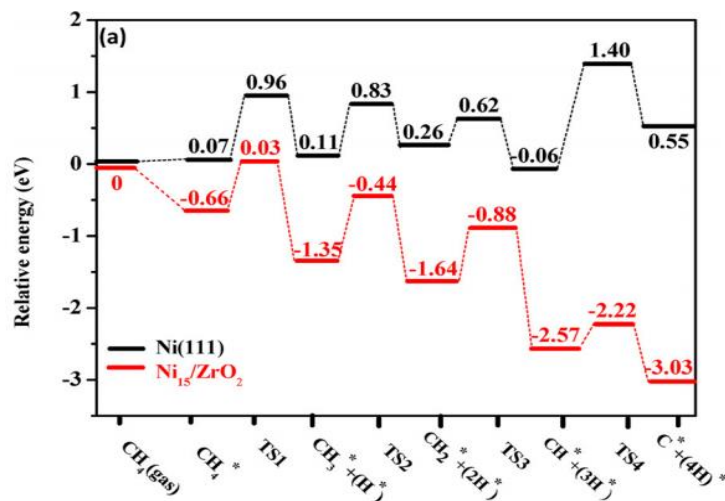
Figure 4. The potential energy profiles for CH_4 sequential dissociation over Ni(111) and Ni_{15}/ZrO_2. [171]

It has been noticed that all the CH_4 dissociation processes were exothermic. Moreover, it is reported that the energy barriers of CH_4 decomposition over most of the used catalysts in the DRM process are low. Consequently, the deposited carbon is the final product of CH_4 decomposition.

The adsorption energies E_{ads}, activation energies E_a, and the reaction energies of varied species involved in DRM reaction over various Ni-based catalysts and Ni surfaces, are summarized in Tables 3 and 4.

Table 3. Adsorption energies of DRM species on different Ni-based catalysts.

Catalyst	species	site	Bond distance (Å)	E_{ads} (eV)	ref
Ni (111)	CH_4	Top		-0.02	[153]
	CO_2	Top	C-Ni=3.85	-0.02	
	CO	Hcp		-1.92	
	H_2	Top		-0.22	
	C	Hcp		-6.78	
	H_2O	Top		-0.29	
Ni-Pt	CH_4	Ni Top	C-Ni=3.92	-0.005	[172]
	CO_2	Pt-Bri	C-O=1.28,1.21	-0.15	
	CO	Ni-FCC	C-Ni=1.96	-1.83	
	H_2	Ni-Top	H-Ni=2.94, H-H=0.75		
	C	Ni-FCC	C-Ni=1.78	-6.73	
	H_2O	Pt-Top	O-Pt=2.73	-0.03	
Ni_{15}/ZrO_2	CH_4	Top	C-Ni= 2.25	-0.06, -1.05	[171]
	CO_2	Bridge	C-Ni= 2.01	-1.29	
	CO	3-fold hollow	C-Ni= 1.92	-3.49	
	H	3-fold hollow		-3.46	
	C	4-fold hollow	C-Ni =1.84	-9.21	

	O	3-fold hollow		-7.25	
Ni$_4$/αMoC(111)	CH$_4$	Top	C-Ni=2.08	-0.39	[173]
	CO$_2$	C-Bri, O-top	C-Ni=1.86	-0.91	
	CO	C-hollow	C-Ni= 1.74	-1.92	
	H$_2$	Top		-0.48	
	C	C-hollow	C-Ni=1.73	-6.77	
	H$_2$O	O-Top		-0.75	
Ni-Pt	CH$_4$	Top	C-Ni= 3.7	-0.198	[159]
	CO$_2$				
	CO	Pt-Top	C-Ni= 1.94	-0.901	
	H$_2$	Pt-Top	H-Ni=2.93, H-H=0.76	-0.160	
	C	Hcp	C-Ni=1.76	-6.375	
	H$_2$O				
Ni$_2$Fe	CH$_4$	Ni-Bridge	H-Ni=2.84, 2.9	-0.1	
	CO$_2$	Fe-T	C-Fe=3.62	-0.02	[155]
	CO	Ni-Bridge	C-Ni=1.89	-1.8	
	H$_2$	Ni-T	H-Ni=2.87	0.06	
	C	NiFe-Hollow	C-Ni/Fe=1.79	-6.72	
	H$_2$O	Fe-T	O-Fe=2.18	-1.8	
Ni$_4$/MgO(100)	CH$_4$			-0.02, 0.05, -0.05	[174]
Ni$_8$/MgO(100)	CO$_2$			-0.03, -0.05, 0.08	
	CO			-2.42, -1.81, -1.81	
Ni$_{12}$/MgO(100)	H			-0.44, -0.4, -0.2	
	C			-8.14, -7.57, -8.15	
	O			-3.05, -2.83, -2.42	
Pt$_{12}$Ni	CH$_4$	Top, Holl, Top		-0.282, -0.201, -0.267	[175]
Sn$_{12}$Ni					
	CO$_2$	Holl, Holl, Bri		-0.596, -0.186, -0.524	
Cu$_{12}$Ni	CO	Top, Holl, Top		-2.534, -0.217, -1.656	
	H$_2$	Top, Bri, Bri		-1.192, -0.134, -0.403	
	C	Holl, Holl, Top		-7.102, -3.655, -5.879	
	H$_2$O	Holl, Holl, Top		-0.589, -0.263, -0.632	
Ni$_2$P(001)	CH$_4$	Ni 3-fol hollow	C-Ni=3.45, C-H=1.11, 1.12	-0.02	[176]
	CO$_2$	Ni Bridge	C-O1=1.31, C-O2=1.23, C-Ni=2	-0.05	
	CO	Ni 3-fol hollow	C-O=1.2	-1.97	
	H$_2$	Ni Top	H-Ni=1.59, 1.63, H-H=0.91	-0.71	
	C	Ni 3-fol hollow	C-Ni=1.81, 1.82	-6.53	
	H$_2$O	Ni Top	O-Ni=2.13, O-H= 1.01	-0.5	

Table 4. The dissociation barriers (Ea/eV) and the reaction energies (ΔE/eV) for the elementary steps involved in DRM reaction on different Ni-based catalysts and Ni surfaces.

Elementary step	$CH_4 \rightarrow CH_3 + H$		$CH_3 \rightarrow CH_2 + H$		$CH_2 \rightarrow CH + H$		$CH \rightarrow C + H$		$CO_2 \rightarrow CO + O$		ref
	E_a	ΔE	E_a	ΔE	E_a	ΔE	E_a	ΔE	E_a	ΔE	
Ni_{15}/ZrO_2	0.69	-0.69	0.91	-0.29	0.76	-0.93	0.35	-0.46	1.61	-0.52	[171]
$Pt_{12}Ni$	0.295	-0.252	0.577	-0.003	0.187	-0.160	0.238	-0.71			[175]
$Sn_{12}Ni$	2.981	1.687	3.809	2.348	0.802	0.016	2.809	2.306			
$Cu_{12}Ni$	1.142	0.009	1.548	0.322	0.031	-0.004	0.601	0.005			
$Ni_4/MgO(100)$	1.96	-0.77	0.17	-0.17	0.56	-0.55	0.47	-0.01	0.52	-0.32	[174]
$Ni_8/MgO(100)$	2.24	0.12	1.54	0.86	2.31	-0.29	0.91	0.76	0.3	-0.52	
$Ni_{12}/MgO(100)$	3.45	0.10	2.58	0.77	1.92	-0.13	1.39	0.55	1.15	-0.84	
$NiPt(111)$	1.057	0.118	0.297	0.175	0.575	-0.224	0.1445	0.815			[159]
$Ni_3C(001)$	0.58	-0.64	0.66	-0.27	0.39	-0.57	1.14	0.12			[177]
$Ni_3C(111)$	0.66	-0.53	0.76	-0.01	0.33	-0.66	0.86	0.07			
$Ni(100)$	1.233	0.674	0.622	0.093	0.218	-0.331	0.643	-0.031			[156]
$Ni(553)$	1.078	0.083	0.715	-0.083	0.145	-0.508	0.0466	-0.29			
$Ni(211)$	0.61	-0.29	0.64	0.24	0.17	-0.64	0.52	-0.28			[177]
$Ni(111)$	0.88	0.01	0.73	0.06	0.32	-0.33	1.35	0.54			
$Ni(111)$	0.89	0.04	0.72	0.15	0.36	-0.32	1.46	0.61	2.44	-0.96	[175]
$Ni(111)$	1.48	0.42	0.82	0.316	0.43	-0.137	1.456	0.81			[159]

II.5.2. CO₂ dissociation

The activation of CO_2 is a crucial step in the DRM process since it provides the primary oxidizer to the reaction [168]. The hydrogen adsorbed on the surface of the catalyst promotes CO_2 activation to form adsorbed OH and CO [165]. Experimentally and theoretically, the activation of C–O bond of CO_2 follows three different pathways: (i) direct dissociation to form CO and O ; (ii) CO_2 hydrogenation to form COOH or HCOO, which can be even more dissociated into CO and OH, or (iii) CHO and O atom [59, 161, 176, 178] as showed in the following reactions:

$$CO_2{}^* + * \rightarrow CO^* + O^* \tag{2.2}$$

$$CO_2{}^* + H^* \rightarrow COOH^* + * \rightarrow CO^* + OH^* \tag{3.2}$$

$$CO_2{}^* + H^* \rightarrow HCOO^* + * \rightarrow CHO^* + O^* \tag{4.2}$$
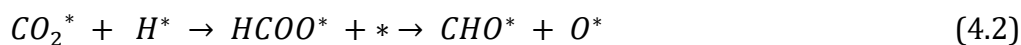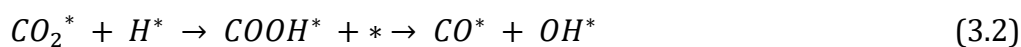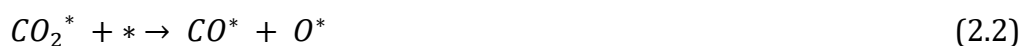
The H atom in the reaction pathway (3.2) results from CH_4 dissociation, which subsequently promotes the activation of CO_2 by attacking its C atom, leading to produce the intermediate COOH. The dissociation of COOH finally yields to the adsorbed CO and oxidant OH. The path (4.2) describes the formation of intermediate COOH, which dissociates into CHO and H. Subsequently, the adsorbed CHO dissociates to produce the adsorbed CO [157, 179].

The DFT calculations [59, 153, 171, 180] showed that the CO_2 molecule is only physically adsorbed on the Ni(111) surface and maintains its linear conformation in the adsorbed state. Furthermore, it was reported that the direct dissociation of the CO_2 over Ni (111) surface is the dominant reaction pathway. The primary oxidant involved in the DRM process was predicted to be the O resulted from this reaction, noting that the role of OH is not negligible because of the comparable energy barriers. On the other hand, the contribution of the HCOO pathway is lower, while the COOH pathway contribution could be insignificant.

However, many authors [161, 168, 171, 176, 181] have investigated the effect of supported and doped Ni on the adsorption energy and dissociation of CO_2.

In their work, Guharoy et al. [168] described the role of the Ni-Sn catalyst in CO_2 conversion; for the dissociation of CO_2, the initial state configuration is represented by the chemisorbed structure of CO_2 on the off-top position over the surface of NiSn1. In contrast, the final state shows that CO prefers to locate on the fcc site and O on the opposite bridge site. Compared with the activation of CO_2 over the Ni(111) surface, the reaction energy was almost double on the Ni(111) surface, facilitating a lower activation energy barrier. The same conclusion was drawn by Dou et al. [171] comparing the CO_2 dissociation on Ni(111) and Ni_{15}/ZrO_2 surfaces. Additionally, they found that the CO and

O resulting species prefer to adsorb at the adjacent bridge site and the bridge site, respectively, with a stretch in C-O bond length. In the final state, the CO and O species migrate to the adjacent 3-fold hollow site.

Niu et al. [157] investigated the adsorption and dissociation mechanism of CO_2 over Pt(111) surface and concluded that the pathway (ii) is the more straightforward reaction to be carried out compared to other routes because of the lower activation barrier compared with the two other reactions pathways; however, the pathway (iii) is unfavorable both kinetically and thermodynamically.

II.6.   Reversal of the Water-Gas Shift (RWGS)

The reverse water-gas-shift reaction (Eq. 5) is critical in producing hydrogen from steam and carbon monoxide [172]. Generally, the thermodynamics of the RWGS process seems to be more favorable at elevated temperatures to obtain a high degree of activity [173].

Numerous chemical routes for RWGS have been suggested in the literature, including formate, carboxyl, and redox processes, as well as those involving COH production (Figure 5) [174-176].
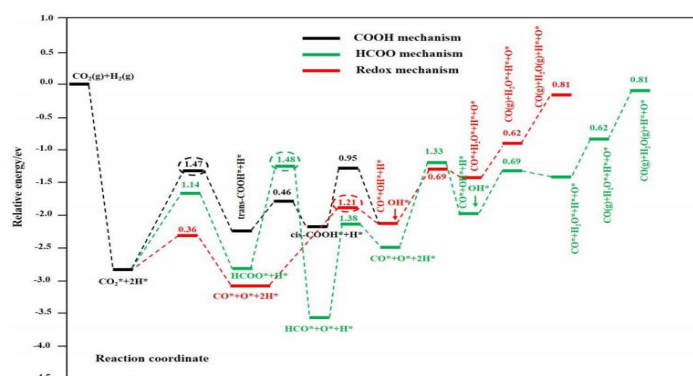
Figure 5. Overall reaction mechanism of RWGS. Adapted with permission from ref [177] © 2018 American Chemical Society.

According to recent theoretical studies, the formate and carboxyl processes are the most favorable reaction routes[178]. Additionally, in comparison to other pathways, formate

intermediates are the most abundant species identified owing to their high dissociation barrier energy. This indicates that the formate route is not prevalent[179]. It is worth noting that the rate-determining step in the Water Gas Shift (WGS) reaction is the dissociation of water on metallic surfaces[180].

The WGS may be improved across various metal-based catalysts, depending on the resistance of the catalyst to poisoning and its working temperature. Due to their availability, cheap cost, and strong catalytic activity, nickel-based catalysts are extensively employed in dry reforming methane. They are also active in WGS. Additionally, the WGS reaction has been studied on a wide variety of supported noble metals, including Rh, Pt, Pd, Ru, and Cu [181, 182], and it was discovered that the reaction is substantially enhanced when composite materials containing oxides are formed. These complexes serve as bifunctional catalysts, exhibiting both metal and oxide characteristics, increasing the kinetic reaction of WGS at the interface[183].

Zhang et al. [184] recently published a DFT calculation examining the redox reaction mechanism for RWGS on various nickel surfaces. Their findings indicate that the reactive species of the RWGS (CO, H_2O) preferentially absorb Ni(311) rather than on Ni (111). Because the energy barriers needed to activate CO_2 and produce water molecules are smaller on the Ni(311) surface, the RWGS reaction is preferred over the Ni(311) surface.

Yuan et al. [185] studied the CO_2 hydrogenation of the extended Ni(111) surface and the Ni(111) system with re-doping. The obtained findings indicated that the adsorption energy of CO_2 absorbed over the Re-doped Ni(111) surface was -0.48 eV more than that of the extended Ni(111) surface, suggesting the strong adsorption of the doped system. Similarly, the activation energy of CO_2 dissociation to CO* and O* was found to be lower on the Re-doped Ni(111) surface than on the pure Ni(111) surface, indicating that doping

the Ni(111) surface with Re encourages the O atom of CO_2 to adsorb on the Re and therefore increases C-O bond dissociation. Because of the given DFT findings, it seems as if the bimetallic alloy can alter the activity and selectivity of the RWGS reaction.

II.7. Effect of the support

II.7.1. Nature of the support

Recently, the DFT technique was used to examine the effect of the support on the performance of the Ni-based catalyst [95, 186]. Due to the MgO poor adsorption capabilities of the support, it has been claimed that it is not directly involved in the DRM process. However, the Mg vacancy acts as a strong anchor for the Ni cluster, inhibiting Ni particle aggregation and maintaining their separation. Additionally, the inclusion of MgO alters the chemical route for CO_2 methanation, switching it from the formate pathway through the HCOOH* intermediate over the Ni(111) surface to the formate pathway via the H_2COO* intermediate over the Ni/MgO surface. MgO is also advantageous for CH_2* hydrogenation and OH removal during the CO_2 methanation reaction due to its lower activation energy requirement than the extended Ni surface, which could be attributed to the strong adsorption of dissociated OH* on the Ni/MgO surface due to the high basicity of the MgO support.

On the other hand, the inclusion of MgO support enhances the Ni reducibility of the Ni/MgO surface, as shown by the Bader charge analysis. This may further increase the C-terminal hydrogenation of CO_2, which is the step that results in the optimum route is different from the one on the Ni(111) surface. Lustemberg et al. [128] investigated the DRM reaction on the Ni/CeO_2(111) surface using experimental and DFT techniques. They discovered that altering the stoichiometric circumstances or the reduced nature of the support may induce a significant electronic disturbance in the Ni nanoparticles, resulting

in a dramatic shift in the chemical characteristics of the catalyst toward the DRM process. In other words, when the reduction of the ceria support rises, the oxidation state of Ni nanoparticles changes from +2 to 0, demonstrating the considerable ability of the support to sustain oxidized Ni^{2+} by accommodating electrons in localized f-states[161]. This leads to an improvement in the stability of the chemisorbed CH_4 molecules owing to the lower activation barrier (0.04 eV) compared to the high activation barrier of the extended Ni(111) surface (0.8-1eV) [187, 188]. Additionally, it was discovered [189] that CO_2 dissociates with no energy barrier on the oxygen defect sites of CeO_2, in contrast to the high barrier demand on the flawless CeO_2 surface, indicating a critical function for the shape of the support.

Recent researches [19, 190] used DFT to investigate the reducibility and non-reducibility of Ni-based catalysts in DRM reactions. The obtained findings indicated that the estimated barrier energy for methane dissociation on the decreased Ni(100) surface was less than the 0.83 eV barrier energy calculated for the NiO(100) surface. However, the dissociation of CH_4 on the NiO(110) surface occurs with barrier energy of 0.59 eV and reaction energy of 0.25 eV, indicating that, although being less stable, the NiO(110) surface is more active in dissociating CH_4. In terms of coke deposition, the findings showed that it is simple to produce coke on the extended Ni(111) surface due to the C atom's low activation energy and high adsorption energy. In comparison, Ni oxide exhibited a more excellent coke resistance due to the lack of C adsorption.

II.7.2. Oxygen vacancy

Oxygen vacancies (OVs) are critical in various chemical reactions, including DRM. OVs can alter oxide surfaces' geometric and electrical structure, thus their chemical characteristics. Additionally, OVs may directly coordinate locations for enhanced inert

molecule adsorption, such as CO_2 and O_2. Because electrons are localized in OVs, they may serve as charge donor sites, activating these molecules[191, 192].

The results obtained by Wang et al. [193] indicate that the most active catalyst among those produced is the one with the greatest concentration of OVs, which serve as active sites for CO_2 activation. Additionally, the presence of OV has been shown to accelerate the production and dissociation of CO_2 intermediates [194]. CO_2 adsorption/activation occurs on decreased ceria or in the presence of H_2, signaling that the existence and composition of a vacancy are necessary (see Figure 6).
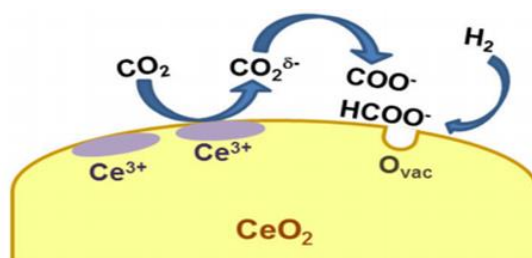
Figure 6. Proposed mechanism for CO_2 activation on ceria surface. Adapted with permission from ref [194] © 2019 Frontiers in Chemistry.

According to some authors [195-197], the metal-oxide catalysts' OV formation energy may contribute to the CH_4 oxidation process and the CH bond activation energy. Additionally, it is well recognized that increasing oxygen mobility is critical for increasing coke resistance and catalyst sintering[198].

The surface defect sites of the catalyst are essential because they participate in the adsorption process, which is a critical stage in the DRM reaction. Thus, the distribution of OVs on the catalyst surface is the sole acceptable criterion for limiting the search for the lowest energy architectures. As with the (101) surface of anatase TiO_2, where the subsurface OVs are more stable than the surface OVs [199,200], the topmost oxygen desorbs first as a necessary step in surface reactions.

Recently, DFT computations have received considerable attention for their significance and presence in the DRM process. Thus, different discoveries have arisen that add to our understanding of OVs' relative stability and electron localization on the support surface and subsurface.

The O surface vacancy formation energy (EO_{vac}), defined as the energy needed to remove one O atom from the catalyst surface, may also be utilized as a descriptor to forecast the performance of such catalysts.

Hinuma et al. [199] used the same calculation level to determine the EO_{vac} for various oxide surfaces. Compared to the energy of creation and the electron affinity, they discovered a significant connection between EOvac and Band Gap (BG). This finding is consistent with the fact that the oxygen vacancy is regarded as the breakage of metal-oxygen bonds. Thus, the HOMO-LUMO gap should affect the EO_{Vac}. Additionally, the scientists examined the adsorption of O_2, NO, CO, CO_2, and H_2 molecules on an oxygen-deficient surface. The EO_{vac} values determined in this research suggest that their adsorption energies and mechanisms of adsorption are highly dependent on EO_{vac}. The findings of this research may provide further light on the design of heterogeneous catalysts with appropriate oxygen vacancies for dry reforming and the prediction of their behavior and catalytic characteristics.

On the other hand, Huygh et al. [201] used comprehensive DFT simulations to investigate the impact of oxygen vacancies on the surface reactivity of TiO_2 anatase (001) towards CO_2 breakdown. Simultaneously, it was discovered that CO_2 dissociates slowly near the stoichiometric surface. It dissociates on a surface that contains oxygen vacancies. The findings of this study show that oxygen vacancies are critical for CO_2 breakdown on the

TiO_2 Anatase (001) surface. As a result, they are anticipated to play a significant part in the CO_2 conversion process throughout the DRM.

II.7.3. Metal loading and particle size

Particle size and metal loading are critical parameters in the catalytic reaction process. Consequently, many efforts have been undertaken to characterize the catalytic performance of samples according to their shape. According to extensive experimental investigations [202-204], reducing the size of Ni nanoparticles has a significant effect on catalytic activity and coke resistance. On the other hand, the value of the critical size remains a matter of dispute. According to many publications [205-209], the crucial size of Ni nanoparticles varies between 2 and 20 nm depending on the support type and reaction conditions; furthermore, when Ni is added to increase catalyst stability, choosing the optimal loading is essential. In this context, DFT provides critical information on the effects of particle size and Ni nanoparticle loading content on the DRM process, which may aid in our understanding of the process and guide future researches toward the development of stable, high-performance catalysts. Guo et al. [157] investigated the DRM reaction process in terms of various Ni nanocluster sizes (Ni_4, Ni_8, and Ni_{12}) supported on a MgO(100) surface. The findings indicate that when the size of the Ni nanocluster reduces, CH dissociation, C oxidation, and the energy barriers associated with CH_4 dissociated adsorption decrease. According to the Hirshfeld charges analysis of the three systems, only Ni atoms in the two layers closest to MgO may accept electrons from the support, and the primary electron transfer occurs between the Ni atoms and the directly contacted species. Consequently, catalyst systems containing nanoclusters of nickel exhibit high catalytic activity, as Ni atoms in contact with the support surface gain additional electrons. Similarly, DFT findings on the effect of clustering on carbon

deposition on Ni(001) nanofacets [209] showed that the binding energy of the C atom on Ni nanocubes less than 5nm in size was reduced as anticipated.

On the other hand, the electronic action of the CeO_2(111) on the highly scattered Ni atoms results in the production of Ni in its most oxidized state, namely +2. This is consistent with the experimental findings showing that at low temperatures and 0.2ML coverages, a significant Ni dispersion occurs on the CeO_2 (111) surface, with the majority of Ni in the (+2) oxidation state [128]. Lustemberg et al. [101] noted that for low-loading M/CeO_2 (M=Pt, Ni, Co) systems, the barrier energies for methane dissociation were lower than those in metal clusters and extended metal surfaces due to the strong metal-support interaction, which resulted in the stabilization of both CH_4 and CH_3 + H products.

Additionally, Pan et al. [210] demonstrated that CO_2 is likely adsorbed and activated at the metal-support interface sites in their DFT study of CO_2 adsorption over -Al_2O_3 supported 3d transition metal dimers (Sc-Cu). This suggestion may be accomplished experimentally by increasing the metal dispersion over the support surface. On the other hand, big nanoparticles diminish the interface while maintaining the same metal loading, resulting in decreased catalytic activity.

II.7.4. Metal-support interactions

Active metals and supports are critical components of heterogeneous catalysts and are primarily utilized in the chemical industry and research. Metal-support interaction affects the stability and dispersion of active metals and may alter their morphology and electronic structural characteristics, resulting in increased catalytic activity [192, 211].

Metal-support interactions are extensively researched in the catalysis field since they reflect the impact of the active phase and close catalytic support. Further study is required to understand better the nature of metal-support interactions and their effect

on the characteristics and reaction activity of the catalyst. Strong metal-support interactions (SMSI) have recently been identified as a possible explanation for the variations in the decreased activity of supported catalysts, and (Temperature programmed reduction) TPR profiles are usually employed to determine the existence of SMSI [212, 213].

Additionally, the presence of SMSI may enhance the catalytic activity by preserving the particle size and generating a high active metal dispersion (Figure 7), which is primarily responsible for the resistance to sintering and coke production [22].

In their research, Liu et al. [214] showed that the SMSI between Ru and Fe is critical for stabilizing the Ru atoms and promoting the ripening of RuO_2 aggregates.
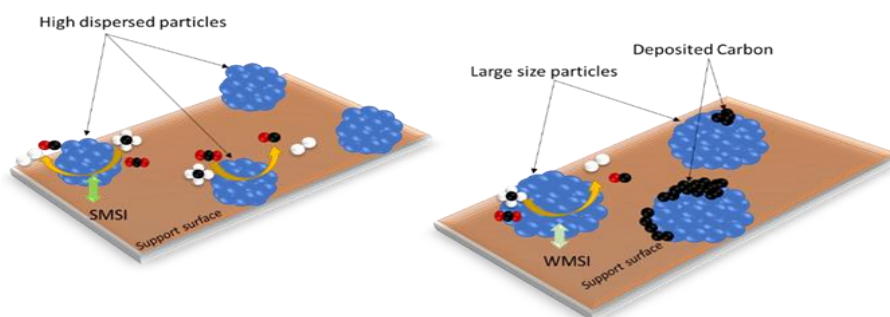
Figure 7. The effect of SMSI on the dispersion of particles over the support surface.

Recently, DFT studies [39, 149, 212, 215, 216] have been widely utilized to understand metal-support interactions further, thus opening up new and improved routes for controlling current reactions and elucidating essential elements of the catalytic process.

The activation energy needed to break the C-H bonds of methane adsorbed on the catalyst surface involved in SMSI may be predicted using DFT simulations. According to[217], the primary source of chemical change between adsorbed species and active sites is the electronic distribution in the active metal. It results from the reducibility and varied stoichiometry of the support.

According to Rounder et al. [218], the electrons transported from the active metal to the support appear as bound state electron-hole pairs stabilized and locked at the interface due to Coulomb interactions. As a result, it is challenging to include the active sites in reactions. Additionally, they proposed that the polarization effect might be caused by the extra electron charges on the metal surface being replaced by charge carriers that can freely travel on the support surface. Thus, the electrical polarization generated by metal-support contact is analogous to the bias potential n in electrochemical experiments. As a result, they determined that the metal-support interaction is caused by a potential difference caused by the slight electrical charge on the supported metal. Furthermore, it was discovered that alumina displays a weak metal-support interaction (WMSI), which is thought to be linked to the low electrical polarization of the oxide supports.

DFT simulations of Van Heerden[212] showed that CO dissociation over unsupported cobalt is not appropriate for particular applications owing CO dissociation over unsupported cobalt is inappropriate for a specific reason applications due to the high barrier energy. However, the CO molecules were dissociated favorably in the presence of surface hydrogen, defect sites, or edges, indicating that the presence of the ligand has a comparable impact to the influence of the promoter on CO dissociation as opposed to the metal-support interaction.

Moreover, Zhang et al. [219] investigated the stable adsorption sites for Ni atoms on the α-Al$_2$O$_3$(0001) surface. They found three types of stable adsorption sites on the surface for a single Ni atom, the most appropriate is the oxygen threefold empty site. Additionally, as the number of Ni atoms increases, no location on the support is favored for Ni adsorption. Once the Ni cluster has been adsorbed onto the support, the electron charge is transferred inside the metal. Local polarization created by the support surface

stabilizes and fixes the metal cluster to the support surface. Ni atoms' diffusion activation energy was reduced across sites on the support surface, enabling Ni atom movement.

The findings of this research may contribute to a better understanding of the metal-support interaction and offer helpful guidance for designing and creating new and effective DRM catalyst systems.

On the other hand, it is worth mentioning that the traditional SMSI may lead to the active metal sites blockage and degradation of catalytic performance due to the migration of oxide species from the reduced support to the metal sites[39] (see Figure 8). Recent studies[220-222]on Co, Pt, and Ni supported over TiO_2 catalysts revealed that the TiO_x layers covered the metal nanoparticles migrated from the support, resulting in suppression of chemisorption capacities of the reactants.
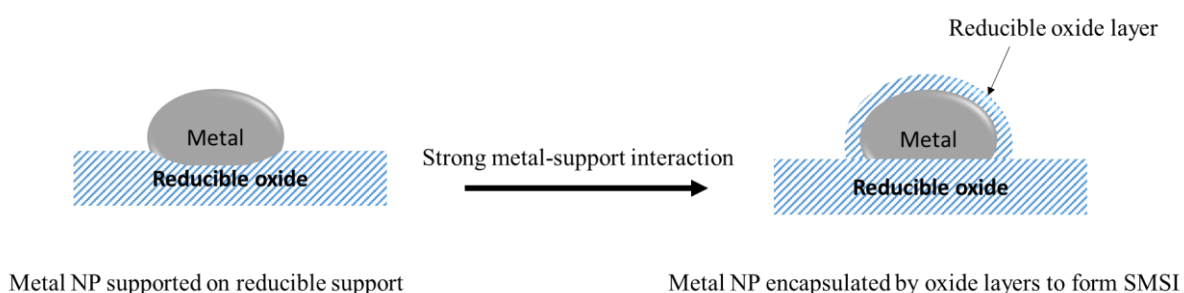
Figure 8. The conventional SMSI formation process. Reproduced with permission from ref [223] © 2020 Springer Nature.

In contrast, it has been found [21, 224] that the reducible CeO_2 support could modify the electronic properties of low-loaded nickel particles in direct contact by changing their oxidation state during oxidation. More specifically, due to the strong metal-support interactions between Ni and ceria, two $4s$ electrons of Ni atoms, which are in direct contact with the support surface, are transferred to the vacant $4f$ band of the ceria, leading to reduce two Ce^{4+} ions to Ce^{3+}. Simultaneously, the Ni atom oxidizes to Ni^{2+},

whereas those on the top remain in their metallic state (Ni^0), showing the rapid decrease in the metal-ceria interaction. Moreover, it has been demonstrated[225] that the two excess electrons produced by forming a neutral oxygen vacancy e localized at cation sites in the outer plane of cations, leading to reducing the Ce^{4+}. The most energetically stable near-surface oxygen vacancy structures have vacancies at subsurface oxygen locations for a wide range of vacancy concentrations. The adsorption energy of the Ni atom decreases with an increasing degree of near-surface reduction, and Ni adatoms regain their metallic character ($Ni^{2+} \rightarrow Ni^{1+} \rightarrow Ni^0$). Basically, as the concentration of Ce^{3+} ions increases, it becomes increasingly difficult for Ni to transfer charges to the already reduced support, which is consistent with the experimental findings and demonstrates that Ni binding is greater at low coverage on a ceria surface with less reduction[21]. This suggests that the ability of ceria to stabilize oxidized nickel species (Ni^{2+}) on the CeO_2 surface by re-localizing electrons on localized f-states (Ce^{3+}), is a key factor in determining the Ni heat of adsorption. These findings are very different compared to those obtained from previous studies on three-dimensional nanoparticles and extended nickel surfaces[188].

Consequently, the strong Ni-ceria interaction present at low Ni loadings results in active and stable $Ni-CeO_2$ catalysts for methane activation, allowing the use of the adsorbed CH_x compounds for chemical processes. Additionally, such Ni-ceria systems were also found to be active towards DRM process at a low temperature of 700 K. The C atoms produced by total CH_4 dissociation interact with lattice oxygen atoms at this temperature to produce CO molecules, which desorb in the gaseous phase, creating an oxygen vacancy[224].

Li et al. [149] demonstrated that by lowering the MSI, absorbed CH_4 and H_2 may alter the structure of the Ni4 cluster supported on the (100) -alumina surface. This finding may offer further information on the Ni/γ-Al_2O_3 interaction and the mechanism by which the SMSI leads to the development of carbon nanotubes.

II.8. Deactivation

II.8.1. Coke deposition

Carbon deposition on the catalyst surface is mainly caused by direct CH_4 cracking on the active metallic phase, which results in active site blockage and, therefore, catalytic deactivation[226]. When the catalyst is new, the carbon deposition process is usually quicker, as the CH_4 goes through a series of breakdown stages to generate deposited carbon and H_2. Carbon is then oxidized through O adatoms liberated during CO_2 dissociation ($C + O_2 \rightarrow CO_2$), as shown in Figure 9. Consequently, coke production at elevated temperatures is caused by unoxidized carbon adhering to the metal surface [227].
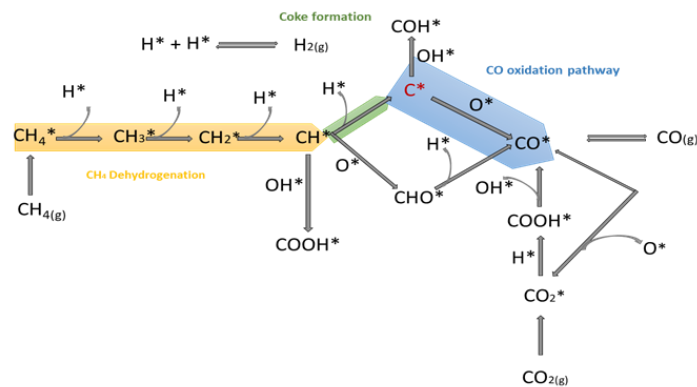
Figure 9. A schematic diagram for the dominant reactions in the DRM process, including coke formation. Reproduced with permission from ref [106] © 2020 MDPI.

The second possibility is CO disproportionation through the Boudouard reaction (Eq. 3), which is thermodynamically favorable at high pressures and temperatures and may

result in the formation of additional carbon. In their experiments, Nagaoka et al.[228] discovered that coke deposited on different supported Ru catalysts at 2 MPa was more significant than coke deposited at 0.1 MPa on the same catalysts. McKenzie et al. [229] also found that the temperature of the reaction and the molar ratios of the different species involved had a significant effect on carbon deposition.

The ratio of carbon produced by CH_4 dissociation and CO disproportionation to surface carbon oxidized by CO_2 affects the pace and quantity of carbon deposited on the catalyst surface.

The dissolving and surface coupling mechanisms have been proposed as alternative mechanisms for carbon deposition. Carbide precipitates on the backside of active metal nanoparticles due to surface carbon dissolving in the bulk of the metal, producing a carbon nanofilament. On the other hand, the deposited surface carbon will rearrange to form a stable surface cluster during the surface coupling process[230, 231].

The following table summarizes the potential carbon deposition reactions:

$$CO(g) + H_2(g) \leftrightarrow H_2O(g) + C(s) \qquad \Delta H°_{298K}= \text{-131.3 kJ mol}^{-1} \qquad (10)$$

$$CO_2(g) + 2H_2(g) \leftrightarrow 2H_2O(s) + C(s) \qquad \Delta H°_{298K}= \text{-90.1 kJ mol}^{-1} \qquad (11)$$

According to DFT simulations [163], the amount of carbon deposited is highly dependent on the main oxidation route of the C-H bond in the overall oxidation process and the high energy barrier associated with CO dissociation. As a consequence, it has been determined that the Ni(111) surface is the most resistant to carbon deposition in comparison to the Ni(211) and Ni_3C(111) surfaces, which exhibit only negligible resistance.

Coke formed on the surface of the catalyst can take on a variety of shapes (carbide, amorphous, polymeric, nanotubes, graphene type, shell-type graphitic), depending on the

nature of the active metal and support/promoter, the support surface area, the location of the active metal concentration, the temperature, and the duration of the reaction[232-235].

According to Aramouni et al. [18], coke may be formed in three primary forms: gum, pyrolytic coke, or whiskers. At lower temperatures, the gum is produced as a CH_x monolayer or multilayer graphene that envelopes the catalyst, while pyrolytic coke and whiskers are more often created at higher temperatures. Pyrolytic coke is usually produced at elevated temperatures using heavy hydrocarbons. Whisker carbon, sometimes called filamentous carbon, is the most abundant carbon type deposited on nickel-based catalysts. This carbon is formed at elevated temperatures and is preferred in the absence of water and aromatic compounds.

Additionally, the various carbon sources produced during the reaction (from the Boudouard reaction, CH_4, and other decomposition) agglomerate on the exposed side of the catalyst. They formed a filamentous carbon that grows around the active metal eventually covers the Ni crystal, pushing it out of the catalyst. However, since filamentous carbon does not immediately deactivate the catalyst, less deactivation will be seen throughout the reaction.

On the other hand, the Ni particle will ultimately disintegrate when the carbon filaments clash with its pore walls, owing to the carbon filaments' great mechanical strength[236]. Thus, the production and deposition of coke may result in catalyst deactivation throughout the DRM process, leading to reduced durability and activity [237]. As a result, it is critical to maintain control.

To get a better understanding of the coke-resistance of Ni single-atom catalysts (SACs), Akri et al. [227] used DFT calculations to examine the first two pathways of CH_4

breakdown on the $Ni_1/CeO_2(111)$ surface, as well as the decomposition series of CH_3 fragment. They discovered that dehydrogenating methyl, $CH_3 \rightarrow CH_2 + H$, was thermodynamically unfavorable due to its significant activation barrier. As a result, the presence of CO in the catalytic system looked contradictory. They evaluated CH_3 oxidation to CH_3O as a possible alternate pathway for converting reactively generated CH_3 to CO after the first CH_4 activation without carbon deposition. The oxidation of CH_3 to CH_3O over a Ni_1/CeO_2 catalyst is exothermic and has a low energy barrier. Simultaneously, it was discovered that the following dehydrogenation of CH_3O to CHO is highly exothermic, while the rate-determining step leading to the final CO product (HCO CO+ H) is endothermic. Consequently, they determined that oxidizing CH_3 to CH_3O is a plausible indirect route for dehydrogenating CH_3 to CO.

Additionally, Senanayake et al. [238] demonstrated that electrical disturbance of the metal-support system in the $Ni-CeO_2$ catalyst might reduce the ability of Ni to dissociate C-O, resulting in less carbon deposition on the catalytic surface. Furthermore, Yang et al. [239] hypothesized that electrons released from oxygen vacancies in ceria might move to the empty d-orbital of Ni0 through the $Ni-CeO_2$ interface, thus inhibiting the breakdown of CH_4.

Omran et al. [106] have studied the carbon deposition mechanism on a bimetallic Ni_2Cu catalyst using DFT-assisted microkinetic analysis. Their findings indicated that most carbon deposits occur through the CH_4 dissociation route. In comparison, the carbon produced by CO_2 was insignificant owing to the low-rate constant (k) of CO*. Moreover, the quantity of carbon deposited is highly dependent on the $k_{CH/C}$ oxidation pathway ratio. Wang et al.[163] found that raising this ratio decreases carbon deposition in this respect. Their study of the temperature impact on carbon formation (from 800 to 1000

K) revealed that the rate constants for C*+O* and CH*+O* (or + OH*) formation are proportional to rising temperature. The rate constant of carbon oxidation by O or OH was greater than that of CH breakdown. As a result, increasing temperature increases $k_{CH}/k_{C(O)}$ and decreases $k_{CH}/k_{C(OH)}$, indicating that carbon deposition by atomic O is easily removed at elevated temperatures. This highlights the critical role of the OH in limiting carbon deposition via the CH dissociation pathway, whereas $k_{CH}/k_{C(O)}$ << $k_{CH}/k_{C(OH)}$. Additionally, the energy barrier for the reaction, $C^* + O^* \rightarrow CO(g)$, which was the most favorable, was 0.72 eV. This result was much less than those achieved when $NiF_2(111)$ and Ni(111) catalysts were used [138, 240-242]. As a result, DFT showed the high resistance performance of Ni_2Cu catalyst toward coke deposition compared to previously reported catalysts.

II.8.2. Sintering

Although transition metals are a less costly and plentiful source of catalytic precursors than noble metals in DRM, understanding the rapid deactivation caused by coke deposition and catalyst sintering under DRM conditions is a significant issue [217]. Due to the robust stability of CH_4 and CO_2, the DRM requires considerable activation energy to initiate the downstream chemistry, rendering the reaction endothermic and necessitating a high temperature. Additionally, secondary exothermic reactions such as the Boudouard reaction, the WGS, and the conversion of CH_3O to CHO occur during the reaction, resulting in an increased local temperature that adversely affects the stability of metal particles the catalytic activity by causing catalyst sintering. As a result, sintering is the primary mechanism through which catalysts deactivate at elevated temperatures [68, 243].

Sintering is a thermal process that results in the migration of metallic nanocrystals (NCs) across support due to the weak metal-support contact and the strong chemical driving force. NCs aggregate to create a nanocluster with a smaller surface area and a variety of structural variations. To comprehend the growth of NCs, two mechanism routes have usually been proposed: Ostwald ripening (OR) and crystallite migration and coalescence (CMC) processes (see Figure 10). OR explains the migration of single metal atoms in three steps: I production and migration of metal adatoms and metal-ligand complexes from metallic crystals, (ii) dispersion of the generated species across the support surface or in the gas phase (iii) species attraction through increasing NCs. Alternatively, the CMC process may be characterized as the aggregation and cohesiveness of many single-crystalline clusters due to Brownian motion and proximity[244, 245]. Sintering has also been reported to occur due to a decrease in the surface energy of crystallites due to their size-dependent mobility on the catalyst carrier, leading to the collapse of support holes on active phase metals[246].
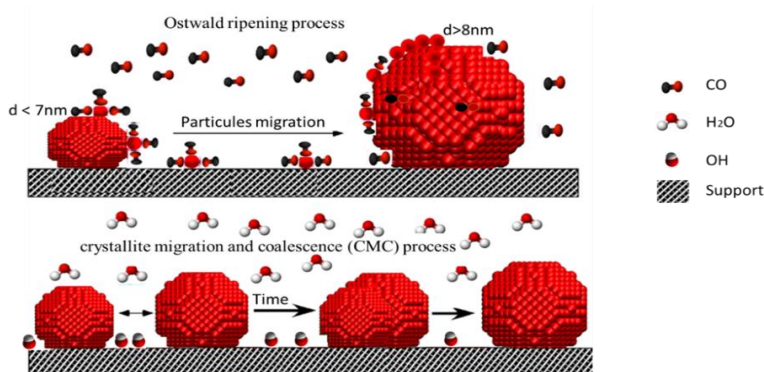
Figure 10. Ostwald ripening (OR), upper scheme, and crystallite migration and coalescence (CMC), lower scheme. Reproduced with permission from ref [244] © 2020 American Chemical Society.

Additionally, it was discovered that a high H_2O concentration [247], a large particle size and a high particle loading [248], a weak metal-support interaction [244], and a low metal

dispersion on the surface of the support [243, 249] could all contribute to the development of more pronounced sintering phenomena. Consequently, many efforts and methods have been developed to provide superior anti-sintering performance while minimizing catalyst regeneration and recovery costs. To this end, it has been reported [48, 243, 250, 251] that the increased sintering resistance at elevated temperatures is due to the confinement effect, which is facilitated by the mesoporous supports core-shell structure of the support and by strong metal-support contacts. As a result, it is critical to improve metal-support interactions further to avoid sintering. Numerous studies have also used Molecular Dynamics Simulation to study the mechanism of sintering events in recent years [252-255]. However, DFT simulations have been widely utilized to open new avenues for studying the behavior of the metallic phase over a variety of support surfaces and to shed further light on catalyst deactivation through sintering.

Xu et al. [256] used DFT to shed light on the mechanism behind the increased rate of sintering of Ni nanoparticles in a water vapor environment. Their findings indicated that the attractive contact between Ni nanoclusters was responsible for the sintering of Ni nanoparticles in a vacuum. For the adsorption and dissociation of H_2O, it was discovered that increasing the number of H_2O molecules on the Ni surface favors their adsorption owing to the H-bond interaction and the resulting reduction in activation energy. Additionally, adsorption simulations on Ni clusters with O, H, and OH-terminated molecules showed that the most significant interaction between Ni clusters and other terminated H and OH occurred in a vacuum compared to Ni clusters and additional terminated H and OH. Two Ni clusters approach one another more rapidly in the presence of vapor than in a vacuum due to the strong attraction produced by the O terminations.

On the other hand, Zou et al. [156] reported the Bader charges and partial density of state (PDOS) of Ni_4/α-MoC(111) and Ni_4 /MgO(100) catalysts using a DFT method. The findings show that the α-MoC(111) and defective MgO(100) surfaces have the opposite electron impact on the Ni_4 cluster (electrons move from the Ni_4 cluster to the support surface in the Ni_4/α-MoC(111) catalyst and from the support surface to the Ni_4 cluster in the Ni_4/MgO(100) catalyst). This results in a stable contact between the metal and the support (SMSI). Consequently, Ni_4/α-MoC(111) catalyst exhibited a high binding to reaction intermediates (*CH_3,*CH_2, and *CH) and a lesser binding to *C, *H, and *O terms of Bader charges. According to prior studies, the strong metal-support contact indicated in this study may inhibit sintering and carbon production.

II.9. Current challenges

Identifying a novel catalyst appropriate for a particular reaction is just the beginning of a series of procedures required for the technical implementation of this catalyst under specified operating circumstances. Thus, the ability of the designed catalyst to remain active under realistic reaction conditions, its stability over time, implying resistance to deactivation via carbon deposition and sintering, and its capacity to achieve high reactant conversion and selectivity, remain critical challenges for in-silico investigation in the DRM process. As a result, the intrinsic development of precise simulation tools for catalysts' characteristics and methodological enhancement is needed [257]. Additionally, the process of creating novel catalysts at the atomic level spans many time and length scales owing to the significant discrepancy between computational and experimental data [258]. Due to the precise capture of metals' delocalized electron structure, periodic slab models provide a practical approximation for simulating heterogeneous catalysts for big metal nanoparticles (> 5nm). However, creating such models may be problematic due to many terminated surfaces. Graph theory [259] and covariant transformations[260]

have been suggested to address this issue. It is difficult to estimate the surfaces of alloy catalysts. As a result, perfect surfaces are often used in HTS (high-throughput screening) simulations to investigate reactivity trends[258]. Another challenge in predicting catalyst activity is the substantial change in the reaction rate constant caused by a slight change in the energy barrier, which often results in an accuracy mistake. As a result, only approximation techniques can determine the transition state energies for large catalytic systems. Additionally, functionals based on the Generalized Gradient Approximation (GGA) are often employed in the area, with up to 20 kJ/mol errors for reaction barriers and adsorption energies [261]. Although it has been successfully used to characterize trends in DRM catalysts, correctly modelling the metal-support interface at a nanometric scale remains a problem since it is computationally costly even at the GGA level [261, 262]. Moreover, when describing the electronic properties of the open-shell orbitals, such as *3d* and *4f* orbitals in transition metals and rare-earth oxides, for example, in the Ni-ceria system, the delocalization problem usually occurs due to the SMSI of low-loaded Ni-ceria. It results from the ability of ceria to stabilize oxidized Ni species on its surface by re-localizing electrons on localized f-states[263]. In this scenario, previous investigations[264, 265] on ceria surfaces have reported that pure GGA-DFT approximation provides a self-interaction error (SIE) and fails to describe the localized Ce (III) states observed by UPS[266]. Furthermore, several failures exist in all GGAs, for instance, the underestimation of band gaps, underestimation of energy barriers for molecular reactions, and overestimation of metallic character and electron delocalization. The fundamental reason for these constraints is the approximation to the unknown XC functional that does not cancel Coulomb self-interaction, which stabilizes solutions by delocalizing the electron density. Thus, hybrid approaches (periodic and clusters) [264,267, 268]have been used instead and found to provide significant

improvement in the description of the electronic structure. However, the high computing cost of periodic calculations limits its application. A more pragmatic approach and computationally more efficient to describe metal oxide systems containing localized d or f electrons is the so-called DFT+U[269]approach. The effectiveness of the DFT+U approach has been demonstrated in recent applications, improving the description of a wide range of local electron defect systems, including cation reduction such as CeO_2, TiO_2, MgO, and SiO_2[270]. Recently, James et al. [271]investigated the GGA-DFT+U effect on the adsorption of SO_2, CO, NO, and H_2 on cerium oxide compared to the pure GGA-DFT. The obtained results (see Figure 11) demonstrated that the Hubbard U parameter is necessary to improve the description of the simulated catalytic behavior of cerium oxide on both adsorption energy values and thermodynamic reaction profiles.
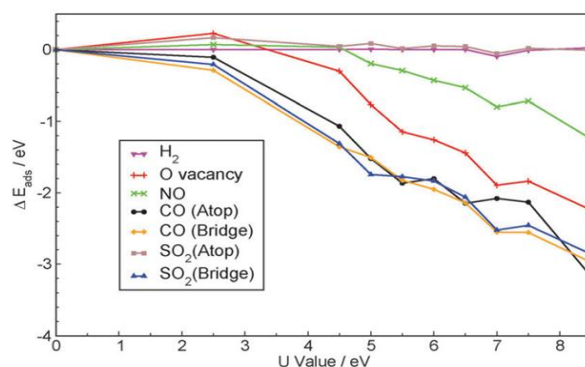
Figure 11. The adsorption energy variation with respect to U for the studied species. Adapted with permission from ref [271] © 2014 Royal Society of Chemistry.

Shishkin et al.[272] investigated the impact of the Hubbard U parameter on the Ni interaction with ceria support. Thus, a 5.3eV value has been taken for the Ni atoms. They found energies of 140 and 111 kcal/mol for interface and surface vacancy formations, respectively. Both the energies were lower than 20 kcal/mol in the case of U=0. In the same context, using CO on NiO surfaces as a testing ground, Rohrabtch et al. [273] have demonstrated that a DFT+U approach could provide a reasonable strategy for calculating the bulk properties of strongly correlated transition metal compounds and lead to

significant breakthroughs in the description of molecular adsorption on the surfaces of these critical materials as well. Thus, the computed adsorption energy of CO on NiO(100) surface (for CO coverage of 0.25 ML) using GGA-DFT+U was 0.33 eV, remarkably close to the experimental value of 0.3 eV, whereas the obtained value using pure GGA-DFT was equal to 0.73 eV.

However, a current drawback of the DFT+U approach is the determination of the U value which is still under debate[274]. This makes theoretical investigations using the DFT+U approach sometimes challenging for heterogeneous catalysts involving transition metals and rare-earth oxides, especially ceria-based catalysts. Extensive research have been reported to provide the optimal modulus of the U parameter for the most used materials. Lutfalla et al.[275] have performed a GGA-DFT+U calculation method to determine the optimal value of U parameter for some transition metals and rare-earth oxides aiming to link the calculated reduction and oxidation energies with the experimental data. Hence, they have recommended the following values for the calculations of the energy of oxygen-atom transfer U_{eff} = 2.3, 2.0, 8.6, and 0.2 eV for Ti, V, Mo, and Ce, respectively. However, it is questionable whether the exact value of U_{eff} should be used to calculate different physical parameters. Furthermore, several investigations [276-278] using GGA-DFT+U formalism with Hubbard parameter U= 4.5 and 5 eV for ceria catalysts support found to provide good results for the description of the electronic properties and the estimation of reaction pathways. However, one drawback of this approach is that the experimental formation energies of O_{vac} are challenging to determine. Therefore, different U values have been reported for the same element.

As a result, the requirement for more efficient techniques and codes to handle the complexity of systems, which includes the support nature of the actual catalyst and its

dynamic behavior, continues to be a significant problem. Additionally, it may be helpful to develop systematic methods for determining materials' ground state and electronic structure without resorting to lengthy and intensive experimental campaigns [261]. Finally, it is essential to emphasize that although only experimental studies can validate the effectiveness of a proposed catalyst, a well-built simulation tool may significantly aid in the selection and pre-screening of viable candidates.

On the other hand, Zou et al. [173] have reported the Bader charges (Table 5), and the partial density of state (PDOS) (Figure 12) obtained by comparing Ni_4/α-MoC(111) and Ni_4/MgO(100) catalysts using DFT approach. The results have indicated that α-MoC(111) and defective MgO(100) surface have converse electron effect for Ni_4 cluster (electrons transfer from Ni_4 cluster to the support surface in Ni_4/α-MoC(111) catalyst, and from the support surface to the Ni_4 cluster in Ni_4 /MgO(100) catalyst). This determines a strong metal-support interaction (SMSI). As a result, Ni_4/α-MoC(111) provided a strong binding to the reaction intermediates(*CH_3,*CH_2 and *CH) and a weaker binding to *C, *H and *O compared to Ni_4/MgO(100) catalyst. The strong metal-support interaction denoted in this investigation could suppress sintering and carbon formation, according to the previously discussed research.

Table 5. The Bader charge of Ni 4 cluster on α -MoC(111) and defective MgO(100)surface[173].

samples	Bader charge of Ni^l				Total Bader charge of Ni_4
	a	b	c	D	
defective Ni_4 /MgO(100)	0.52	0.12	0.17	-0.10	0.71
Ni_4 / α -MoC(111)	-0.12	-0.16	-0.13	-0.01	-0.42
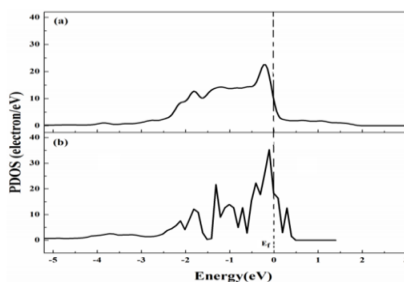
Figure 12. The PDOS of Ni_4 cluster on α-MoC(111) (a) and MgO(100) [173]

Chapter III

Alumina support and Ni nanoclusters

III.1. γ-Al₂O₃ structure

Alumina (or Aluminum oxide, Al_2O_3) is one of the most used materials in the chemical industry. Due to its many physio-chemical properties, such as mechanical resistance, high thermal stability, high surface area, electrical insulation and high ionic interatomic bonds[278]. Alumina has gained a significant attention from many scientists. Besides its application as a sorbent[279], fine chemicals field, refining[280] and petrochemical, alumina showed an important results in the catalysis field for a large number of reactions. Although, the application of the pure alumina is largely used in academic research, it is still limited in the industrial field[281]. On the other hand, alumina is mostly used as a support in the industrial catalytic process. Thus, several noble metals, transition metals and different oxides are supported on alumina [282-284]. In dry reforming of methane (DRM), based-supported metals on alumina are largely used. Moreover, compared to the other supports, alumina exhibits a high catalytic activity due to surface proprieties.

Five crystalline structures of aluminum hydroxide exist gibbsite, boehmite, disport, bayerite and nordstrandite. They are called precursor hydroxide, their particles size is varying from one type to another depending on the preparation method, and their dihydroxylation process occurs between 300 and 600°C. By increasing the temperature near than 1100°C, α-Al_2O_3 will be formed, above this temperature alumina particles start to sinter and change their crystalline structure to hexagonal microplatelets which are known as 'Tubular crystals'[285].

Thus, between the temperature of aluminum hydroxide dihydroxylation and the formation of α-Al_2O_3 crystals, several alumina structures known as transition alumina or activated alumina are formed (η-, κ-, χ-, θ-, δ- and γ-Al_2O_3). Consequently, the structure

of each alumina type depends strongly on the temperature condition and the precursor hydroxide used[286].

Among those different resulted alumina, γ-Al$_2$O$_3$ and α-Al$_2$O$_3$ are the most used in the catalyst field[287].

γ-Al$_2$O$_3$ is formed as a result of the dehydration process of Boehmite (AlOOH) through a topotactic transformation (eq.1) and it is widely believed that it takes the spinel-based structure, while the bulk structure is still unknown [288].

$$AlOOH \rightarrow \gamma \rightarrow \delta \rightarrow \theta \rightarrow \alpha - Al_2O_3 \quad (1.3)$$
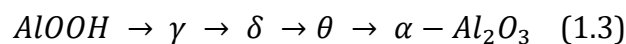
Despite their wide applications, the structure of transition alumina is still under debate and their exact morphology remains mysterious.

However, various research efforts are underway to provide more insights on γ-Al$_2$O$_3$ structure. Thus, many scientists suggest that the required model must be to take into account the cations occupancies of non-spinel positions and the tetragonal defect of the cubic structure[288, 289].

The first step to study the alumina structure is to investigate the transition of the boehmite γ-AlOOH to γ-Al$_2$O$_3$ and determine the realistic alumina bulk model[287]. The second is to determine the properties of different exposed surfaces of γ-Al$_2$O$_3$[290, 291] (111), (110) and (100) in realistic conditions of water coverage, calcination temperature which allows to figure out the hydration state of those surfaces and provide a clear image (more details) about the surface structure such as Al sites, OH groups (number of acid sites) to more understand the surface interaction with different reactants.

The empirical model of γ-Al$_2$O$_3$ structure proposed by Knozinger and Ratnasamy[281], was the most popular model for 25 years. Although, this model was the best possible

approach and has allowed to interpret different experimental tasks, it has been later questioned by several theoretical and experimental investigations[290, 292, 293]. Recently, Digne et al[291] have reinvestigated the structure and the adsorption properties of γ-Al₂O₃ surfaces using the DFT calculations taking into consideration the required hypothesis cited above. Their results showed that the (110) surface is the most exposed with 74% follows by (100) and (111) surfaces with 16% and 10% respectively. However, the (110) surface shows two layers denoted as (110C) and (110D), where the (110C) is the most exposed layer[293].

III.2. γ -Alumina morphology

The morphology of γ-Al₂O₃ strongly depends on its preparation method. The common preparation way is the precipitation of aluminum salts in an aqueous solution to produce the hydrated precursor (Boehmite γ-AlOOH) which will after calcination at 700K, form γ-Al₂O₃. Thus, the morphology of γ-Al₂O₃ particles is inherited from the Boehmite particles structure and crystalize in a defect spinel structure[294] (Figure 13).

The DFT calculations[291] showed that the main change during the transformation process of boehmite to γ-Al₂O₃ is the collapse of the hydrogen-bonded layers, which leads to a contraction in the (010) direction. By combining these results with those obtained in the reference [295], the structure of γ-Al₂O₃ has been proposed. Moreover, according to the reference[296], the dried γ-Al₂O₃ chemisorbed at least a monolayer of water molecules when exposed to moisture at room temperature. And even after calcination at high temperature, the adsorbed water is believed to be a physiosorbed water form and hydroxyl groups bound on the surface. Furthermore, the desorbed water reacts at low temperature to form surface hydroxyls, while the adjacent hydroxyls condense at high

temperature to form water molecules which will then be evacuated according to the following reaction:

$$\sim OH + \sim OH \longrightarrow \sim O \sim + \square + H_2O \quad (2.3)$$

Where, the $\square$ represent the oxide vacant site.

On the other hand, the assumption proposed by A.A. tsyganenko[297] suggest that the adsorbed water molecule on the surface dissociates then to form a hydroxyl group bound to Al atom, whereas the remained H atom bound to the surface O atom.
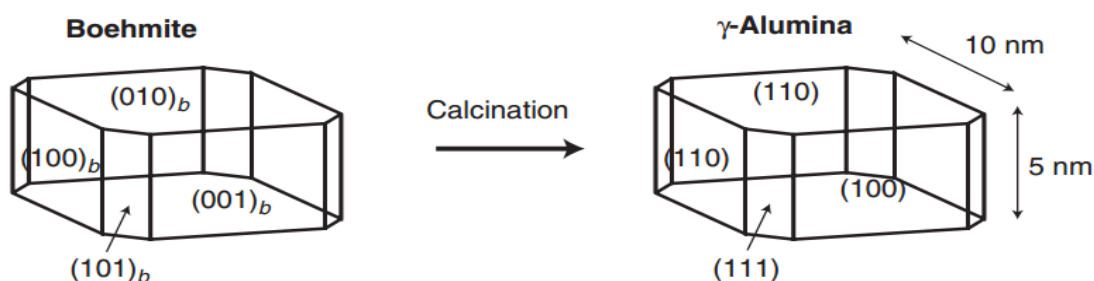
Figure 13. Topotactic transformation of boehmite into γ-alumina

III.3. γ-Al$_2$O$_3$ Bulk structure models

Starting from the supercell model of boehmite (AlOOH) and using MD to simulate its transformation to γ-Al$_2$O$_3$, Krokidis et al.[287] have proposed a bulk structure model for γ-Al$_2$O$_3$ (Figure 14.a). During the dehydration process, the Boehmite layers collapse together because of water molecules extraction and hydrogen transfer, as well as aluminum cations migrate from the octahedral to tetrahedral sites. Thus, the structure of γ-Al$_2$O$_3$ is described as a defective spinel model with some Al vacancies to satisfy the stoichiometry as denoted in the following formula: Al$_8$O$_{12}$, where the $\square$ represent the vacancy sites. Moreover, it has been concluded that the sublattice of oxygen atoms is FCC and the most stable structure of γ-Al$_2$O$_3$ consists of 25% of tetrahedral aluminum (Al$_{III}$). The simulated XRD were in agreement with the experimental one[290].

Furthermore, a non-defective spinel model consists of 8 Al_2O_3 units has lately been proposed by Digne et al[291]. The authors reported that this model was the most stable compared with other spinel models, moreover, it shows the ability of Al cations to occupy other than spinel sites which is the main difference among the other proposed models. However, this model does not perfectly represent the complexity of γ-Al_2O_3 as it has been derived from an industrial way process of boehmite transformation to γ-Al_2O_3. Besides that, it has been investigated under a realistic condition of temperature and water pressure which justify its reliability. Thus, it was nominated to be as a reference for surface modelling and catalyst reactions investigations. The details of the proposed γ-Al_2O_3 bulk are presented in table 1.

Table 6. γ-Al_2O_3 bulk properties [14]

Properties	Calc.
Cell volume ($Å3$/Al_2O_3 unit)	47.40
Al in tetrahedral site (%)	25
Cell parameters (*a, b, c*) ($Å$)[a]	7.90, 7.93, 8.07
Tetragonal distorsion (*c/a*)	1.02
Bulk modulus (GPa)	171
Electronic gap (eV)	4.9

[a] *a*, *b*, *c* parameters refer to an ideal spinel structure (for MgAl2O4, *a* = *b* = *c* = 8.08 $Å$).

Other spinel and nonspinel bulk structure models have been also proposed[298-303]. The traditional cubic defective spinel model[299] (Figure 14.b) of formula AB_2O_4 where A=B=Al, is presented as a unit cell contains four primitive cells Al_6O_8. Thus, to get the Al_2O_3 stoichiometries, three repetitive primitive cells with 2 Al vacancies are built. Moreover, the model with 40 atoms ($Al_{16}O_{24}$) where the spinel lattice has 2 Al vacancies at octahedral sites is used by computational simulation.

A nonspinel model with space groups of Fd3m and I41/amd containing 160 atoms supercells (Figure 14.c , 14.d respectively) have been published by [300]. This model is known as a defective cubic spinel structure. Moreover, the XRD experimental patterns agreed with the presented model. Although, the achieved spinel models and the model proposed by[288] showed an agreement with the experimental data, their quality remains inferior compared with the 160-atoms models [304].

Another model developed from pseudo-boehmite called H spinel γ-Al_2O_3 structure has recently proposed by dong at al[305] (Figure 14.f). The unit cell of this model consists of 2 octahedral cationic vacancies and one bulk H which was realized at high temperature.
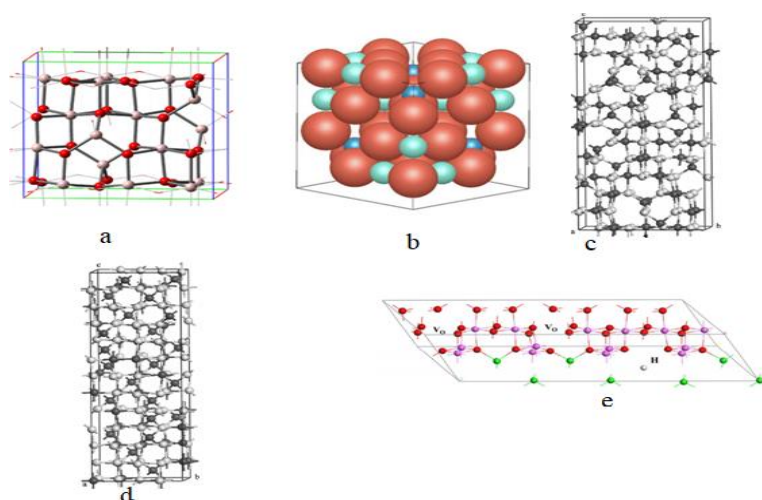
Figure 14. Different proposed unit cells for γ-Al_2O_3

III.4. γ-Al_2O_3 surfaces

Based on the experimental results of IR spectroscopy obtained firstly by A.A. tsyganenko et al.[297] and according to the achieved studies on the ability of hydroxyl groups to bound to different metal atoms[306, 307], the authors have supposed that the hydroxyl groups could be bound to a single metal atom, bridge two adjacent metal atoms and cap three adjacent metal atoms as showed in the Figure 15.
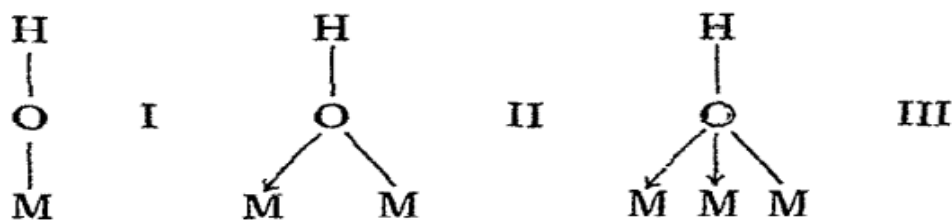
Figure 15.Types of hydroxyl groups bound to metal [20].

This assumption could interpret the different absorption bands obtained in the hydroxyl stretching region. Moreover, it is worth mentioning that the other absorption bands that appeared in the same region are reveal to the hydrogen-bonding between the adjacent hydroxyl groups.

Based on the precedent proposed bulk model, [291] have investigated the acid-base properties of different γ-Al_2O_3 surfaces.

III.4.1. (110) Surface

This surface is the most exposed in the crystalline structure (around 70 to 83% from the overall crystal shape). The 110 surface exhibits a rectangular oxygen atom sublattice in the spinel description. Moreover, this surface exhibits two types of unsaturated Al surface sites: octahedral Al atoms (Al_{IV}) representing 75% of twofold unsaturated sites and tetrahedral Al atoms (Al_{III}) representing 25% of onefold unsaturated sites resulting from the octahedral and tetrahedral Al atoms bulk. Regarding to the thermal stability, the hydroxyl groups in 110 surface shows a high stability even at high temperature comparing to (100) surface[288, 308].

Concerning the OH surface coverage, the model developed by M. Digne et al[290] shows the presence of both bound OH group to one single Al atom and bridged OH to two Al atoms. The presented model has been investigated as function of temperature (573K) and several OH surface groups (Figure 16). The results obtained agreed with the experimental

IR spectrum and MAS NMR[309]. The authors have also indicated the effect of the adsorbed water molecule and the Hydrogen-bonding interaction on the simulated spectral features. Moreover, it has been found that the OH concentration over the (110) surface decreases from 11.8 to 3.0 OH.nm^{-2} between 500 to 1000K[291].
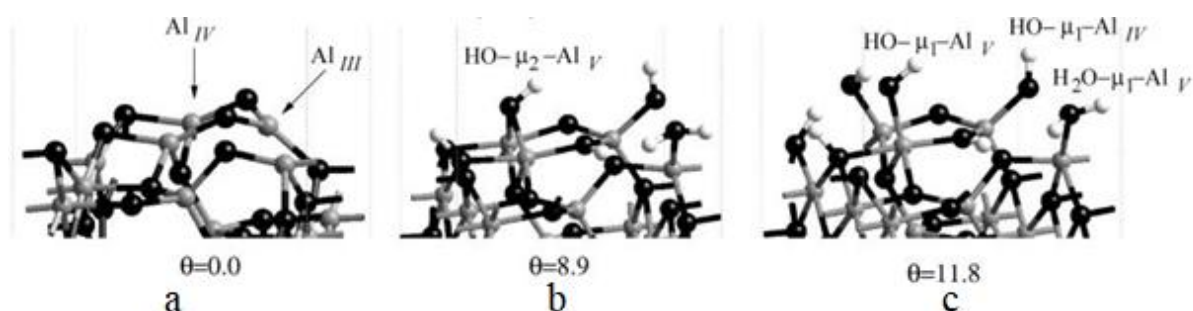
Figure 16. Different OH coverage of γ -Al$_2$O$_3$ (110) surface [14]

III.4.2. (100) Surface

According to the reference [310] the surface (100) corresponding to a square oxygen sublattice represent 17% from the overall area of γ-Al$_2$O$_3$ particle and it exhibits only a fivefold coordinated Al atoms (Al$_V$) and threefold coordinated oxygen atoms (μ$_3$-O) (denoted as I, II and III for Aluminum atoms and A, B, C for the oxygen atoms in the Figure 17).
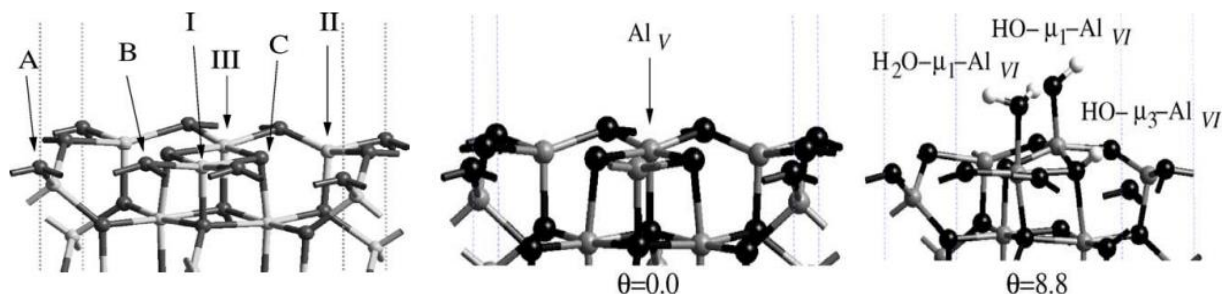
Figure 17. Different OH coverage of γ -Al$_2$O$_3$ (100) surface [14].

The (100) surface becomes totally dehydrated at a temperature higher than 573K indicating the transition of the Bronsted acid sites to Lewis acid sites[311]. Under this

temperature, the water molecules and hydroxyl groups bound to the one single Al atom, bridged two Al atoms, and bridged three Al atoms.

III.4.3. (111) surface

The (111) surface is completely hydrated at 800K and even at 1000K[291] the OH groups coverage is still high (9.8 OH nm^{-2}) due to the high coordination of μ_2–OH and μ_3–OH and a great number of hydrogen bonds which makes the dehydration of this surface costs high energy (Figure 18).
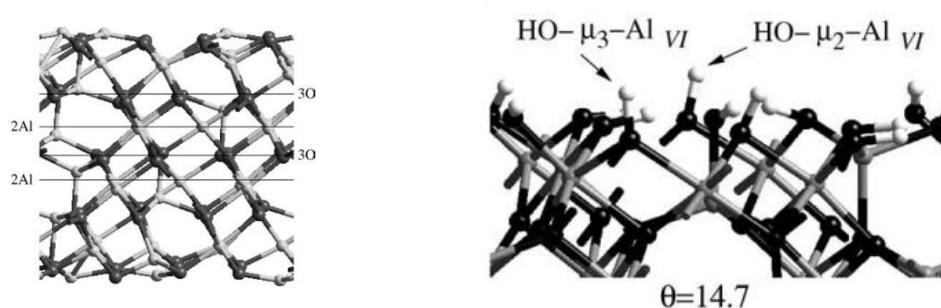
Figure 18. Structure and OH coverage of (111) surface [14].

The different modelled surfaces from various unit cells are summarized in the following table.[242]

Table 7. The modeled surfaces from different bulk structures.

Surface	Bulk	supercell	slabs	vacuum	OH, H$_2$O coverage	Cutoff energy	ref
100	Non spinel		8	12	8.8	300	[291]
110	Non spinel				8.9, 11.8 OH.nm^2	300	[291]
111	Non spinel				14.7 OH.nm^2	300	[291]
110	Non spinel	8.07 × 8.40	8	24		700	[308]
100	Non spinel	8.41 × 5.59		24		700	[308]
100	Non spinel	11.17×8.41×20.44 2x1	10	12	1 H$_2$O		[312]
110	Non spinel	8.41×8.07×19.17	6	12	1 H$_2$O		[312]
110	Non spinel	8.40 × 8.07 × 19.18	6	12			[313]
100	Non spinel	11.16 × 8.40 ×20.44 2x1	10	12			[313]
100	Spinel unit cell	18.9x 5.6x 5.6	5	15	1 H$_2$O	420	[314]
110D	Spinel unit cell	19.1x 7.9x 5.6	4	15	1 H$_2$O	420	[314]
110D	Spinel unit cell	21.9x 7.9x 5.6	6	15			[314]
100	Non spinel	(2x2) 11.14x 16.79	4		0		[315]
110	Non spinel	(2x2) 16.14x 16.79	4		8.9 OH.nm^2		[315]
100	Cubic	50x50x50			0		[316]
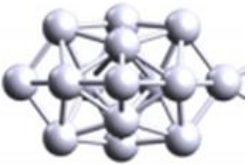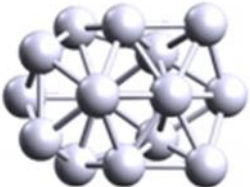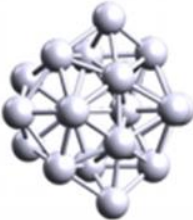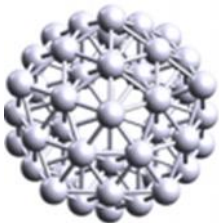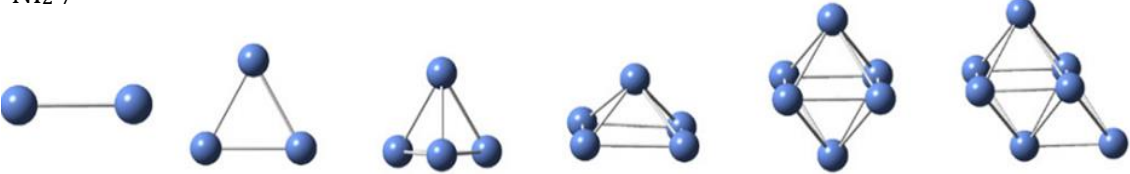
III.5. Ni sub-nano clusters

The sizes of the nickel sub-nano clusters used in dry reforming of methane DFT simulations typically range from a few atoms up to around 50 atoms. The exact size of the cluster used in a simulation may depend on the specific research question being addressed.

In general, smaller nickel clusters have been found to exhibit higher catalytic activity for dry reforming of methane. This is because smaller clusters have a larger surface area relative to their volume, which provides more active sites for the reaction to occur.

However, the choice of cluster size can also depend on other factors such as the stability and reactivity of the cluster under reaction conditions, and the computational resources available for the simulation. Researchers may need to balance these factors when selecting the appropriate cluster size for their study.

Table 8. Most investigated Ni clusters in the literature

Ni_{15}	Ni_{16}	Ni_{21}	Ni_{55}	[322]
Ni_{2-7}				[323]

Ni_4/Al_2O_3	Ni_7/Al_2O_3	Ni_{13}/Al_2O_3	Ni_{55}/Al_2O_3	[166, 312, 324]
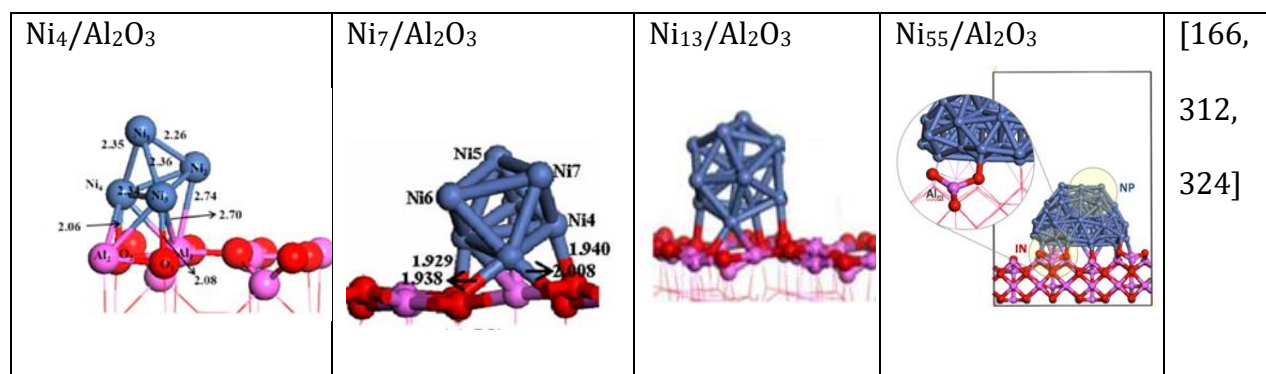
III.6. Ni-based supported systems

Here we reported the most Ni systems, and Ni-based supported on different surfaces systems used as catalysts models for different chemical reactions, including isolated extended surfaces and clusters, supported Ni clusters on different surfaces, and monometallic, bimetallic and trimetallic systems.

Table 9. most used Ni-based systems as catalysts models

System	reaction	ref
Isolated clusters		
Ni_4	CH_4 dissociation	[325]
Ni_{1-55}	CH_4, CH_3adsorption	[322]
Ni_{13}, Fe_{13}, Cu_{13}, Co_{13}	CH_4 dissociation	[326]
Ni_{13}, Ni_{55}	CO_2 dissociation	[327]
Cu-Ni-Pt core shell	DRM	[328]
Ni_{13}, Cu_{13}, $Ni_{12}Cu$	Activity towards ammonia decomposition reaction	[329]
Ni_3Au	CH_4 dissociation	[330]
Supported systems		
$Ni_4/\gamma-A_2O_3$	CH_4 dissociation	[166, 331]
$Ni_4/\alpha-A_2O_3$	CH_4 dissociation	[332]
Ni_4/Al_2O_3, Ni_3Fe/Al_2O_3	CO methanation	[333]
Ni_3Fe/Al_2O_3, Ni/Al_2O_3, Ni_3Cu/Al_2O_3	CO_2 hydrogenation to CH_4	[334]
Ni_6/Al_2O_3	CO adsorption	[335]
Ni_{1-7}/Al_2O_3	Effect of OH groups on the stability of Ni_{1-7} clusters	[336]
Ni_{13}, Co_{13}/Al_2O_3 (110)	Aldehyde Hydrogenation on pure Al_2O_3 (110)	[337]
Ni_{13}/Al_2O_3 (100), (110)	CO_2 Activation on Ni_{13}/Al_2O_3 (100), (110) pure surfaces	[327]
Ni_1/CeO_2	CH_4 dissociation	[338]
Ni_1, Fe_1, Co_1 / CeO_2(111)	CH_4 activation over CeO_2 surfaces modified by transition metals	[339]
$Pt_{1-5, 13}$ /Al_2O_3 (110),(100)	CO_2 activation	[340]
Ni_{13}/CeO_2, Ni (111)	CO, NiO formation, CH_4, H_2O dissociation	[341]
Ni_{15}/ZrO_2	DRM	[171]
Ni_4/ZrO_2, Ni_{13}/ZrO_2 (111)	CO hydrogenation	[342]
Ni_{13}/TiO_2(110)	SRM	[343]
$Ni_{4,8,12}$ / MgO (100)	Effect of the Ni cluster size on the DRM, CH_4 and CO_2 dissociation	[344]
Ni_8Rh_1/h-BN, Ni_9/h-BN	DRM	[345]
Pd/Cu (111)	CH_4 dissociation	[346]
Ni_{1-3}, Co_{1-3} incorporated γ-Al_2O_3(110)	system stability	[347]
Ni_2Fe overlayer of Ni (1 1 1)	CH_4, CO_2 dissociation, C, CH oxidation	[155]
Fe_2O_3-Ni, Fe_2O_3-NiO	Adsorption of Hydrogen	[348]
PdO/SnO_2(110), Pd/SnO_2(110)	Methane oxidation	[349]
$Ni_{4,9,13}/TiC$(001)	CH_4 activation	[350]
Ni_2Co_2 / MgO	H_2 adsorption/desorption	[351]
Monometallic extended surfaces		
Ni (111), (100) (553)	CH_4 dissociation	[166]
Ni (111), (110), (100),	DRM	[352]
Ni(111) (211)	Coke formation	[177]

Co (111) (221) (211) (110) (100)	C removal	[353]
Bi-metallic extended surfaces		
Ni-Co (111), Co (111), Ni (111)	CH_4 activation	[354]
Ni-Sn	DRM	[168]
Ni-Cu	DRM	[355, 356]
Ni-Fe Ni_4Fe (1 1 1)	CO_2 methanation	[357]
Ni-Pt	DRM	[167, 358]
Ni-Mo	DRM	[359]
Ni-Rh, Ni-Ru	CH_4 dissociation, CO formation	[360]
Ni–M (M = Cu, Ru, Rh, Pd, Ag, Pt, Au)	CH_4 dissociation	[361]
Ni - Au	CO adsorption	[362]
Tri-metallic extended surfaces		
Pt_3 clusters decorated Co@Pd and Ni@Pd model core-shell	ORR	[363]
Ni-Fe-W oxides	NH_3 dissociation	[364]
Pt–Pd–Ni	ORR	[365]
Pt-Fr-Ni, Pt-Cu-Co… core shell cluster	ORR	[366]
Pt-Cu-Ni core shell cluster	ORR	[367]

Although CH_4 dissociation has been extensively studied on various Ni surfaces and clusters, few DFT studies have reported on the effect of the γ-Al_2O_3 support (for Ni/γ-Al_2O_3 systems) on CH_4 dissociation. To our knowledge, no DFT study has been conducted on the dissociation of CH_4 on Ni_{13}/γ-Al_2O_3. Furthermore, no CO_2 or CH_4 dissociation has been reported on Ni_x-M_y/γ-Al_2O_3 (x > 10) (M=Co, Mo, Cu, etc.). Additionally, in the DRM process, the surface model of γ-Al_2O_3 (110) has not considered hydroxyl groups.

Chapter IV

Experimental and DFT calculation work

IV.1. Introduction

The nature and type of the active metal affects the catalytic performance of the dry reforming of methane reaction. The effect of using transition metal Co and noble metal Pd as a promoter on a $Ni/\gamma-Al_2O_3$ catalyst for the DRM reaction will be investigated in this chapter. The objective is to optimize the content of the active phase necessary to carry out the dry methane reforming reaction while obtaining a suitable conversion.

The reactions were carried out at atmospheric pressure and 750°C to study the effect of the promoter on the conversions of CH_4 and CO_2 and carbon deposition. Different characterization techniques have been used for the synthesized catalysts.

The severe conditions of reforming reactions can cause sintering and/or carbon deposition on the active metal surface leading to catalyst deactivation. Several research have shown that all Group VIII metals are suitable catalysts for DRM. Some authors argue that nickel-based catalysts could play an important role in the catalytic action of DRM, owing to their numerous properties, relatively high activity, and stability. Consequently, during the DRM and under certain conditions the deactivation of the catalyst by sintering or by the formation of carbon on the active surface of the metal which is connected to the structure of the catalyst and its composition always remains a major problem for this reaction. Many studies have been directed towards minimizing the deactivation of Ni-based catalysts.

The researchers found that the addition of alkaline earth oxides and/or rare earth oxides to the catalysts plays a beneficial role on the catalytic properties of Ni and significantly reduces the formation of coke on the surface of the catalyst by the formation of carbonates, or oxycarbonates [1]. Several recent reviews have reported the use of Co or Pd as a promoter for the dry methane reforming reaction. In addition, it should be noted

that the carbides of transition metals like Co and Mo show catalytic properties like those of noble metals. Recent research indicates that unsupported β-Mo2C type catalysts are catalytically active for the DRM showing good thermal stability and high resistance to coke deposition [2].

In this part, the conversion of methane by the dry reforming process is studied in the presence of promoted nickel-based catalysts at different Ni, Co and Pd contents, to evaluate their catalytic performances for this reaction.

First, we will synthesize two types of catalysts based on nickel and Co, Pd to define the most efficient catalyst. The influence of different operating parameters such as temperature on the performance of the reaction as well as on the formation of carbon were also studied. The catalysts studied are characterized after the whole tests to study their final state and to explain any changes in their catalytic activity.

IV.2. Experimental work

IV.2.1. Synthesis of catalysts

As already mentioned, the choice of nickel as a catalyst for the DRM reaction is based on their excellent catalytic performance. For our study, the synthesized catalysts are (1%Ni and 1% Ni-Co) supported on the metal oxide which is alumina (γ-Al$_2$O$_3$). The synthesized catalysts must be stable under the operating conditions so the active phase must be well dispersed on the support.

IV.2.1.1. Experimental protocol for the preparation of catalysts

Numerous researchers have explored various techniques for catalyst preparation. According to Shan et al [6], the preparation methods significantly influence both the structural properties and the catalytic performance of the catalyst. In our study, the

method we have chosen to synthesize our catalysts by using incipient wetness impregnation. For this, commercial alumina (Puralox) was used as support. An exact quantity of nickel nitrate $Ni(NO_3)_2.6H_2O$ (Sigma-Aldrich) was dissolved in a calculated volume of distilled water corresponding to the pore volume of alumina to obtain 1% by mass of nickel.

For the bimetallic catalyst, an appropriate amount of $Co(NO_3)_2.6H_2O$ (Sigma-Aldrich), was dissolved in the solution of the nickel precursor, in the right proportions to obtain catalysts promoted with 1 mol% Co.

The mixture is placed under a humid atmosphere for 5 hours for the maturation phase, then overnight in an oven at 60°C to be dried.

Once the drying is completed, it is imperative to proceed with an oxidizing pre-treatment. The purpose of calcination is to eliminate metal precursors (nitrates) to obtain metals in oxide form. The sample is calcined at 500°C for 4 hours with a temperature rise (ramp) of 2°C per minute.

Then, the last step to obtain an active catalyst for the catalytic conversion of methane by CO_2 is the reduction step. This step is a so-called reducing pretreatment, because it allows the transition from the oxide phase to the metallic phase. The reduction is performed directly in a fixed-bed catalytic quartz reactor, with a constant flow of a mixture of nitrogen (20 mL/min) and hydrogen (20 mL/min), prior to the catalytic dry reforming test. The reduction temperature is maintained at 700°C for 1 hour.

IV.2.2. Catalysts characterizations

IV.2.2.1. XRD Analysis

Analysis by X-ray diffraction (XRD) is the best known of the crystallographic methods used to identify the different crystalline phases and to follow the structural modifications occurring during the different treatments. The principle of this technique is based on sending an X-ray beam on the sample deposited on slightly hollowed pyrex supports. When the beam reaches the sample (with an angle θ already chosen) and is diffracted by an angle θ then detected by a scintillation counter. By reflection, the diffracted ray obeys Bragg's law: $n\lambda = 2d \times sin\theta$, Knowing that:

d: distance of two reticular planes, n: diffraction order, 2θ: angle formed by the incident and diffracted beams, λ: wavelength of the X-ray beam.

In our work, XRD analysis has been used at room temperature in a D8 PASSEUR advanced equipment with Cu–Kα radiation (λ = 1.5404 Å) to identify the different crystalline phases and to follow the structural modifications occurring during the different treatments. The ranges canned was from 10° to 80° with a 0.02° step size at a scan rate of 0.05 s^{-1}. The average particle size was calculated using the Scherer's equation: D = Kλ / (B.cosθ) where D is the mean size of the ordered crystalline domains (in A°), K is dimensionless shape factor whose value was taken at 0.9, the X-ray wavelength λ = 1.54056 Å and B (rad) is the full width half maximum (FWHM), θ (rad) the Bragg angle.

IV.2.2.2. in situ- XRD Analysis

The catalyst reduction was studied by in situ- XRD analysis. The catalysts were reduced to 700°C with a ramp of 10°C.min^{-1} under 3 vol% H_2/N_2 (5 ml min^{-1}). A diffractogram is recorded at every 100°C. The radiation used is the Kα of copper (λ = 1.54059 Å) and the

scanned angular range is 2θ = 10–80°, with an increment of 0.05° and a counting time of 1 second for each position.

IV.2.2.3. SEM-EDX analysis

SEM-EDX analysis is a powerful tool in materials science and chemistry, which refers to the use of a scanning electron microscope (SEM) in conjunction with energy-dispersive X-ray spectroscopy (EDX) to analyze the elemental composition and distribution of a sample.

In our work, the SEM-EDX analysis of the calcined and reduced samples were carried out using an electronic microscope model MET FEI TITAN Themis 300.

IV.2.2.4. ThermoGravimetric Analysis (TGA)

ThermoGravimetric Analysis (TGA) is a thermal analysis technique that measures the change in the weight of a sample as a function of temperature or time under a controlled atmosphere.

In TGA, a small quantity of the sample is placed on a sensitive balance and subjected to controlled heating in the presence of air in a furnace. As the temperature increases, the sample undergoes thermal decomposition or other chemical reactions, resulting in a change in its weight. The weight change is measured continuously and recorded as a function of temperature or time.

To quantify the coke formed on the used catalysts and identify the nature of carbon present, ThermoGravimetric Analysis (TGA), coupled with Differential Scanning Calorimetry (DSC), was performed.

IV.2.3. Catalytic test

The performances of the catalysts were evaluated in DRM reaction. The catalytic tests were carried out in a fixed bed catalytic reactor at atmospheric pressure. The purpose of which is to study the different reactions of reforming methane into synthesis gas (H_2+CO) also to assess the influence of certain parameters such as temperature...etc.

IV.2.3.1. Principle of the device

The experimental frame illustrated in the Figure 20 comprises three parts:

- A gas supply and regulation system.

- The tubular catalytic reactor with fixed bed placed in a furnace whose temperature of heating is controlled by an external thermocouple.

- Online analysis of the output composition of the gas mixture by chromatography in the gas phase. The Agilent 3000 Micro GC is a powerful gas chromatograph designed for rapid gas stream analysis in fuel cell development and the hydrocarbon processing industry. Equipped with a micro thermal conductivity detector (TCD) and standard injector heating, it ensures accurate and efficient analysis. Its modular design allows for quick reconfiguration and repair, ensuring long-term, trouble-free operation. Each channel requires an analytical column and offers flexibility in injector options.

The assembly also includes a bypass circuit, a pressure sensor, and a valve millimeter to regulate the pressure and a trap to recover the water formed.

IV.2.3.2. Introduction and regulation of gases

The gases used for this experimental study are methane and carbon dioxide as reagents and nitrogen which serves as an inert standard. All gases come from bottles of gas under pressure equipped with manometers. The gases are sent to the reactor at known flow rates and controlled by pressure regulators: mass flow "Brooks" type SLA5850 and

5850TR, controlled by a regulator electronic 0254, 4 channels which allows us to manage mass flowmeters.

The total volumetric flow rate of the gases introduced is kept constant for all the catalytic tests. The gaseous ratio of reagents and diluent ($CH_4:CO_2:N_2$) is equal to (33.33 : 33.33 : 33.33).

A three-way valve connects the gas supply system and the reactor. It allows either to inject the gases into the reactor, or to short-circuit the reactor (by-pass) and to send the gases directly to the analyzers, to identify and quantify the gases injected before the reaction (white). All the gases resulting from the reaction are collected in a condenser. The reaction was performed with a GHSV of 6210.191 h^{-1}.

IV.2.3.3. Description of the catalytic reactor

The reactor used in this work is a tubular quartz reactor with an inner diameter of 1 cm and an outer diameter of 1.1 cm. The reactor loading is done from below due to the presence of a thermowell that allows for temperature monitoring inside the reactor.

The catalytic bed is divided into two parts, with a zone of SiC upstream of the catalyst separated by quartz wool to limit pressure drop and ensure the stability of the catalytic bed. After introducing a known mass of catalyst (100 mg) into the middle of the reactor, the height of the catalytic zone is determined to be 1.1 cm.

The reactor is then placed into a straight furnace that envelopes the catalytic zone, with the temperature of the reaction determined by a thermocouple placed in the oven and connected to an automatic regulator (EUROTHERM). The regulator allows for temperature control and rate of temperature increase.
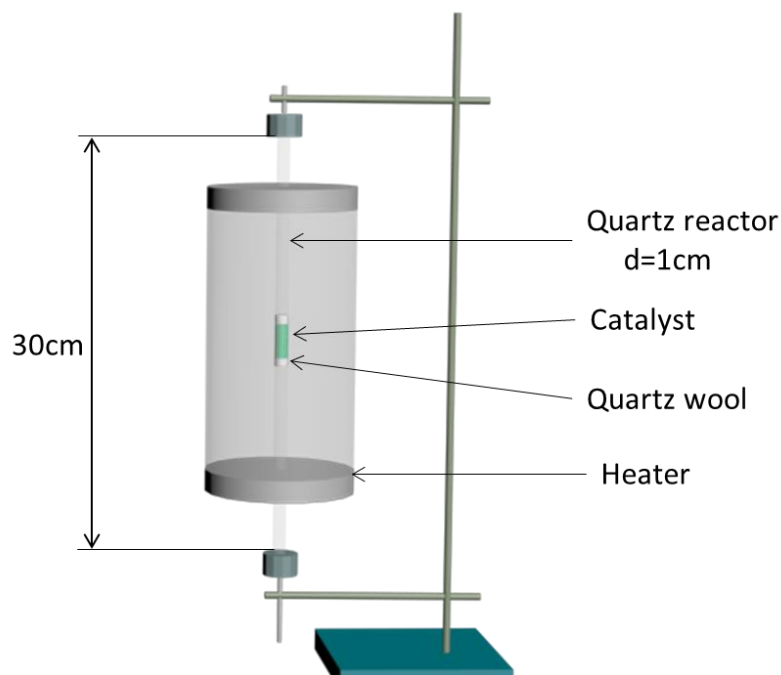
Figure 19. Catalytic reactor

IV.2.3.4. Gas analysis

Gas analysis of all the resulting gaseous compounds was performed using a gas chromatograph. The composition of these products was determined online at atmospheric pressure using an injection valve system to the Agilent 3000A micro-chromatograph, which was equipped with a conductivity detector (TCD).

The TCD detector was coupled with a "filled" chromatographic column of type Altech CTR-I, with molecular sieve and permeable polymer, allowing simultaneous quantification of N_2 (as the internal standard), CH_4, residual CO_2 from the reaction, and CO produced during the reaction.

In our study, the analysis and quantification of compounds were performed using a thermal conductivity detector (TCD). The detector was connected to an integrator that

calculated the peaks areas of the compounds present at the reactor outlet. Chromatographic analysis was performed by injection every 5 minutes.
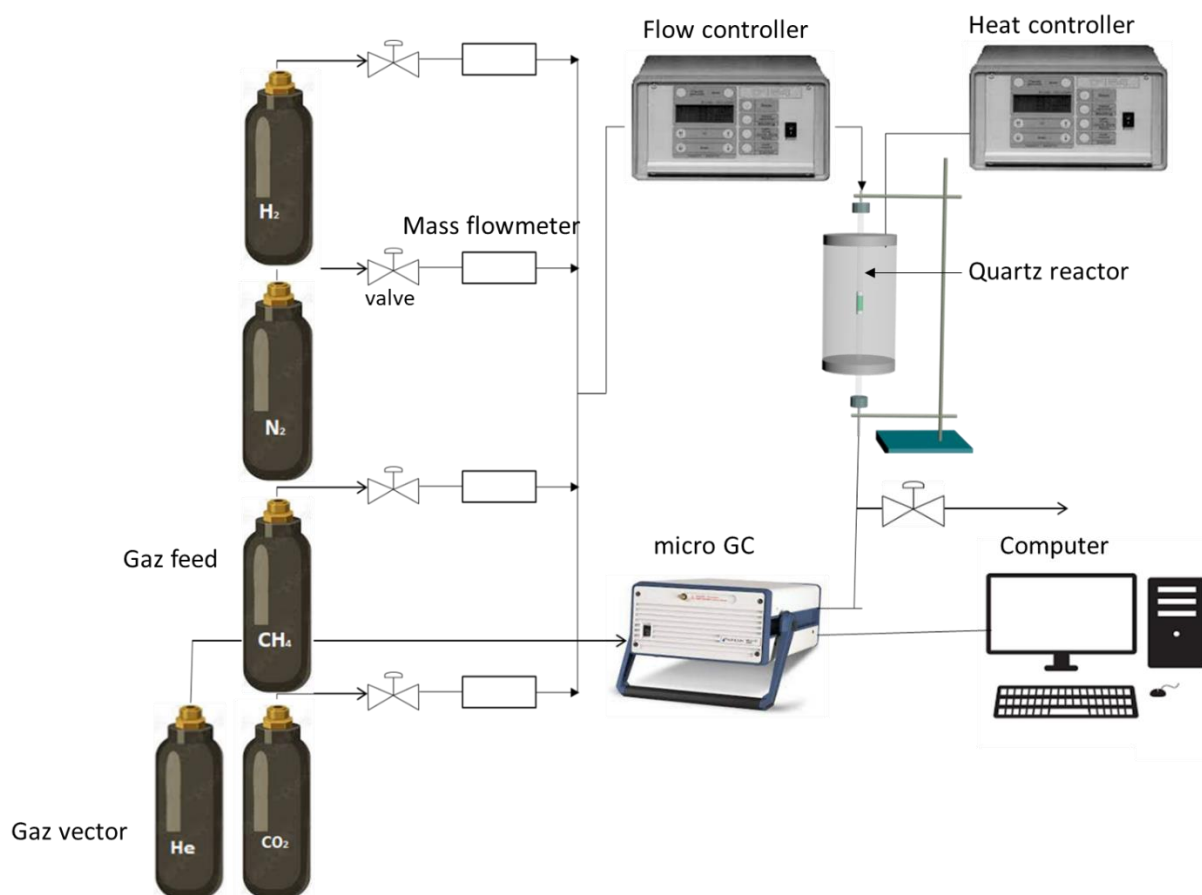
Figure 20. Scheme of gas analysis setup

Table 10. Operating conditions for the analysis of gaseous effluents

Columns	TCD: CTR I column 6 x ¼ outer & 6 x 1/8 inner
Temperature injector	50°C
Temperature detector	TCD : 100°C (filament :100°C)
Gaz vector	Helium

IV.2.3.5. Mode and operating conditions

The dry methane reforming reaction is performed under atmospheric pressure in the gas phase. The temperature range of the experiments for all the tested catalysts is 750°C.

Reduction or pre-activation is a necessary step to reach the reducibility of different oxidized species and obtain the most active form of the catalyst.

In our case, it is necessary to reduce the catalyst and therefore have the nickel and cobalt in metallic form before testing its catalytic performance. For this study, we chose to reduce the 1% Ni (1%) Co catalysts under a total hydrogen and nitrogen flow of 40 mL/min at a temperature of 700°C for 2 hours with a ramp of 2°C/min.

Afterward, the sample is purged under a flow of nitrogen (20 mL/min) for 1 hour until it reaches the test temperature and before admitting the flow of the reaction mixture. The CH_4/CO_2 feed mixture is an equimolar mixture, and the total gas flow rate introduced is maintained constant at 30 mL/min (33.33% CH_4, 33.33% CO_2, and 33.33% N_2). Then, the analysis of the reaction mixture at the outlet of the reactor is carried out using a gas chromatograph every 10 minutes.

The values obtained from the chromatogram make it possible to quantify the conversion of the reactants and the selectivity of the products. The following formulas are used for the calculations:

The conversion of reactants CH_4 and CO_2, denoted XCH_4 and XCO_2 respectively, are the fraction of reactants in gaseous products.

$$XCH_4(\%) = \frac{CH4,E - CH4,S}{CH4,E} \times 100$$

$$XCO_2(\%) = \frac{CO2,E - CO2,S}{CO2,E} \times 100$$

CH4,E, CO2,E: respective numbers of moles of CH_4 and CO_2 entering the reactor.

CH4,S, CO2,S: respective numbers of moles of CH_4 and CO_2 leaving the reactor.

The product selectivity, noted SP, is given by the following formula:

$$SP\ (\%)\ = \frac{(np,S - np,E) \times \alpha R}{nR,E \times \alpha P} \times 100$$

$p,, np,S$: number of moles of the products P initially present and at the exit.

$nR,$: respective numbers of moles of reactants R.

αR, αP: stoichiometric coefficients respectively of the reactant and product at the equilibrium of the reaction.

For example, in the case of carbon monoxide selectivity, we obtain:

$$SCO\ (\%)\ = \frac{nCO,S}{XCO2 \times nCO2,E + XCH4 \times nCH4,E} \times 100$$

$nCO,$: CO outlet mole number.

IV.3. DFT calculation

IV.3.1. Computational models

IV.3.1.1. Bulk model

Herein, we have reconstructed the bulk model proposed by Digne et al[317](Figure21). All calculations are performed at GGA-PBE level, the cut-off energy for geometry optimization is 300 eV and the k-point set 4x2x2. The grimme method for DFT-D correction was applied to calculate the van der waals interactions. The total energy converged to be less than 2.10^{-5}eV/atom, the max force and max displacement are less than 0.05 eV/atom and 0.002 Å, respectively.
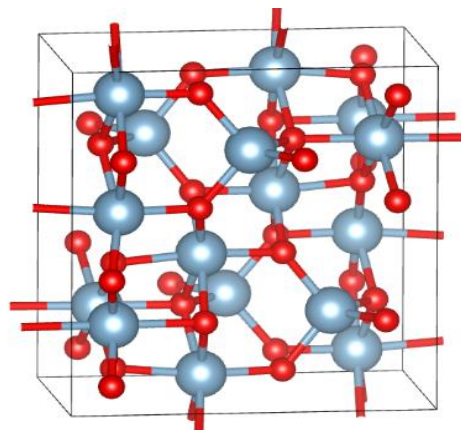
Figure 21. The reconstructed bulk model (a=5.587, b=8.413, c=8.068, β = 90°)

The calculated Partial density of state (PDOS) for the reconstructed γ-alumina bulk seems

similar as the calculated PDOS of the proposed model by Digne et al.(Figure22).
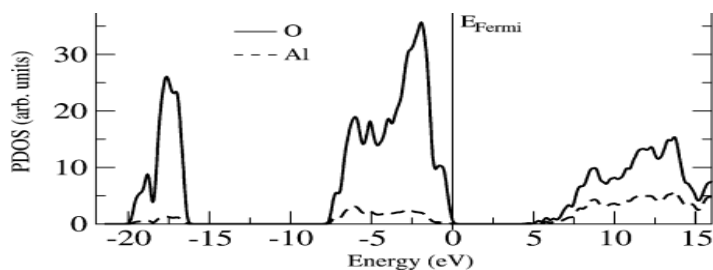
Calculated PDOS for reconstructed *γ* -alumina bulk
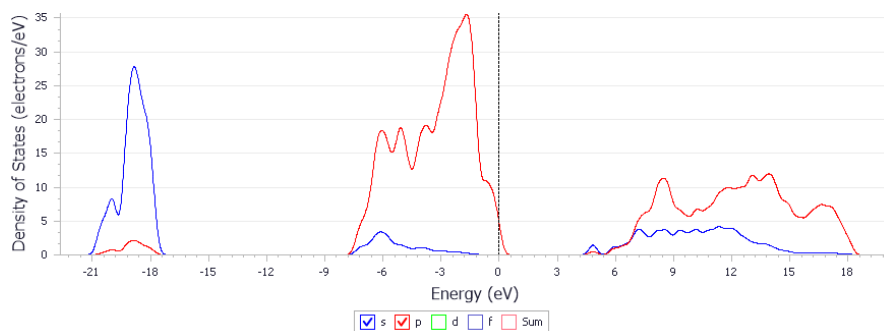
Calculated PDOS for the *γ* -alumina bulk model by Digne et al.[317]

Figure 22. PDOS for the γ -alumina bulk model

IV.3.1.2. Hydroxylation of (110) Surface model

According to Digne et al[317], the relaxed Al_2O_3(110) surface exhibits lower Al

coordination: three Al_{III} atoms and one Al_{IV} atom inherited from the bulk tetrahedral and

octahedral atoms respectively, while the oxygen atoms exhibits μ_2–O and μ_3–O

coordination's .

The OH coverage is formed by dissociative adsorption of the water molecules over the metallic sites on the γ-Al_2O_3 surface and the hydroxylation/dihydroxylation process for the studied surface is described by the following equilibrium [312, 317]:

$$\text{Surface hkl} + \text{nadsH}_2\text{O(gas)} \leftrightarrow [\text{Surfacehkl, nadsH}_2\text{O}] \quad (1.4)$$
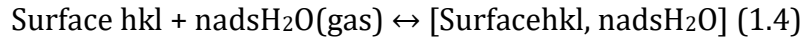
Thus, different OH coverage of γ-Al_2O_3 (110) surface as a function of temperature have been investigated by Digne et al.[290]. The first water molecule adsorbs on the Al_{III} site and adjacent O–μ_2–(Al_{III}, Al_{IV}) site represent a surface coverage of 3 OH nm^{-2}, the other three adsorbed molecules occur on Al_{IV} sites to form Al_V sites as following : HO–μ_1–Al_V, H_2O–μ_1–Al_V, and HO–μ_2–(Al_V, Al_V) with a surface coverage varying from 5.9 to 11.8 OH nm^{-2}. Finally, the two last water molecules adsorb on the Al_V site to form Al_{VI}. However, since the OH surface coverage depends on the pre-treatment temperature, the OH concentration is determined at the standard outgassing temperature 573K and found to be θ_{110} = 11.8 OH nm^{-2}. Other recent studies[308, 318, 319], have also investigated the OH coverage on the alumina surface in function of temperature and water pressure10^{-4} < P (H_2O) < 10^{-6} to reproduce the experimental observed water coverage.

The (110) surface model was cleaved from the bulk derived from Digne model and was optimized without changes. The constructed slab was modeled as 2x2 supercell with a dimension of 16.1 × 16.8 × 28.0 $Å^3$ occupied by a thickness of 4 layers where the two bottom layers were fixed on their bulk position whereas the top layers allowed to relax. A vacuum of 22Å was applied to avoid the interaction among crystal faces produced by the periodic boundary conditions. Although the (110) surface is the most exposed surface, it is not stable in the dehydrated form, thus, the hydrated (110) surface is considered in this investigation for more realistic metastable termination. For that purpose, it has reported[319] that in the experimental conditions of water pressure 10^{-4}

< P (H_2O) < 10^{-6} bar and temperature 700 K < T < 800 K (773K in our case), the (110) surface exhibits a hydroxyl density of 3 OH nm^{-2} and 9 OH nm^{-2}. However, to reduce the computational cost, we have only selected the 3 OH nm^{-2} coverage corresponds to 4 adsorbed H_2O molecules on the 2x2 surface. This surface has also been investigated in previous DFT studies. R. Wischert et al[308] found that the adsorption of one H_2O molecule on the Al_{III} site is highly exoenergic with and an adsorption energy of -2.342 eV and the dissociated H_2O yielding a terminal OH bonded to Al_{III} to form (Al_{VI}-OH) and the H atom bonded to O_{2b}. Ana T. F. Batista et al[319] have also studied the same OH coverage in addition to 6, 9 and 12 OH nm^{-2} , their results showed that the adsorbed hydroxyls in the surface involves in the H bonding, and most of them are H-bond donors resulting in high chemical shift.
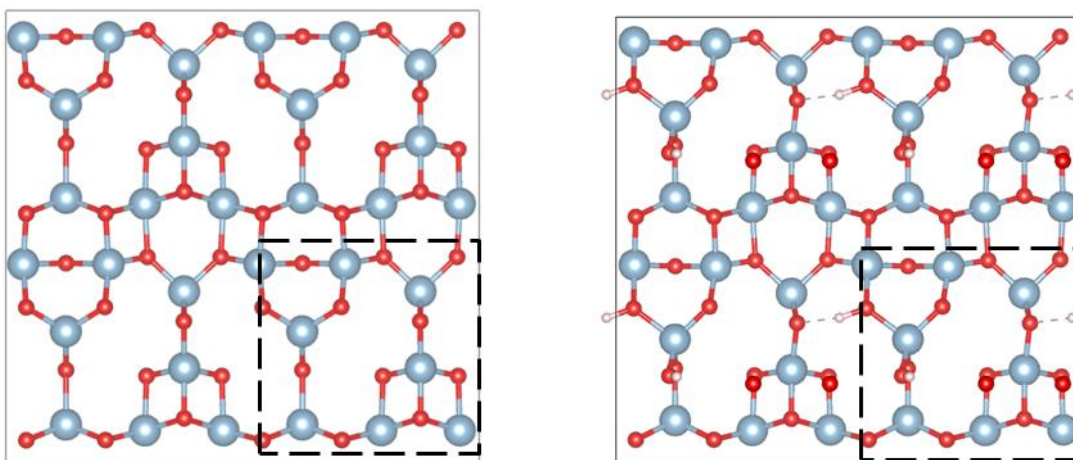
Figure 23. (2x2) surface a: dehydrated surface, b: hydrated surface 3 OHm^{-2}

For the Ni interaction on the support surface, many Ni clusters have been reported in the literature. Li et al[166] have investigated the interaction of Ni_4 cluster on both spinel and non-spinel γ -Al_2O_3 surface, the results obtained showed the same metal-support interaction effect for the both systems. Liu et al[312] have investigated the stable configuration of isolated (2-7) than the interaction of most stable Ni_n cluster on different γ-Al_2O_3 surfaces including single Ni atom, their results showed that the hydroxylated

(110) surface was unfavorable for (2-7) cluster adsorption stability, and the hydroxyl groups lead to decrease the metal-support interaction, which suggest that γ-Al_2O_3 support inhibit metal cluster aggregation and favor the formation of high dispersed particles. More recently, many studies have investigated the stable configuration of Ni clusters consisting of 2-16, 21 and 55 atom[321, 364, 365]. The cluster model used by[365] consisted of 55 Ni nanoparticle was much closer to technical Ni catalyst than the most common clusters (n<10). Using transferable tight-binding potential and molecular-dynamics simulation method with simulated-annealing techniques, C. Luo[366] has determined the stable geometry configuration of Ni_2–Ni_{19} cluster. Furthermore, W. Song et al[367] have studied the magnetic and electronic properties of Ni_n (n =<30) and found that the $Ni_{6,13}$ can be highly stable with a small magnetic moments.

After structural relaxation of the γ -Al_2O_3 (110) surfaces, the optimized Ni_{13} and Co_1-Ni_{12} clusters are added to different sites of pure and hydroxylated γ -Al_2O_3 (110) surfaces to achieve the most stable configuration representing the Ni /Al_2O_3 catalyst. Then, the CH_4, CO_2 and C species were added on different sites of the modeled systems to determine their most stable configurations.

IV.3.2. Computational Method

Periodic spin-polarized density functional theory calculations were performed by means of the Vienna Ab Initio Simulation (VASP) packages, using the projector augmented wave method53 and the exchange-correlation Perdew-Burke-Ernzerhof (PBE) functional54. A rotationally invariant GGA+U correction55 was employed to consider the strongly correlated character of the localized Ni-d electrons, where the Hubbard U and J parameters were fixed to 3.0 and 0.9 eV, respectively. In addition, the Grimme's D2 formulation was included to take into consideration the van der Waals

interactions between the DRM species or the small clusters and the alumina surface. The alumina (110) surface has been modeled using a periodic supercell of two Al atomic layers and four O atomic ones with a cell dimension of (16.83 x 16.14 x 28° A). A vacuum region of 3 nm was used to separate the periodically repeated pure and supported (DRM species and/or small Nin clusters) alumina slabs. The integration over the Brillouin zone was sampled by 2×2×1 k-points using a Gaussian integration method with a width of 0.1 eV. We have used an energy cutoff of 450 eV for the plane wave functions and 10^{-6} eV to ensure the convergence of the total energy. The structural relaxations of the supported DRM species and/or small Ni clusters over alumina surfaces were performed by nullifying the forces on the relaxed atoms with a precision of 10^{-5} eV/° A.

Finally, the adsorption species on the corresponded surfaces was calculated as following:

$$E_{ads} = E_{adsorbates/slab} - E_{slab} - E_{adsorbates} \ (2.4)$$

where $E_{adsorbates/slab}$ is the total energy of adsorbates on the surface, E_{slab} is the total energy of the surface slabs and $E_{adsorbates}$ is the total energy of free adsorbates, respectively.

IV.4. Results and discussion

IV.4.1. XRD analysis of fresh calcined and reduced catalyst samples

XRD analysis was used to examine the crystalline structure of the calcined, reduced and the spent catalysts. For the calcined catalysts (Figure 24) the XRD pattern showed no crystalline phases of Ni and NiO from all unreduced samples, suggesting either that Ni/NiO were highly dispersed on both catalysts even following high temperature calcination (500 °C), or instrumental detection limit due to the low Ni loading.
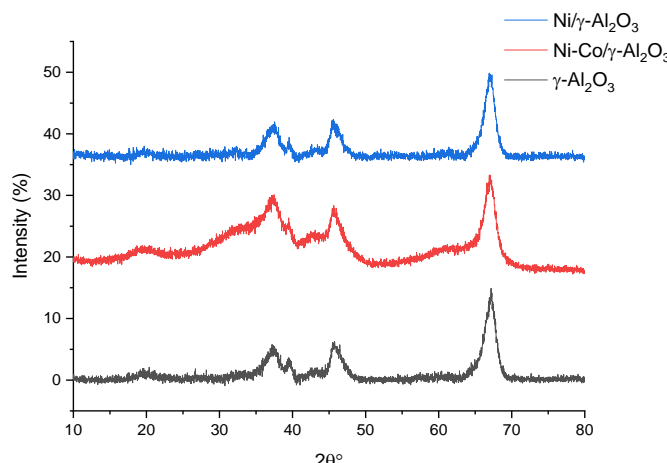
Figure 24. XRD patterns for Alumina, Ni and Ni-Co supported on alumina at room temperature.

a)   b)
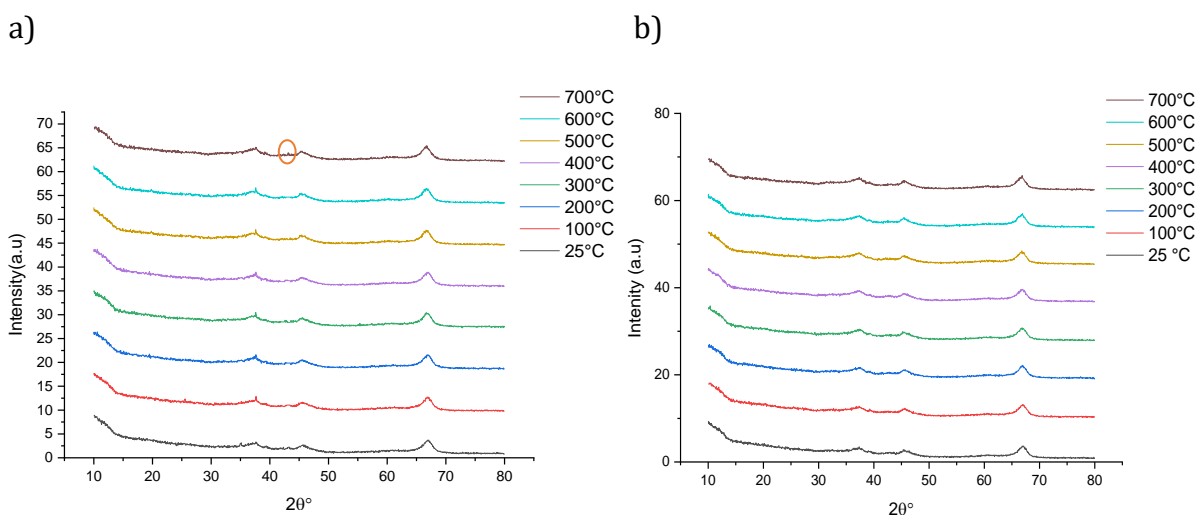
Figure 25. in-situ XRD patterns for Ni (a) and Ni-Co (b)supported on alumina.

For samples subsequently reduced under H_2 at 700 °C (Figure 25), only 1wt% Ni sample

shows reflections characteristic of (111) nickel metal surface at 44.6°. However, no peaks

correspondent to Ni particles have been detected for the bimetallic Ni-Co/ γ-Al_2O_3

catalyst, suggesting that the introduction of Co inhibited the sintering of Ni nanoparticles.

IV.4.2. SEM-EDX analysis

All prepared samples of monometallic and bimetallic catalysts, including the calcined and

reduced ones, were examined by high-angle annular dark-field scanning transmission

electron microscopy (ac-HAADF-STEM), including aberration correction, to identify the

nature of the supported Ni species. The obtained magnification images for the calcined

catalysts clearly revealed the exclusive presence of Ni nanoparticles for the Ni/γ-Al$_2$O$_3$

catalyst. However, for the bimetallic Ni-Co/γ-Al$_2$O$_3$ catalysts, the images showed the

presence of sub-nanoclusters, confirming the role of Co addition in the high dispersion of

Ni, as shown in Figures 26 and 27.
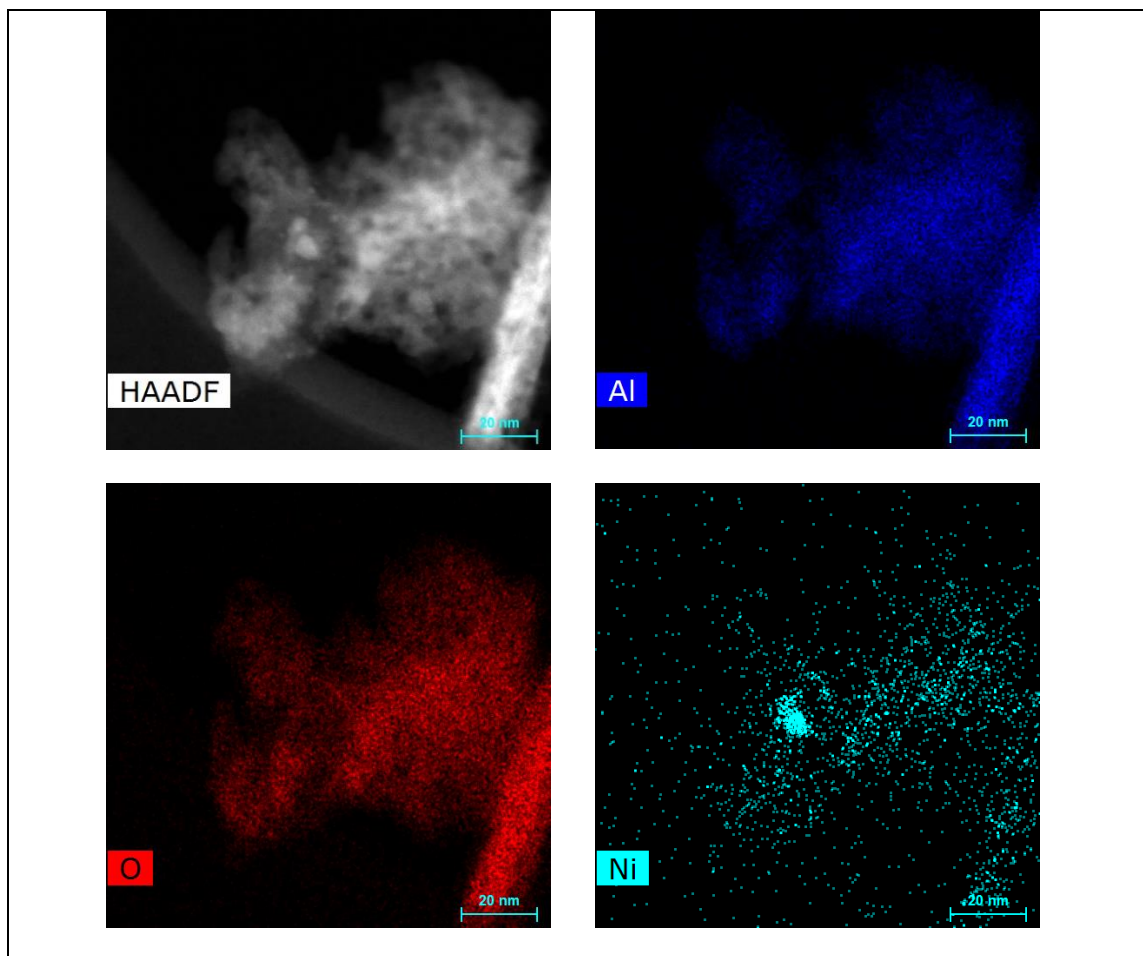
Figure 26. HAADF-SEM, EDX mapping images of calcined sample 1%Ni/Al$_2$O$_3$. Elemental

mapping legend: (bleu) Aluminum, (red) oxygen, and (green) Nickel.
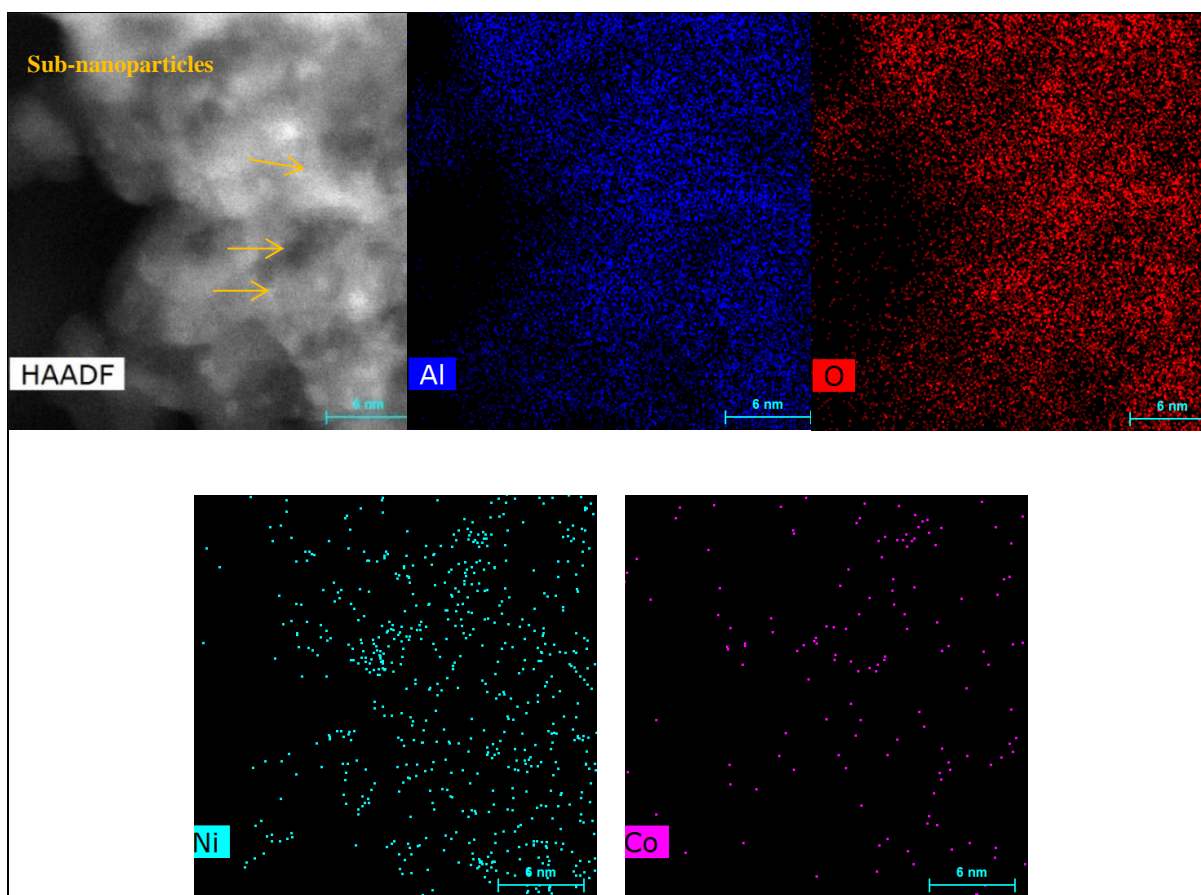
Figure 27. HAADF-SEM, EDX mapping images of calcined sample 1%Ni-Co (90%Ni 10%Co)/Al$_2$O$_3$. Elemental mapping legend: (bleu) Aluminum, , (red) Cobalt, and (green) Nickel

The magnified images obtained for the reduced monometallic and bimetallic catalysts shown in Figures 28 and 29 revealed that, after reducing the prepared catalysts at the operating temperature, the size of metallic particles increased compared to the calcined ones. However, the detected particles remained well dispersed on the support surface, which is beneficial for avoiding catalyst deactivation by sintering.

Moreover, it is evident from Figure 29 that the size of the Ni particles in the bimetallic catalyst differs from the monometallic catalyst, as they exhibit a more dispersed distribution. This difference can be attributed to the inclusion of Co, thus confirming the role of Co in promoting particle dispersion.

Figure 28. HAADF-SEM, EDX mapping images of reduced sample 1%Ni/Al$_2$O$_3$. Elemental mapping legend: (bleu) Aluminum, (red) oxygen, and (green) Nickel.
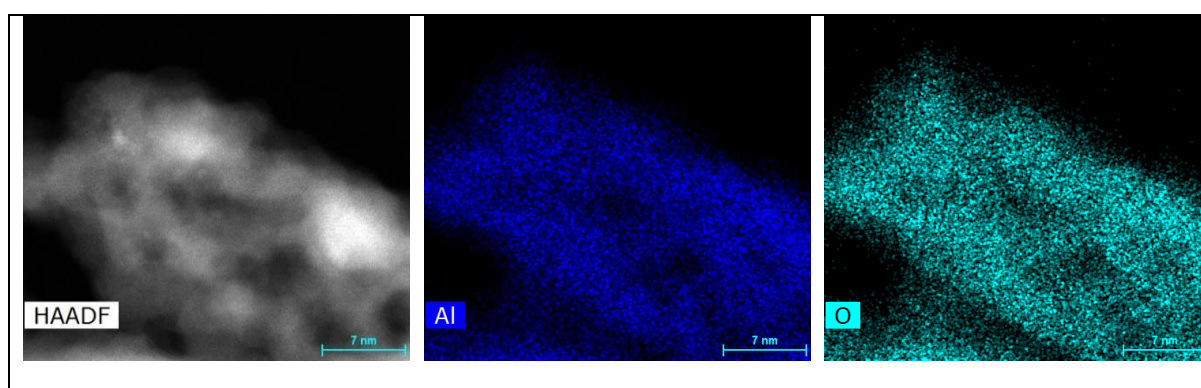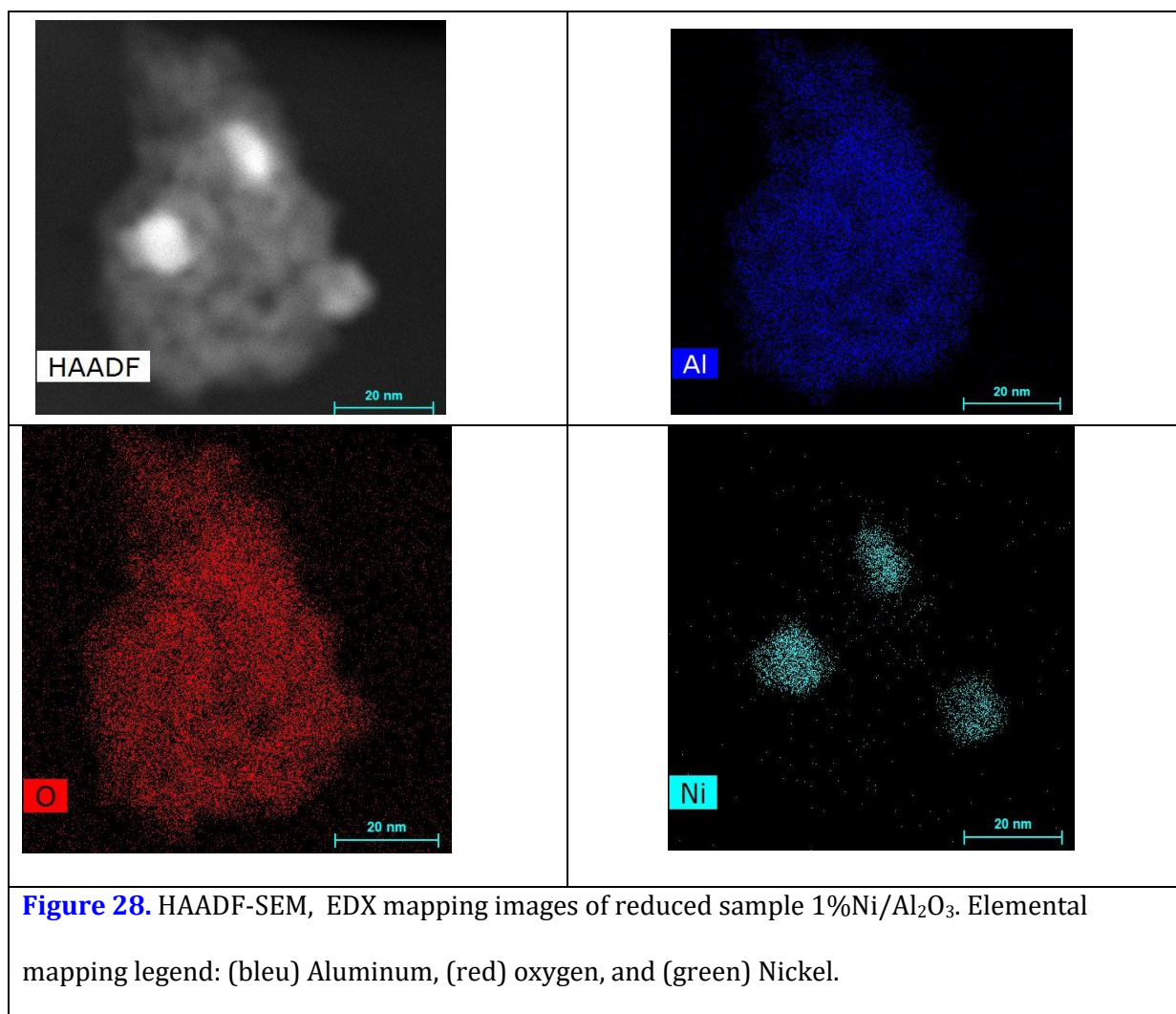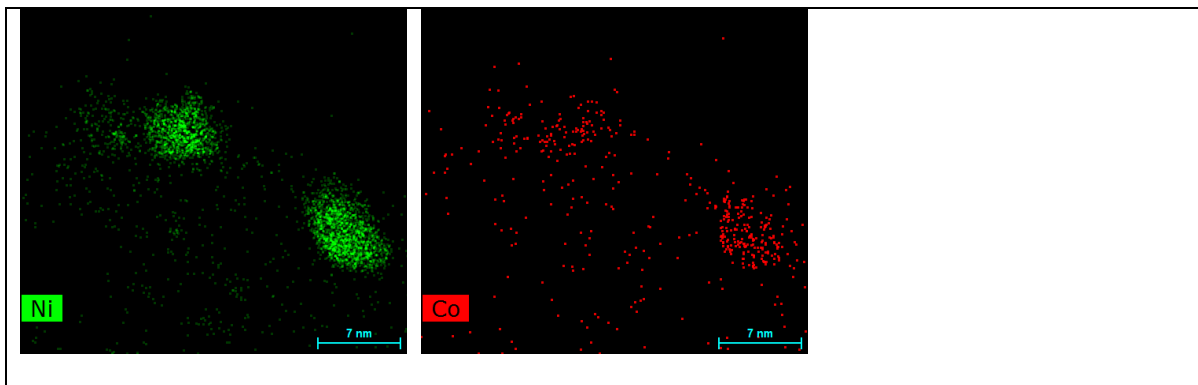
Figure 29. HAADF-SEM, EDX mapping images of reduced sample 1%Ni-Co/Al$_2$O$_3$. Elemental mapping legend: (bleu) Aluminum, (blue) oxygen, (green) Nickel, red (cobalt).

IV.4.3. Catalysts activity

Several gas compositions and catalyst amounts have been considered to determine the optimal gas hourly space velocity (GHSV) that provides maximum conversion and selectivity. The best compromise between convertion and selectivity is obtained for a Ni loading content of 1mg and GHSV of 60.000 ml/g.h.

(a)

(b)
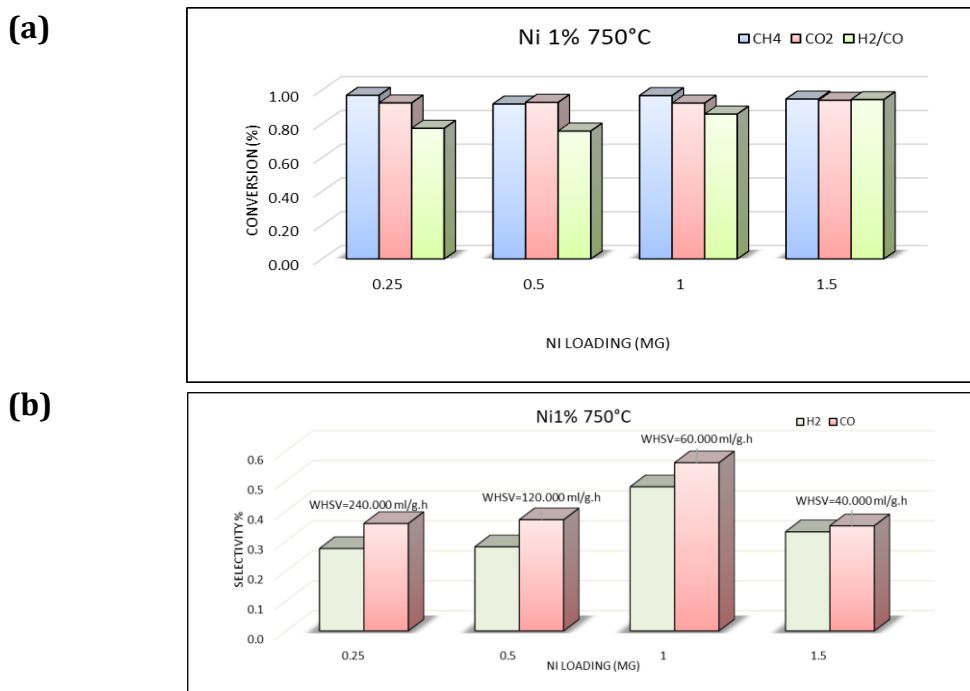
Figure 30. The optimal Ni loading (a) and GHSV (b).

Different nickel-based catalytic systems were synthesized and tested to compare the effect of the Co content on the activity of the dry methane reforming reaction and the deactivation of the catalysts. Figure 31 (a,b) shows the influence of the Ni/Co ratio on the conversion of methane and CO_2 between 0 and t (min). The stability of the catalysts is evaluated in the temperature of 750°C.

Importantly, both catalysts display activity from the start of the reaction as well as catalytic stability until deactivation. The results show that the conversion of CO_2 is greater for both catalysts.

This result can be explained by an overconsumption of CO_2 by the reaction of (RWGS) which is a side réaction of dry methane reforming reaction. This reaction consumes CO_2 and amount of H_2 produced and leads to the production of CO and H_2O:

$$CO_2 + H_2 \leftrightarrow H_2O + CO \qquad \Delta_R H_{25°C} = 41 kJ/m \quad (3.4)$$

It is worth noting that metallic nickel is widely acknowledged as the active phase in the RWGS reaction as well as the dry reforming reaction of methane. Furthermore, it is evident that the catalytic activity is influenced by the concentration of the promoter present [15].

In addition, the CH_4 conversion is high. This result indicates the presence of the methane cracking reaction which causes the formation of solid carbon deposition causing the deactivation of the catalyst.

Moreover, in terms of stability, both 1% Ni and 1% Ni1Co catalysts show excellent stability during the catalytic tests at high temperature. The conversions of CH_4 and CO_2 undergo the same evolution for both catalysts, with their conversions respectively

reaching about 97% and 90%. However, regarding the selectivity of H_2 and CO Figure 31

(c,d), for Ni catalyst the value of CO and H_2 reach 70% and 40% respectively in the first 4

hours, and then start decreasing until they reach the value 50% and 30% respectively. In

contrast to the Ni-Co catalyst, both H_2 and CO selectivity remained stable around 65%,

40% value for Ni-Co catalyst during 18 hours of testing. This result underscores the

critical significance of employing a bimetallic catalyst to greatly augment both stability

and selectivity, highlighting the crucial role it plays in enhancing these essential aspects.
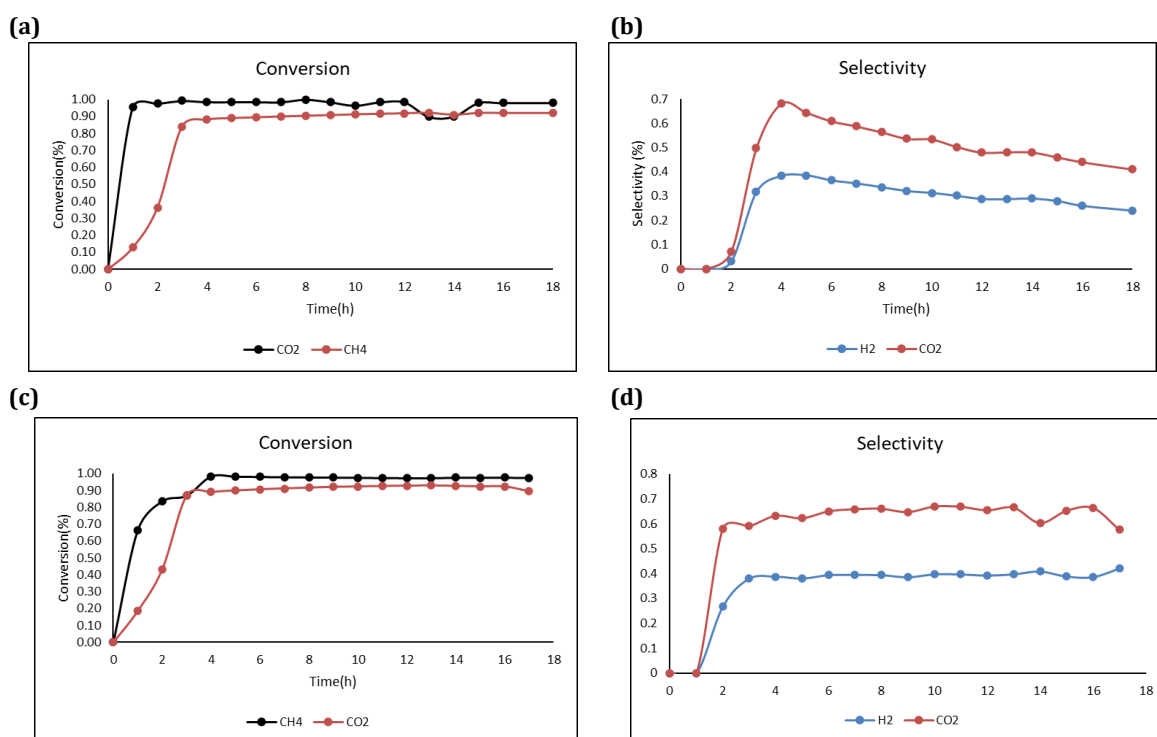
Figure 31. Conversion and selectivity evolution of DRM species on the Ni/Al$_2$O$_3$ (a,b) and Ni-Co/Al$_2$O$_3$ (c,d) systems.

IV.4.4. The effect of temperature

The reaction temperature is a parameter that has an important impact on the catalytic

activity. The DRM reaction is carried out in a temperature range between 500°C and

750°C at atmospheric pressure and a CH$_4$/CO$_2$ ratio fixed at 1, with the aim of studying

the evolution of the dry methane reforming reaction as well as the reactivity of the

catalysts. Figure 32 (a) illustrates the conversion of methane as a function of temperature. The results obtained compare the reactivity of the two catalysts.

The conversion of methane increases significantly when the reaction temperature is increased for both catalysts. The first important remark of these results is that the two solids show good activity in the range of temperatures studied. At T=550-600°C, a clear difference is observed between 1Ni-Co and 1Ni. The 1Ni-Co catalyst presents an activity larger and allows a conversion of 90%, however, a value of 80% was obtained for 1Ni catalyst.

Figure 32 (b) represents the evolution of CO_2 conversion as a function of reaction temperature for 1Ni and 1Ni-Co catalysts. It is noted that the two catalysts exhibit a remarkably high conversion of CO_2 in the temperature range 600-750°C. It is also noted that the CO_2 conversion increases with the reaction temperature.

We observe that the results are quite close. For a temperature of 600°C the conversion values for 1Ni and 1Ni-Co are equal to 90% and 80%. These conversions increase up to 97% and 98% respectively at T=750°C.

It is obvious that $1Ni1Co/Al_2O_3$ is more suitable in the dry reforming reaction of methane due to its excellent activities and stability and low promoter content (1% by mass).

Figure 32 (c) represents the selectivity evolution on the 1Ni and 1Ni-Co catalysts as a function of the temperature. It was found that the H_2 selectivity was slightly higher with the 1Ni-Co catalyst than with the Ni catalyst in the temperature range of de 500 °C to 600 °C, and above this temperature the two selectivity became similar.

The CO selectivity curves Figure 32 (d) show a slightly higher value for the Ni catalyst in the temperature range of 600°C to 750°C compared to the 1Ni-Co catalyst. Moreover, it is

also observed that the selectivity for both catalysts increase with the temperature rise. This may be due to the presence of the RWGS reaction at a lower temperature as seen previously.

(a) CH$_4$ conversion

(b) CO$_2$ conversion

(c) H$_2$ selectivity
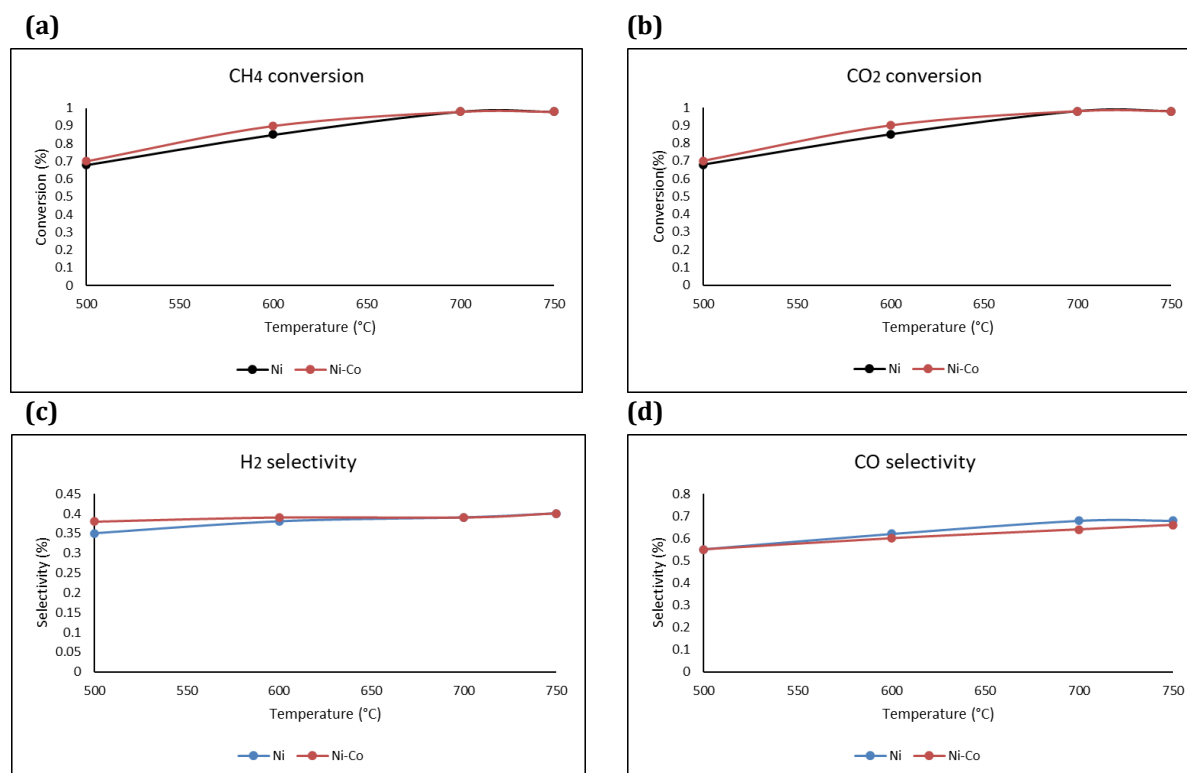
(d) CO selectivity

Figure 32. Temperature effect on the conversion of CH$_4$ (a) and CO$_2$ (b) and selectivity of H$_2$ (c) and CO (d).

IV.4.5. Anti-coke effect

Thermogravimetric analyses (TGA) were preformed to evaluate the amount of carbon formed on the surface of the spent catalysts after 28h. The mass decrease observed on the TG curves is caused by the oxidation of carbon deposition. A higher mass decrease indicates a greater amount of carbon on the surface. Figure 33 shows TG plots in the form of percentage of mass decrease as a function of temperature. The highest mass decrease, equal to 5.3%, was observed in the case of the Ni/Al$_2$O$_3$ catalyst compared to the Ni-Co/Al$_2$O$_3$ where it was 4.5%. The obtained results showed the higher carbon resistance of the low metal loading in the prepared catalysts and the effect of adding Co to Ni/Al$_2$O$_3$

where the carbon deposition was slightly less important. These results are in good agreement with the SEM-TEM analysis results where it has been shown that the metallic phase was highly dispersed on the support. Thus, we can conclude that high dispersion of the metallic phase is a parameter that contibutes to the resistance of carbon deposition. The better resistance to carbon deposition in the Ni-Co/Al_2O_3 comes from the effect of the Co addition, suggesting that co-metallic interaction is another key parameter to consider. Moreover, it is well known that carbon oxidation below 250 °C is referred to as atomic carbon, while carbon oxidized in the range of 250–600 °C is categorized as amorphous. Graphitic carbon, on the other hand, is formed at temperatures above 600 °C. Based on our results and the information provided in the literature, we can conclude that the carbon deposited on the catalyst is most likely of a graphitic nature.
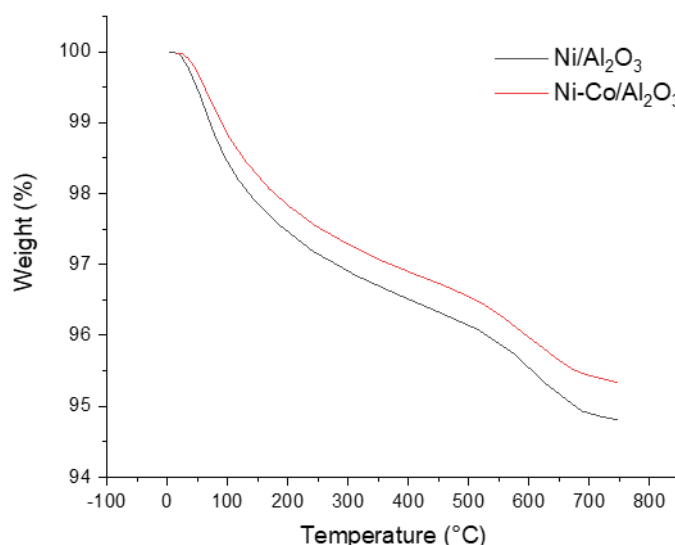
Figure 33. Thermogravimetric analyses (TGA) of Ni/Al_2O_3 and Ni-Co/Al_2O_3 systems

IV.4.6. Anti-sintering effect of Co addition to Ni-Al_2O_3 catalyst

Based on the most stable adsorption configurations of the Ni and Ni-Co clusters on the alumina surface, the metal-support interaction energies were determined.

For the most stable configuration of the adsorbed Ni_{13} cluster on alumina surface, it was found that the Ni atoms interacted with the Al_{III} in the surface due to its acidity, it was also observed that the Ni atoms were bonded to the O atoms of the alumina surface. The correspondent interaction energy of this configuration was -5.57 eV, indicating the strong interaction between the metal and the support. Moreover, the presence of OH groups have no effect on the metal-support interaction, since the interaction energy of the Ni cluster on the hydroxylated alumina surface was -5.58 eV.

On the other hand, the most stable configuration of the Ni cluster doped Co atoms was obtained and presented in Figure B. 34. The obtained structure showed that the cobalt atoms were bonded to the O atoms of the surface, however, the Ni atom was bonded to the acid Al_{III} site. The correspondent interaction energy of this configuration was -6.03 eV, which is higher than that obtained with the pure Ni_{13} cluster. This result showing the effect of the addition of Co to Ni in enhancing the metal-support interaction, which is a vital parameter in heterogeneous catalysts since it allows to increase the electronic delocalization between the metal and the support and thus avoid the sintering phenomena. Similarly, to the pure Ni cluster, we have also noted that there was no effect.

(a)   (b)

E_{int}=-5.57 eV E_{int} =-5.58 eV

$E_{int} = -6.03$ eV $\qquad\qquad\qquad$ $E_{int} = -6.06$ eV
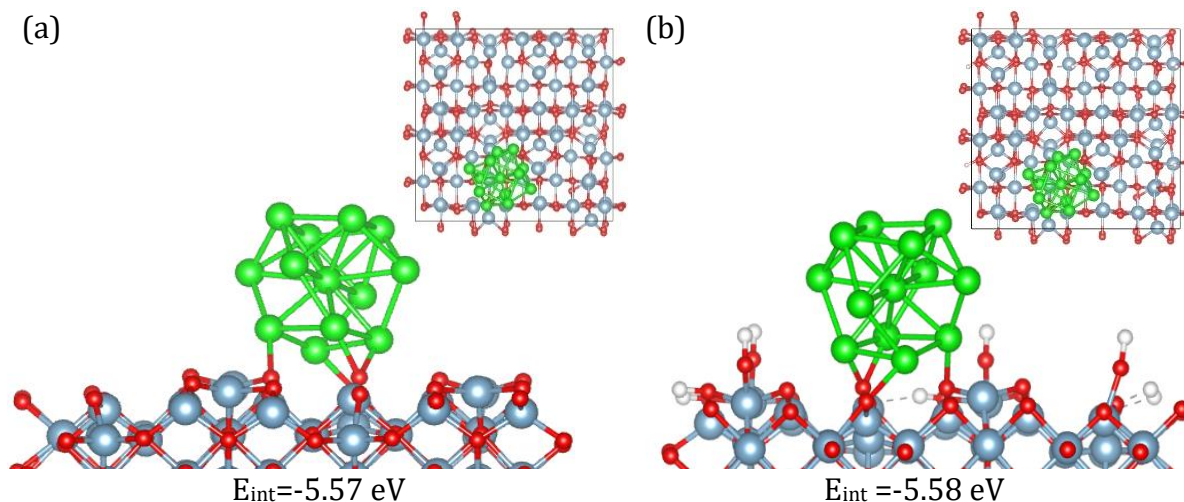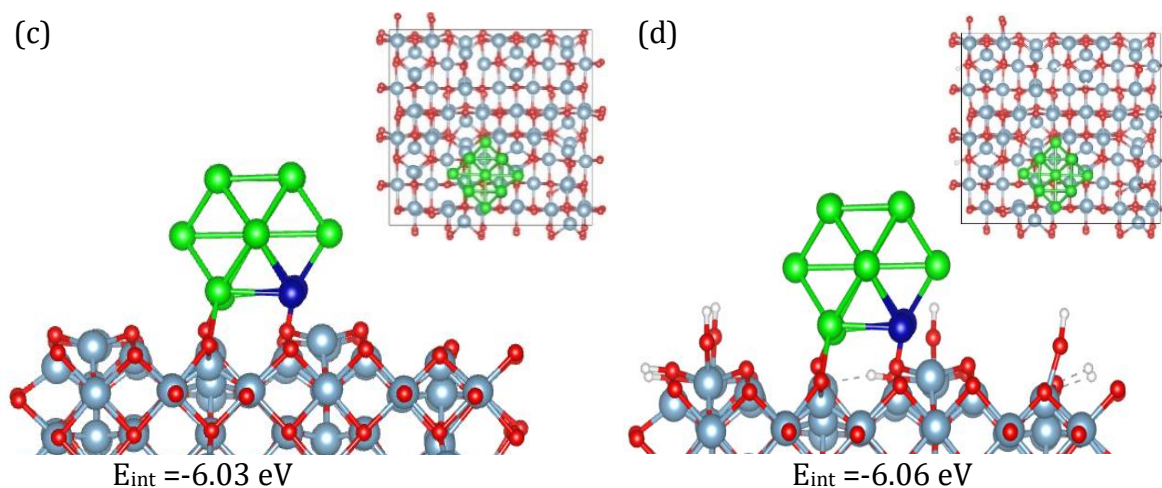
Figure 34. Most stable configurations of (a) Ni/Al$_2$O$_3$, (b) Ni/Al$_2$O$_3$-OH, (c) CoNi/Al$_2$O$_3$ and (d) CoNi/Al$_2$O$_3$OH.

IV.4.7. CH$_4$ adsorption

The adsorption of CH$_4$ has been investigated on Ni and Ni-Co catalysts. The obtained results showed that the CH$_4$ was physically adsorbed on both Ni and Ni-Co catalysts surfaces, and there have been no bonds between the CH$_4$ and the catalysts surfaces. However, the adsorption energy of CH$_4$ on the Ni-Co catalyst was slightly higher compared to the Ni catalyst which indicates the effect of Co doping to Ni catalyst, guiding to change the properties of catalyst, and enhancing the CH$_4$ adsorption.

Moreover, the study conducted by P. L. Rodríguez-Kessle et al. [321] revealed that the adsorption energy of CH$_4$ on the pure Ni$_{13}$ cluster was -0.30 eV, which is lower than the value obtained in our study using the supported Ni$_{13}$ and Ni$_{12}$-Co clusters on the alumina surface. This finding highlights the influence of the support on the reactivity of CH$_4$. The presence of a support plays a significant role in shaping the reactivity of CH4, as strong adsorption on the catalyst surface can enhance reactivity by facilitating the formation of reactive intermediates and providing favorable conditions for subsequent reactions.

a)   b)

E_{ads} =0.31eV E_{ads} =0.44eV
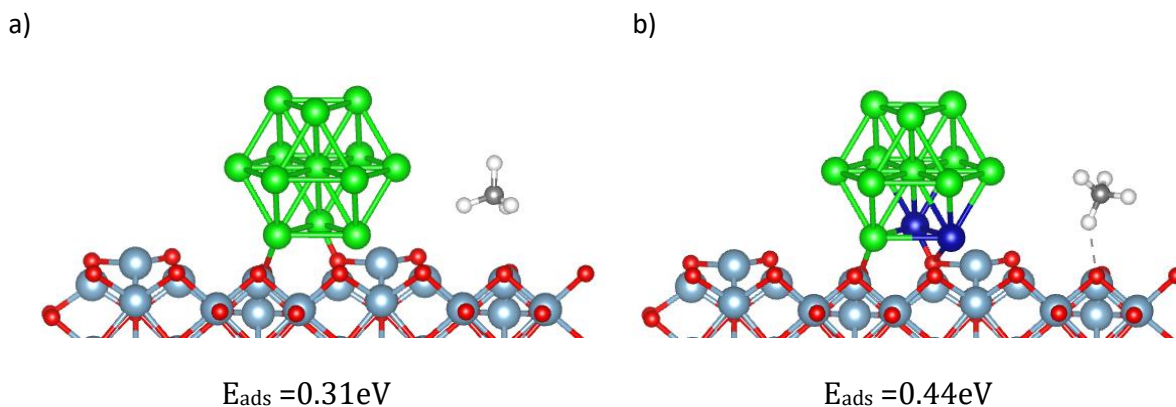
Figure 35. Most stable configuration of the adsorbed CH_4 on a) Ni_{13}/Al_2O_3 and b) Co_2Ni_{11}/Al_2O_3

IV.4.8. CO_2 adsorption

The most stable configurations of the CO_2 adsorption on the Ni and Ni-Co catalysts surfaces have been presented on Figure 36. Regarding the CO_2 adsorption on the Ni catalyst, it has been found that the most stable configuration shows that the CO_2 adsorbed in the interface site between the Ni cluster and the alumina surface, where both O and C atoms have been bonded to the same Ni atom, whereas the left O atom was bonded to Lewis's acid site (Al_{III}). The adsorption energy of CO_2 in this system was 0.35. It is worth mentioning that the same system has been studied by Silaghi et al. [323] and they found the same configuration obtained in our study. Moreover, they revealed that the interaction of CO_2 on Ni was higher in the presence of the alumina support compared to the pure Ni cluster confirming the crucial role of the presence of the support.

Regarding the CO_2 adsorption on the Ni-Co catalyst, the obtained results showed that the adsorption energy of CO_2 on Ni doped Co was higher compared to the non dopped system. This result reveals that the Co presence can modify the electronic properties of the catalyst's system and enhances the interaction of the CO_2.

The results discussed above show that the Ni and Ni doped Co catalyst was highly active compared to the pure Ni catalyst system investigated in previous studies [321,323]

justified by the strong interaction between the CH_4 and CO_2 species and the studied catalysts systems. These results confirm those obtained by the experimental work, where we have noticed a high activity of the CH_4 and CO_2 with a slightly high activity on Ni-Co catalyst system compared to the Ni catalyst system.

a)   b)

E_{ads}= 0.25eV E_{ads} =0.35eV
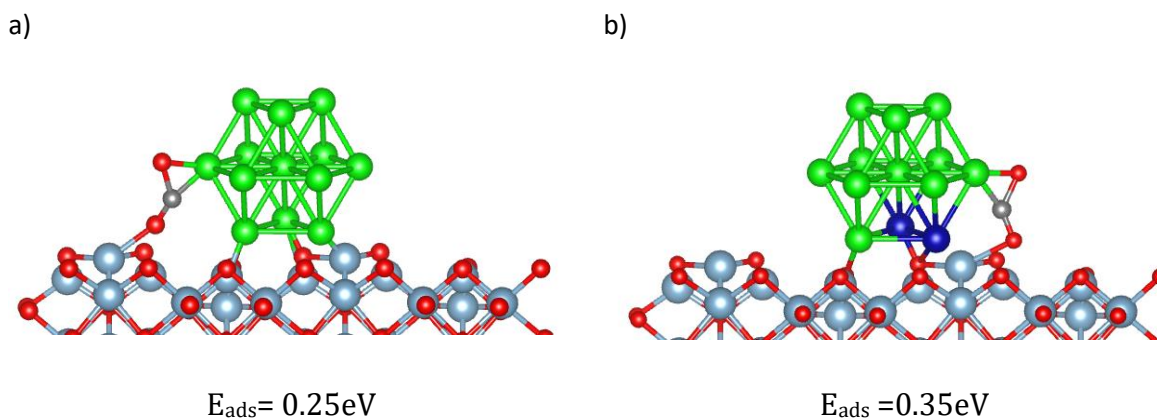
Figure 36. Most stable configuration of the adsorbed CO_2 on a) Ni_{13}/Al_2O_3 and b) Co_2Ni_{11}/Al_2O_3

IV.4.9. C adsorption

In the literature, it has been reported [63] that the main pathway of carbon deposition on the catalyst surface is the CH4 cracking reaction, in which the methane goes through a series of decomposition steps to finally form a deposited carbon on the catalyst surface. Moreover, the disproportionation of the carbon monoxide in the Boudouard reaction $2CO_{(g)} \leftrightarrow CO_{2\,(g)} + C_{(s)}$ can enhance the carbon formation, which leads to active site blockage and, consequently, to catalyst deactivation. Furthermore, two additional pathways have been proposed to describe the carbon deposition, i.e. surface coupling mechanism, and dissolving mechanism, as detailed in the reference [64]. According to the recent DFT calculations, the deposited carbon strongly depends on the reaction pathway of C-H bond oxidation and the energy barrier of CO decomposition [6]. To assess this important issue, we investigated the adsorption of the carbon atom over the modeled catalyst systems, and the most stable configurations are presented in Figure 37.

E_{ads}= -6.64 eV E_{ads}= -6.10 eV
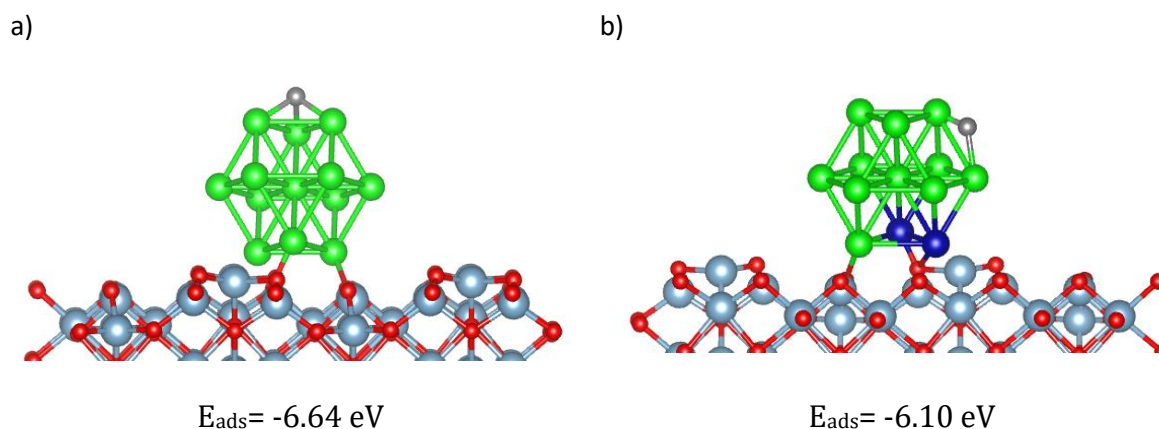
Figure 37. Most stable configuration of the adsorbed C on a) Ni_{13}/Al_2O_3 and b) Co_2Ni_{11}/Al_2O_3

IV.4.10. Comparison of modeled catalysts to each other and literature

The adsorption energy values obtained in this study were compared to those reported in the literature to gain insight into the performance of our catalysts.

In terms of methane adsorption, the results showed weak adsorption on our supported catalysts, indicating physisorption behavior, which is consistent with the findings of previous studies. Additionally, the adsorption energy values obtained on our supported catalysts were higher than those observed on the extended surface of Ni(111), indicating the role of the support in enhancing the gas-surface interaction.

The results obtained for CO_2 adsorption indicated that our catalysts had the highest adsorption values reported in the literature, highlighting their superior performance. Moreover, it is worth noting that the adsorption energy of CO_2 on Co_2Ni_{11}/Al_2O_3 was slightly higher than that of Ni_{13}/Al_2O_3, suggesting the beneficial effect of Co in enhancing CO_2 adsorption.

For C adsorption, it is evident that the interaction of C with our catalysts was lower than that reported in the literature, particularly in comparison to Ni/ZrO_2, Ni/MgO, and $Pt_{12}Ni$,

indicating the anti-coking behavior of our catalysts. Furthermore, the lower value of C

adsorption on Co_2Ni_{11}/Al_2O_3 compared to Ni_{13}/Al_2O_3 justifies the lower amount of carbon

detected by TGA in the experimental work for Co_2Ni_{11}/Al_2O_3 compared to Ni_{13}/Al_2O_3.

Table 11. Adsorption energies (eV) of the CH_4, CO_2, and C species over the modeled catalysts

Species	Ni_{13}/Al_2O_3	Co_2Ni_{11}/Al_2O_3	Ni(111) [79]	Ni/ZrO$_2$ [23]	Ni/αMoC (111) [80]	Ni/CaO [81]	Ni/MgO (100)[82]	Pt$_{12}$Ni [78]
CH$_4$	-0.31	-0.44	-0.02	-0.66	-0.39	-0.183	-0.02	-0.28
CO$_2$	-2.33	-2.43	-0.02	-1.29	-0.91	-1.810	-0.03	-0.60
C	-6.22	-6.10	-6.78	-9.21	-6.77	/	-8.14	-7.10
Metal	-5.57	-6.03						

Conclusion

Conclusion

The conversion of methane into syngas (CO, H_2) by reaction with carbon dioxide via dry reforming (DRM) has a great potential to address future increasing energy demand and reduce environmental changes. However, the main problem with this process is the rapid deactivation of the catalysts used due to metal sintering and the coke deposition on the surface of the catalysts. Recently, several strategies have been developed in this field to propose a new concept of low cost and high-performance catalysts that resilient to coke disposition and metal sintering under reaction conditions, including e.g., the use of bimetallic combination, the adoption of supports with acid-base surfaces, or enhancing strong metal-support interaction or mobility of oxygen. Nickel-based catalysts are one of the most widely used classes of catalysts for dry reforming process. Moreover, it is of vital importance to understand the basic mechanisms for DRM reactions such as CH_4 and CO_2 dissociation, water-gas shift reaction and other existed interactions in the process, including metal-metal and metal-support interactions, which will guide the design of excellent Ni-based catalysts. Otherwise, without a clear understanding of these interactions, proposed strategies to overcome the problem remain just a trial-and-error approach. Density functional theory (DFT), the most famous quantum mechanical method in chemistry and physics, has been frequently used in DRM process investigations. Nowadays, many scientists in this field believe that in addition to the experimental work on this process, there is also a need to complement them with state-of-the-art theoretical computations. Thus, DFT was used to complement information obtained from the achieved experimental works and to provide insights on the behavior of the process at the electronic and atomic levels to better understand the reaction mechanism and atomic interactions. The knowledge generated by DFT approaches can

provide useful data to go through the development and design of new high-performance catalysts.

This thesis summarizes the recent advances achieved in the analysis of the catalytic DRM process using DFT, and our contribution to improve the stability and selectivity of Ni-based catalysts by adding a small amount of Co. DFT has a great potential in providing details at the atomic scale about the adsorption mechanism of different species of the DRM process over several catalysts. Besides, it could also give some meaningful suggestions for the reduction and removal of carbon deposits and metal sintering in the experimental and industrial processes. Thus, some recommendations for future works can be identified, such as carrying out a theoretical study of metal-support interaction and oxygen vacancy, which would allow to choose the best couple metal/support with a high performance against metal sintering and carbon deposition. Simultaneously, it would be interesting to study the possible reactions mechanism over the chosen catalyst to predict the final product and avoid the coke formation, and conducting a thermodynamic and energetic study of different reactions to determine the most suitable and economic catalyst that provides the desired performances. In conclusion, the search for new economic and viable catalysts with high performances remains imperative to further develop the process at industrial and commercial scale and, in this sense, DFT can provide a significant contribution thanks to the proved great successes of recorded in catalysts development for the DRM process.

References

References

1. Akbari, E., S.M. Alavi, and M. Rezaei, Synthesis gas production over highly active and stable nanostructured Ni MgO Al 2 O 3 catalysts in dry reforming of methane: Effects of Ni contents. Fuel, 2017. 194: p. 171-179.

2. Niu, J., et al., Methane dry (CO_2) reforming to syngas (H_2/CO) in catalytic process: From experimental study and DFT calculations. International Journal of Hydrogen Energy, 2020. 45(55): p. 30267-30287.

3. Aziz, M.A.A., et al., A review of heterogeneous catalysts for syngas production via dry reforming. Journal of the Taiwan Institute of Chemical Engineers, 2019. 101: p. 139-158.

4. IEA, CO2 Emissions from Fuel Combustion: Overview. (2020): IEA, Paris https://www.iea.org/reports/co2-emissions-from-fuel-combustion-overview.

5. Aizebeokhai, A.P., Global warming and climate change: Realities, uncertainties and measures. International journal of physical sciences, 2009. 4(13): p. 868-879.

6. Rathod, V. and P.V. Bhale, Experimental Investigation on Biogas Reforming for Syngas Production over an Alumina based Nickel Catalyst. Energy Procedia, 2014. 54: p. 236-245.

7. Roser, H.R.a.M. CO_2 and Greenhouse Gas Emissions. 2020; Available from: https://ourworldindata.org/co2-and-other-greenhouse-gas-emissions.

8. Bian, Z., et al., A Review on Bimetallic Nickel-Based Catalysts for CO_2 Reforming of Methane. Chemphyschem, 2017. 18(22): p. 3117-3134.

9. Zeng, Y.X., et al., Low temperature reforming of biogas over K-, Mg- and Ce-promoted Ni/Al_2O_3 catalysts for the production of hydrogen rich syngas: Understanding the plasma-catalytic synergy. Applied Catalysis B: Environmental, 2018. 224: p. 469-478.

10. Charisiou, N.D., et al., Synthesis Gas Production via the Biogas Reforming Reaction Over Ni/MgO–Al2O3 and Ni/CaO–Al2O3 Catalysts. Waste and Biomass Valorization, 2016. 7(4): p. 725-736.

11. Iakovou, E., et al., Waste biomass-to-energy supply chain management: a critical synthesis. Waste Manag, 2010. 30(10): p. 1860-70.

12. Wang, X., et al., High-performance nano-structured Ni based catalysts for high-temperature CO2CH4 reforming—Greenhouse gases to syngas. Catalysis Today, 2020. 339: p. 344-351.

13. Muraza, O. and A. Galadima, A review on coke management during dry reforming of methane. International Journal of Energy Research, 2015. 39(9): p. 1196-1216.

14. Pakhare, D. and J. Spivey, A review of dry (CO2) reforming of methane over noble metal catalysts. Chem Soc Rev, 2014. 43(22): p. 7813-37.

15. Aramouni, N.A.K., et al., Catalyst design for dry reforming of methane: Analysis review. Renewable and Sustainable Energy Reviews, 2018. 82: p. 2570-2585.

16. Praserthdam, S., et al., Computational Study of the Evolution of Ni-Based Catalysts during the Dry Reforming of Methane. Energy & Fuels, 2020.

17. Schwengber, C.A., et al., Methane dry reforming using Ni/Al2O3 catalysts: Evaluation of the effects of temperature, space velocity and reaction time. Journal of Environmental Chemical Engineering, 2016. 4(3): p. 3688-3695.

18. Jang, W.-J., et al., A review on dry reforming of methane in aspect of catalytic properties. Catalysis Today, 2019. 324: p. 15-26.

19. Arora, S. and R. Prasad, An overview on dry reforming of methane: strategies to reduce carbonaceous deactivation of catalysts. RSC Advances, 2016. 6(110): p. 108668-108688.

20. Lavoie, J.M., Review on dry reforming of methane, a potentially more environmentally-friendly approach to the increasing natural gas exploitation. Front Chem, 2014. 2: p. 81.

21. Singh, S., et al., Boron-doped Ni/SBA-15 catalysts with enhanced coke resistance and catalytic performance for dry reforming of methane. Journal of the Energy Institute, 2020. 93(1): p. 31-42.

22. Sebai, I., et al., Preparation and characterization of 5%Ni/γ-Al2o3 catalysts by complexation with NH3 derivatives active in methane steam reforming. International Journal of Hydrogen Energy, 2019. 44(20): p. 9949-9958.

23. de Freitas Silva, T., et al., Ni/Al2O3catalysts: effects of the promoters Ce, La and Zr on the methane steam and oxidative reforming reactions. Catal. Sci. Technol., 2013. 3(3): p. 635-643.

24. Juan-Juan, J., M.C. Román-Martínez, and M.J. Illán-Gómez, Nickel catalyst activation in the carbon dioxide reforming of methane. Applied Catalysis A: General, 2009. 355(1-2): p. 27-32.

25. Wysocka, I., J. Hupka, and A. Rogala, Catalytic Activity of Nickel and Ruthenium–Nickel Catalysts Supported on SiO2, ZrO2, Al2O3, and MgAl2O4 in a Dry Reforming Process. Catalysts, 2019. 9(6): p. 540.

26. Papadopoulou, C., H. Matralis, and X. Verykios, Utilization of Biogas as a Renewable Carbon Source: Dry Reforming of Methane. 2012: p. 57-127.

27. Aghamohammadi, S., et al., Sequential impregnation vs. sol-gel synthesized Ni/Al 2 O 3 -CeO 2 nanocatalyst for dry reforming of methane: Effect of synthesis method and support promotion. Molecular Catalysis, 2017. 431: p. 39-48.

28. Ibrahim, A.A., et al., Dry Reforming of Methane Using Ce-modified Ni Supported on 8%PO4 + ZrO2 Catalysts. Catalysts, 2020. 10(2): p. 242.

29. Qin, Z., et al., Recent Advances in Heterogeneous Catalytic Hydrogenation of CO2 to Methane. 2017.

30. Kim, H.-M., et al., Effect of support materials and Ni loading on catalytic performance for carbon dioxide reforming of coke oven gas. International Journal of Hydrogen Energy, 2019. 44(16): p. 8233-8242.

31. Pan, C.-J., et al., Tuning/exploiting Strong Metal-Support Interaction (SMSI) in Heterogeneous Catalysis. Journal of the Taiwan Institute of Chemical Engineers, 2017. 74: p. 154-186.

32. Frontera, P., et al., Supported Catalysts for CO2 Methanation: A Review. Catalysts, 2017. 7(12): p. 59.

33. Therdthianwong, S., Synthesis gas production from dry reforming of methane over Ni/Al2O3 stabilized by ZrO2. International Journal of Hydrogen Energy, 2008. 33(3): p. 991-999.

34. Yentekakis, I.V., et al., Effect of support oxygen storage capacity on the catalytic performance of Rh nanoparticles for CO2 reforming of methane. Applied Catalysis B: Environmental, 2019. 243: p. 490-501.

35. Paksoy, A.I., B.S. Caglayan, and A.E. Aksoylu, A study on characterization and methane dry reforming performance of Co–Ce/ZrO 2 catalyst. Applied Catalysis B: Environmental, 2015. 168-169: p. 164-174.

36. García, V., et al., Effect of MgO addition on the basicity of Ni/ZrO2 and on its catalytic activity in carbon dioxide reforming of methane. Catalysis Communications, 2009. 11(4): p. 240-246.

37. Özdemir, H., M.A. Faruk Öksüzömer, and M. Ali Gürkaynak, Preparation and characterization of Ni based catalysts for the catalytic partial oxidation of methane: Effect of support basicity on H2/CO ratio and carbon deposition. International Journal of Hydrogen Energy, 2010. 35(22): p. 12147-12160.

38. Hou, Z., et al., Production of synthesis gas via methane reforming with CO22 on noble metals and small amount of noble-(Rh-) promoted Ni catalysts. International Journal of Hydrogen Energy, 2006. 31(5): p. 555-561.

39. Z. Xiea, Q.L., M. Liua, Z. Yanga, L. Zhanga, Micro-kinetic modeling study of dry reforming of methane over the Ni-based catalyst. Energy Conversion and Management 2017. 153: p. 526–537.

40. Shah, Y.T. and T.H. Gardner, Dry Reforming of Hydrocarbon Feedstocks. Catalysis Reviews, 2014. 56(4): p. 476-536.

41. P. Turlier, H.P., P. Moral, G. A. Martin, and J. A. Dalmon,, Influence of the nature of the support on the reducibility and catalytic properties of nickel: evidence for a new type of metal support interaction. Applied Catalysis 1985. 19(2): p. 287–300.

42. Gomes, R., et al., Dry Reforming of Methane over NiLa-Based Catalysts: Influence of Synthesis Method and Ba Addition on Catalytic Properties and Stability. Catalysts, 2019. 9(4): p. 313.

43. Al-Fatesh, A.S., et al., Effect of pre-treatment and calcination temperature on Al2O3-ZrO2 supported Ni-Co catalysts for dry reforming of methane. International Journal of Hydrogen Energy, 2019. 44(39): p. 21546-21558.

44. Abd Ghani, N.A., et al., Dry reforming of methane for syngas production over Ni–Co-supported Al2O3–MgO catalysts. Applied Petrochemical Research, 2018. 8(4): p. 263-270.

45. Bo, Z., et al., Plasma assisted dry methane reforming using gliding arc gas discharge: Effect of feed gases proportion. International Journal of Hydrogen Energy, 2008. 33(20): p. 5545-5553.

46. Song, Y., et al., Dry reforming of methane by stable Ni–Mo nanocatalysts on single-crystalline MgO. Science, 2020. 367(6479): p. 777-781.

47. Khoja, A.H., et al., Kinetic study of dry reforming of methane using hybrid DBD plasma reactor over La2O3 co-supported Ni/MgAl2O4 catalyst. International Journal of Hydrogen Energy, 2020. 45(22): p. 12256-12271.

48. Das, S., et al., Highly Dispersed Ni/Silica by Carbonization–Calcination of a Chelated Precursor for Coke-Free Dry Reforming of Methane. ACS Applied Energy Materials, 2020. 3(8): p. 7719-7735.

49. Leba, A. and R. Yıldırım, Determining most effective structural form of nickel-cobalt catalysts for dry reforming of methane. International Journal of Hydrogen Energy, 2020. 45(7): p. 4268-4283.

50. Zhang, F., et al., Effects of Zr doping into ceria for the dry reforming of methane over Ni/CeZrO2 catalysts: in situ studies with XRD, XAFS, and AP-XPS. ACS Catalysis, 2020. 10(5): p. 3274-3284.

51. Tu, P.H., et al., structured catalyst containing CeO2–Ni flowers for dry reforming of methane. International Journal of Hydrogen Energy, 2020. 45(36): p. 18363-18375.

52. Song, Z., et al., Improved effect of fe on the stable NiFe/Al2o3 catalyst in low-temperature dry reforming of methane. Industrial & Engineering Chemistry Research, 2020. 59(39): p. 17250-17258.

53. Turap, Y., et al., Co–Ni alloy supported on CeO2 as a bimetallic catalyst for dry reforming of methane. International Journal of Hydrogen Energy, 2020. 45(11): p. 6538-6548.

54. Chong, C.C., et al., Dry reforming of methane over Ni/dendritic fibrous SBA-15 (Ni/DFSBA-15): optimization, mechanism, and regeneration studies. International Journal of Hydrogen Energy, 2020. 45(15): p. 8507-8525.

55. Shen, D., et al., Effects of alumina morphology on dry reforming of methane over Ni/Al 2 O 3 catalysts. Catalysis Science & Technology, 2020. 10(2): p. 510-516.

56. Li, B., et al., Impact of pore structure on hydroxyapatite supported nickel catalysts (Ni/HAP) for dry reforming of methane. Fuel Processing Technology, 2020. 202: p. 106359.

57. Hambali, H.U., et al., Enhanced dry reforming of methane over mesostructured fibrous Ni/MFI zeolite: Influence of preparation methods. Journal of the Energy Institute, 2020. 93(4): p. 1535-1543.

58. Wang, L., et al., Encapsulated Ni@ La2O3/SiO2 catalyst with a one-pot method for the dry reforming of methane. Catalysts, 2020. 10(1): p. 38.

59. Fan, C., et al., Density functional theory-assisted microkinetic analysis of methane dry reforming on Ni catalyst. Industrial & Engineering Chemistry Research, 2015. 54(22): p. 5901-5913.

60. Wittich, K., et al., Catalytic Dry Reforming of Methane: Insights from Model Systems. ChemCatChem, 2020.

61. Vogiatzis, K.D., et al., Computational Approach to Molecular Catalysis by 3d Transition Metals: Challenges and Opportunities. Chem Rev, 2019. 119(4): p. 2453-2523.

62. Grindy, S., et al., Approaching chemical accuracy with density functional calculations: Diatomic energy corrections. Physical Review B, 2013. 87(7).

63. Blaylock, D.W., Y.-A. Zhu, and W.H. Green, Computational Investigation of the Thermochemistry and Kinetics of Steam Methane Reforming Over a Multi-Faceted Nickel Catalyst. Topics in Catalysis, 2011. 54(13-15): p. 828-844.

64. Durand, D.J. and N. Fey, Computational Ligand Descriptors for Catalyst Design. Chem Rev, 2019. 119(11): p. 6561-6594.

65. Hohenberg, P. and W. Kohn, Inhomogeneous Electron Gas. Physical Review, 1964. 136(3B): p. B864-B871.

66. Kohn, W. and L.J. Sham, Self-Consistent Equations Including Exchange and Correlation Effects. Physical Review, 1965. 140(4A): p. A1133-A1138.

67. Cohen, A.J., P. Mori-Sánchez, and W. Yang, Challenges for Density Functional Theory. Chemical Reviews, 2011. 112(1): p. 289-320.

68. L. Goerigk, A.H., C. Bauer, S. Ehrlich, A. Najibi, and S. Grimme, A look at the density functional theory zoo with the advanced GMTKN55 database for general main group thermochemistry, kinetics and noncovalent interactions. Physical Chemistry Chemical Physics, 2017. 19: p. 32184–32215.

69. M. Schreiber, M.R.S.-J., S. P. A. Sauer, and W. Thiel, Benchmarks for electronically excited states: CASPT2, CC2, CCSD, and CC3. The Journal of Chemical Physics, 2008. 128: p. 134110.

70. D. E. Taylor, J.G.Á., G. Galli, C. Zhang, F. Gygi, K. Hirao, J. W. Song, K. Rahul, O. Anatole von Lilienfeld, R. Podeszwa, I. W. Bulik, T. M. Henderson, G. E. Scuseria, J. Toulouse, R. Peverati, D. G. Truhlar, and K. Szalewicz, Blind test of density-functional-based methods on intermolecular interaction energies. The Journal of Chemical Physics, 2016. 145: p. 124105.

71. Head-Gordon, N.M.a.M., Thirty years of density functional theory in computational chemistry: an overview and extensive assessment of 200 density functionals. Molecular Physics, 2017. 115: p. 2315–2372.

72. Dirac, P.A.M., Note on Exchange Phenomena in the Thomas Atom. Mathematical Proceedings of the Cambridge Philosophical Society, 2008. 26(3): p. 376-385.

73. Koch, W., M.C. Holthausen, A Chemist's Guide to Density Functional Theory, ed. n. edition. 2001: Wiley VCH Verlag GmbH.

74. Wang, J.P.P.a.Y., Erratum: Accurate and simple analytic representation of the electron-gas correlation energy. Phys. Rev. B, 1992. 45: p. 13244

75. S. H. Vosko, L.W., and M. Nusair, Accurate spin-dependent electron liquid correlation energies for local spin density calculations: a critical analysis. Canadian Journal of Physics, 1980. 58: p. 1200–1211.

76. Yue, J.P.P.a.W., Accurate and simple density functional for the electronic exchange energy: Generalized gradient approximation. Physical Review B, 1986. 33: p. 8800–8802.

77. Perdew, J.P., Generalized gradient approximations for exchange and correlation: A look backward and forward. Physica B: Condensed Matter, 1991. 172: p. 1-6.

78. Becke, A.D., Density-functional exchange-energy approximation with correct asymptotic behavior. Physical Review A, 1988. 38: p. 3098–3100.

79. Madsen, G.K.H., Functional form of the generalized gradient approximation for exchange: ThePBEαfunctional. Physical Review B, 2007. 75(19).

80. Pribram-Jones, A., D.A. Gross, and K. Burke, DFT: A Theory Full of Holes? Annu Rev Phys Chem, 2015. 66: p. 283-304.

81. CORDERO, J.A.A.A.N.A., Exchange and Correlation in Density Functional Theory. International Journal of Quantum Chemistry: Quantum Chemistry Symposium, 1995. 29: p. 49-59.

82. Liu, J., et al., DFT study on electronic structures and optical absorption properties of C, S cation- doped SrTiO3. Open Physics, 2009. 7(4).

83. Benidris, A., Zaoui, A., Belhadj, M. et al, Structure and Magnetic Properties of RESn3 Compounds: GGA + U Calculations. J Supercond Nov Magn, 2015. 28: p. 2215–2222.

84. Noura, L.A.a.H., Perovskite oxides MRuO 3 (M = Sr, Ca and Ba): Structural distortion, electronic and magnetic properties with GGA and GGA-modified Becke–Johnson approaches. Results in Physics, 2015. 5: p. 38–52.

85. Yeganeh, D.V.F.a.M., GGA and Meta-GGA study of electronic, optical and thermoelectric properties of fluorinated borophene. Superlattices and Microstructures, 2020. 143: p. 106553.

86. M. Zhang, H.G., J. Lv, and H. Wu, Electronic and magnetic properties of 5d transition metal substitution doping monolayer antimonene: within GGA and GGA + U framework. Applied Surface Science, 2020. 508: p. 145197.

87. Perdew, J.P.B., K.; Ernzerhof, M., Generalized Gradient Approximation Made Simple. Phys. Rev. Lett, 1996. 77: p. 3865-3868.

88. Neil Qiang Su, I.Y.Z., Jianming Wu, Xin Xu, Calculations of ionization energies and electron affinities for atoms and molecules: A comparative study with different methods. Frontiers of Chemistry in China, 2011. 6: p. 269-279.

89. S. Kurth, J.P.P., and P. Blaha, Molecular and solid-state tests of density functional approximations: LSD, GGAs, and meta-GGAs. Int. J. Quantum Chem, 1999. 75: p. 889.909.

90. Campo, J.M.d., B88 exchange functional recovering the local spin density linear response. Theoretical Chemistry Accounts, 2016. 135(7).

91. Perdew, J.P.C., J. A.; Vosko, S. H.; Jackson, K. A.; Pederson, M. R.; Singh, D. J.; Fiolhais, C., Atoms, molecules, solids, and surfaces: Applications of the generalized gradient approximation for exchange and correlation. Phys. Rev. B, 1992. 46: p. 6671-6687.

92. Becke, A.D., Density-functional exchange-energy approximation with correct asymptotic behavior. Phys. Rev. A, 1988. 38: p. 3098-3100.

93. Becke, A.D., A new mixing of Hartree–Fock and local density-functional theories. The Journal of Chemical Physics, 1993. 98: p. 1372–1377.

94. P. J. Stephens, F.J.D., C. F. Chabalowski, and M. J. Frisch, Ab Initio Calculation of Vibrational Absorption and Circular Dichroism Spectra Using Density Functional Force Fields. Journal of Physical Chemistry 1994. 98: p. 11623-11627.

95. Jorgensen, J.T.-R.a.W.L., Performance of B3LYP Density Functional Methods for a Large Set of Organic Molecules. J. Chem. Theory Comput, 2008. 4: p. 297-306.

96. Adamo, C.V.B., Toward reliable density functional methods without adjustable parameters: The PBE0 model. The Journal of Chemical Physics, 1999. 110: p. 6158–6170.

97. Ernzerhof, J.H.G.E.S.M., Hybrid functionals based on a screened Coulomb potential. J. Chem. Phys., 2003. 18: p. 8207.

98. Zhao, Y.D.G.T., The M06 suite of density functionals for main group thermochemistry, thermochemical kinetics, noncovalent interactions, excited states, and transition elements: two new functionals and systematic testing of four M06-class functionals and 12 other functionals. Theor. Chem. Account, 2008. 120: p. 215–241.

99. Ray, K., et al., Developing descriptors for CO2 methanation and CO2 reforming of CH4 over Al2O3 supported Ni and low-cost Ni based alloy catalysts. Phys Chem Chem Phys, 2018. 20(23): p. 15939-15950.

100. Ray, K., Aditya Shankar Deo, Goutam, Activity and stability descriptors of Ni based alloy catalysts for dry reforming of methane: A density functional theory study. International Journal of Quantum Chemistry, 2020.

101. E. Pérez, A. and R. Ribadeneira, Modeling with DFT and Chemical Descriptors Approach for the Development of Catalytic Alloys for PEMFCs. 2019.

102. Porosoff, M.D., W. Yu, and J.G. Chen, Challenges and opportunities in correlating bimetallic model surfaces and supported catalysts. Journal of Catalysis, 2013. 308: p. 2-10.

103. Grabow, L.C., et al., Descriptor-based analysis applied to HCN synthesis from NH3 and CH4. Angew Chem Int Ed Engl, 2011. 50(20): p. 4601-5.

104. Norskov, J.K., et al., Towards the computational design of solid catalysts. Nat Chem, 2009. 1(1): p. 37-46.

105. Ghosh, S., N. Mammen, and S. Narasimhan, Support work function as a descriptor and predictor for the charge and morphology of deposited Au nanoparticles. J Chem Phys, 2020. 152(14): p. 144704.

106. Ding, Y., et al., Achieving rational design of alloy catalysts using a descriptor based on a quantitative structure-energy equation. Chem Commun (Camb), 2020. 56(21): p. 3214-3217.

107. G. Palm, Warren McCulloch and Walter Pitts: A Logical Calculus of the Ideas Immanent in Nervous Activity. Brain Theory, 1986: p. 229–230.

108. Ouyang, R., et al., SISSO: A compressed-sensing method for identifying the best low-dimensional descriptor in an immensity of offered candidates. Physical Review Materials, 2018. 2(8): p. 083802.

109. Rothenberg, E.B.a.G., In Silico Design in Homogeneous Catalysis Using Descriptor Modelling. Int. J. Mol. Sci., 2006. 7: p. 375-404.

110. Norskov, J.K., et al., The nature of the active site in heterogeneous metal catalysis. Chem Soc Rev, 2008. 37(10): p. 2163-71.

111. Jacobs, R., et al., Assessing correlations of perovskite catalytic performance with electronic structure descriptors. Chemistry of Materials, 2019. 31(3): p. 785-797.

112. Lee, Y.-L., et al., Prediction of solid oxide fuel cell cathode activity with first-principles descriptors. Energy & Environmental Science, 2011. 4(10): p. 3966-3970.

113. Rossmeisl, J., A. Logadottir, and J.K. Nørskov, Electrolysis of water on (oxidized) metal surfaces. Chemical Physics, 2005. 319(1-3): p. 178-184.

114. Fukui, K., T. Yonezawa, and H. Shingu, A Molecular Orbital Theory of Reactivity in Aromatic Hydrocarbons. The Journal of Chemical Physics, 1952. 20(4): p. 722-725.

115. Schmuck, C., Modern Physical Organic Chemistry. Von Eric V. Anslyn und Dennis A. Dougherty. Angewandte Chemie, 2006. 118(7): p. 1036-1037.

116. Getsoian, A.B., Z. Zhai, and A.T. Bell, Band-gap energy as a descriptor of catalytic activity for propene oxidation over mixed metal oxide catalysts. J Am Chem Soc, 2014. 136(39): p. 13684-97.

117. Polanyi, M.G.E.a.M., nertia and driving force of chemical reactions. Transactions of the Faraday Society, 1938. 34: p. 11.

118. Bronsted, J.N., Acid and Basic Catalysis. Chemical Reviews, 1928. 5: p. 231–338.

119. Andersen, M., et al., Beyond Scaling Relations for the Description of Catalytic Materials. ACS Catalysis, 2019. 9(4): p. 2752-2759.

120. Nguyen, N.L., S. de Gironcoli, and S. Piccinin, Ag-Cu catalysts for ethylene epoxidation: selectivity and activity descriptors. J Chem Phys, 2013. 138(18): p. 184707.

121. Wang, Y., et al., Adsorption-energy-based activity descriptors for electrocatalysts in energy storage applications. National Science Review, 2018. 5(3): p. 327-341.

122. Zuo, Z., et al., Dry Reforming of Methane on Single-Site Ni/MgO Catalysts: Importance of Site Confinement. ACS Catalysis, 2018. 8(10): p. 9821-9835.

123. Wang, B., et al., Propagating DFT Uncertainty to Mechanism Determination, Degree of Rate Control, and Coverage Analysis: The Kinetics of Dry Reforming of Methane. The Journal of Physical Chemistry C, 2019. 123(50): p. 30389-30397.

124. Z. Zuo, S.L., Z. Wang, C. Liu, W. Huang, J. Huang, and P. Liu, Dry Reforming of Methane on Single Site Ni/MgO Catalysts: Importance of Site Confinement. ACS Catalysis, 2018. 8: p. 9821–9835.

125. Ras, E.J., et al., Predicting adsorption on metals: simple yet effective descriptors for surface catalysis. Phys Chem Chem Phys, 2013. 15(12): p. 4436-43.

126. Tao, H., et al., Descriptor of catalytic activity of metal sulfides for oxygen reduction reaction: a potential indicator for mineral flotation. Journal of Materials Chemistry A, 2018. 6(20): p. 9650-9656.

127. Zhuang, H., A.J. Tkalych, and E.A. Carter, Surface Energy as a Descriptor of Catalytic Activity. The Journal of Physical Chemistry C, 2016. 120(41): p. 23698-23706.

128. Zhao, Z.-J., et al., Theory-guided design of catalytic materials using scaling relationships and reactivity descriptors. Nature Reviews Materials, 2019. 4(12): p. 792-804.

129. Nguyen, N.L., S. de Gironcoli, and S. Piccinin, Ag-Cu catalysts for ethylene epoxidation: Selectivity and activity descriptors. The Journal of chemical physics, 2013. 138(18): p. 184707.

130. Sinthika, S., U.V. Waghmare, and R. Thapa, Structural and Electronic Descriptors of Catalytic Activity of Graphene-Based Materials: First-Principles Theoretical Analysis. Small, 2018. 14(10).

131. Nørskov JK, R.J., Logadottir A, Lindqvist L, Lyngby D, Jo H, Origin of the overpotential for oxygen reduction at a fuel-cell cathode. The Journal of Physical Chemistry B, 2004. 108: p. 17886-17892.

132. Bligaard, T., et al., The Brønsted–Evans–Polanyi relation and the volcano curve in heterogeneous catalysis. Journal of Catalysis, 2004. 224(1): p. 206-217.

133. Chen, L., et al., Catalytic Hydrogen Production from Methane: A Review on Recent Progress and Prospect. Catalysts, 2020. 10(8): p. 858.

134. Polo-Garzon, F., M. He, and D.A. Bruce, Ab initio derived reaction mechanism for the dry reforming of methane on Rh doped pyrochlore catalysts. Journal of Catalysis, 2016. 333: p. 59-70.

135. Luyben, W.L., Design and Control of the Dry Methane Reforming Process. Industrial & Engineering Chemistry Research, 2014. 53(37): p. 14423-14439.

136. Abbasi, S., et al., Syngas production plus reducing carbon dioxide emission using dry reforming of methane: utilizing low-cost Ni-based catalysts. Oil &

Gas Science and Technology – Revue d'IFP Energies nouvelles, 2020. 75: p. 22.

137. Omran, A., et al., Mechanistic insights for dry reforming of methane on Cu/Ni bimetallic catalysts: DFT-assisted microkinetic analysis for coke resistance. Catalysts, 2020. 10(9): p. 1043.

138. Foucaud, Y., et al., A review of atomistic simulation methods for surface physical-chemistry phenomena applied to froth flotation. Minerals Engineering, 2019. 143: p. 106020.

139. Domingo, L.R., M. Rios-Gutierrez, and P. Perez, Applications of the Conceptual Density Functional Theory Indices to Organic Chemistry Reactivity. Molecules, 2016. 21(6).

140. Kryachko, E.S., Density Functional Theory and Molecular Interactions: Dispersion Interactions," Applications of Density Functional Theory to Biological and Bioinorganic Chemistry. 2012: Springer-Verlag Berlin Heidelberg. XII, 236.

141. Hine, D.J.C.a.N.D.M., Applications of large-scale density functional theory in biology. J. Phys.: Condens. Matter, 2016. 26: p. 31.

142. Mazurek, A.H., L. Szeleszczuk, and D.M. Pisklak, Periodic DFT Calculations-Review of Applications in the Pharmaceutical Sciences. Pharmaceutics, 2020. 12(5).

143. M. Hagar, H.A.A., G. Aljohani, O. A. Alhaddad, Investigation of Some Antiviral N-Heterocycles as COVID 19 Drug: Molecular Docking and DFT Calculations. Int. J. Mol. Sci, 2020. 21: p. 3922.

144. M.te Vrugt, J.B., and R. Wittkowski, Effects of social distancing and isolation on epidemic spreading: a dynamical density functional theory model. Nature Communications, 2020. 11.

145. Mishra, S.S., et al., Computational investigation of potential inhibitors of novel coronavirus 2019 through structure-based virtual screening, molecular dynamics and density functional theory studies. J Biomol Struct Dyn, 2020: p. 1-13.

146. Even, J., et al., Density Functional Theory Simulations of Semiconductors for Photovoltaic Applications: Hybrid Organic-Inorganic Perovskites and III/V Heterostructures. International Journal of Photoenergy, 2014. 2014: p. 649408.

147. P. J. Hasnip , K.R., M.J. Probert, J. R. Yates,S. J. Clark and C. J. Pickard, Density functional theory in the solid state. Phil. Trans. R. Soc. A, 2014. 372: p. 20130270.

148. Wu, J., Density functional theory for chemical engineering: From capillarity to soft materials. AIChE Journal, 2006. 52(3): p. 1169-1193.

149. Deushi, F., A. Ishikawa, and H. Nakai, Density Functional Theory Analysis of Elementary Reactions in NOx Reduction on Rh Surfaces and Rh Clusters. The Journal of Physical Chemistry C, 2017. 121(28): p. 15272-15281.

150. Voĉadlo, J.P.B.a.L., Applications of Density Functional Theory in the Geosciences. MRS Bulletin, 2006. 31: p. 675–680.

151. J. Yun, Q.W., C. Zhu, G. Yang, Application of Density Functional Theory in Soil Science. Density Functional Calculations - Recent Progresses of Theory and Application. 2018.

152. Nørskov, J.K., et al., Density functional theory in surface chemistry and catalysis. Proceedings of the National Academy of Sciences, 2011. 108(3): p. 937-943.

153. Zhu, Y.-A., et al., DFT studies of dry reforming of methane on Ni catalyst. Catalysis Today, 2009. 148(3-4): p. 260-267.

154. Nie, X., et al., DFT insight into the support effect on the adsorption and activation of key species over Co catalysts for CO2 methanation. Journal of CO2 Utilization, 2018. 24: p. 99-111.

155. Xu, L.-l., et al., DFT study on dry reforming of methane over Ni2Fe overlayer of Ni(1 1 1) surface. Applied Surface Science, 2018. 443: p. 515-524.

156. Li, J., E. Croiset, and L. Ricardez-Sandoval, Methane dissociation on Ni (100), Ni (111), and Ni (553): A comparative density functional theory study. Journal of Molecular Catalysis A: Chemical, 2012. 365: p. 103-114.

157. Niu, J., et al., Dry (CO 2) reforming of methane over Pt catalysts studied by DFT and kinetic modeling. Applied Surface Science, 2016. 376: p. 79-90.

158. Ren, J., et al., Insights into the mechanisms of CO2 methanation on Ni(111) surfaces by density functional theory. Applied Surface Science, 2015. 351: p. 504-516.

159. Zhang, M., et al., Effect of Ni(111) surface alloying by Pt on partial oxidation of methane to syngas: A DFT study. Surface Science, 2014. 630: p. 236-243.

160. Zhang, Z.-w., J.-c. Li, and Q. Jiang, Density functional theory calculations of the metal-doped carbon nanostructures as hydrogen storage systems under electric fields: A review. Frontiers of Physics, 2011. 6(2): p. 162-176.

161. Foppa, L., et al., Intrinsic reactivity of Ni, Pd and Pt surfaces in dry reforming and competitive reactions: Insights from first principles calculations and microkinetic modeling simulations. Journal of Catalysis, 2016. 343: p. 196-207.

162. Niu, J., et al., New mechanism insights into methane steam reforming on Pt/Ni from DFT and experimental kinetic study. Fuel, 2020. 266: p. 117143.

163. Pakhare, D., et al., Kinetic and mechanistic study of dry (CO2) reforming of methane over Rh-substituted La2Zr2O7 pyrochlores. Journal of catalysis, 2014. 316: p. 78-92.

164. Kathiraser, Y., et al., Inverse NiAl2O4 on LaAlO3–Al2O3: unique catalytic structure for stable CO2 reforming of methane. The Journal of Physical Chemistry C, 2013. 117(16): p. 8120-8130.

165. Robert W. Stevens, J.a.S.S.C.C., In Situ IR Study of Transient CO2 Reforming of CH4 over Rh/Al2O3. J. Phys. Chem., 2004. 108: p. 696-703.

166. Li, J., E. Croiset, and L. Ricardez-Sandoval, Effect of Metal–Support Interface During CH4 and H2 Dissociation on Ni/γ-Al2O3: A Density Functional Theory Study. The Journal of Physical Chemistry C, 2013. 117(33): p. 16907-16920.

167. Niu, J., et al., Effect of Pt addition on resistance to carbon formation of Ni catalysts in methane dehydrogenation over Ni-Pt bimetallic surfaces: A density functional theory study. Molecular Catalysis, 2017. 434: p. 206-218.

168. Guharoy, U., et al., Understanding the role of Ni-Sn interaction to design highly effective CO2 conversion catalysts for dry reforming of methane. Journal of CO2 Utilization, 2018. 27: p. 1-10.

169. Jiang, S., et al., Insight into the reaction mechanism of CO 2 activation for CH 4 reforming over NiO-MgO: A combination of DRIFTS and DFT study. Applied Surface Science, 2017. 416: p. 59-68.

170. Das, S., et al., Facile nitridation of NiO/Al2O3: an efficient approach to design an extraordinarily stable catalyst for dry reforming of methane. ACS Applied Energy Materials, 2018. 1(9): p. 4414-4419.

171. Dou, J., et al., Sandwiched SiO2@Ni@ZrO2 as a coke resistant nanocatalyst for dry reforming of methane. Applied Catalysis B: Environmental, 2019. 254: p. 612-623.

172. Ou, Z., et al., A comprehensive DFT study of CO2 catalytic conversion by H2 over Pt-doped Ni catalysts. International Journal of Hydrogen Energy, 2019. 44(2): p. 819-834.

173. Zou, X.-Y., et al., DFT and KMC study the strong metal–support interaction of DRM reaction over Ni based catalysts. Chinese Journal of Chemical Engineering, 2020.

174. Guo, Y., J. Feng, and W. Li, Effect of the Ni size on CH 4 /CO 2 reforming over Ni/MgO catalyst: A DFT study. Chinese Journal of Chemical Engineering, 2017. 25(10): p. 1442-1448.

175. Chen Tao , F.L., Luo Wei , Meng Yue , Xue Jilong , Xia Shengjie , Ni Zheming, , Theoretical Study of Dry Reforming of Methane Catalyzed by Bimetallic Alloy Cluster M12Ni(M=Pt, Sn, Cu) Chemical journal of chinese universities, 2019. 40: p. 2135-2142.

176. Guharoy, U., et al., Theoretical insights of Ni2P (0001) surface toward its potential applicability in CO2 conversion via dry reforming of methane. ACS Catalysis, 2019. 9(4): p. 3487-3497.

177. Wang, Z., et al., Activity and coke formation of nickel and nickel carbide in dry reforming: A deactivation scheme from density functional theory. Journal of Catalysis, 2014. 311: p. 469-480.

178. Foppa, L., et al., Contrasting the Role of Ni/Al2O3 Interfaces in Water-Gas Shift and Dry Reforming of Methane. J Am Chem Soc, 2017. 139(47): p. 17128-17139.

179. Zhang, R., et al., Insights into the effect of surface hydroxyls on CO2 hydrogenation over Pd/γ-Al2O3 catalyst: A computational study. Applied Catalysis B: Environmental, 2012. 126: p. 108-120.

180. Nugraha, et al., DFT study of the formate formation on Ni(111) surface doped by transition metals [Ni(111)-M; M=Cu, Pd, Pt, Rh]. Journal of Physics: Conference Series, 2016. 739: p. 012082.

181. Kratzer, P., B. Hammer, and J.K. No/rskov, A theoretical study of CH4 dissociation on pure and gold-alloyed Ni(111) surfaces. The Journal of Chemical Physics, 1996. 105(13): p. 5595-5604.

182. Cui, X., et al., Room-temperature electrochemical water-gas shift reaction for high purity hydrogen production. Nat Commun, 2019. 10(1): p. 86.

183. Becke, A.D., Density-functional thermochemistry. III. The role of exact exchange. The Journal of Chemical Physics, 1993. 98(7): p. 5648-5652.

184. C. V. Ovesen, B.S.C., B. S. Hammershøi, G. Steffensen,T. Askgaard, I. Chorkendorff, J. K. Nørskov,P. B. Rasmussen,P. Stoltze, and P. Taylor, A Microkinetic Analysis of the Water–Gas Shift Reaction under Industrial Conditions. JOURNAL OF CATALYSIS, 1996. 158: p. 170–180.

185. Ashok, J., M.H. Wai, and S. Kawi, Nickel-based Catalysts for High-temperature Water Gas Shift Reaction-Methane Suppression. ChemCatChem, 2018. 10(18): p. 3927-3942.

186. Catapan, R.C., et al., DFT Study of the Water–Gas Shift Reaction and Coke Formation on Ni(111) and Ni(211) Surfaces. The Journal of Physical Chemistry C, 2012. 116(38): p. 20281-20291.

187. Mohsenzadeh, A., T. Richards, and K. Bolton, DFT study of the water gas shift reaction on Ni(111), Ni(100) and Ni(110) surfaces. Surface Science, 2016. 644: p. 53-63.

188. Fajín, J.L.C.D.S.C., M. Natália, Probing the efficiency of platinum nanotubes for the H2 production by water gas shift reaction: A DFT study. Applied Catalysis B: Environmental, 2020. 263: p. 118301.

189. Nakhaei Pour, A. and S.F. Tayyari, Water-gas-shift reaction over nickel catalysts: DFT studies and kinetic modeling. Structural Chemistry, 2019. 30(5): p. 1843-1852.

190. Amit A. Gokhale, J.A.D., and Manos Mavrikakis, On the Mechanism of Low-Temperature Water Gas Shift Reaction on Copper. J. AM. CHEM. SOC, 2008. 130: p. 1402-1414.

191. Liu, P., et al., Water–gas-shift reaction on a Ni2P(001) catalyst: Formation of oxy-phosphides and highly active reaction sites. Journal of Catalysis, 2009. 262(2): p. 294-303.

192. Zhang, M., et al., A theoretical study of the reverse water-gas shift reaction on Ni(111) and Ni(311) surfaces. The Canadian Journal of Chemical Engineering, 2019. 98(3): p. 740-748.

193. Das, S., et al., A study of the synergy between support surface properties and catalyst deactivation for CO_2 reforming over supported Ni nanoparticles. Applied Catalysis A: General, 2017. 545: p. 113-126.

194. Lalik, E., et al., Humidity induced deactivation of Al2O3 and SiO2 supported Pd, Pt, Pd-Pt catalysts in H_2+O_2 recombination reaction: The catalytic, microcalorimetric and DFT studies. Applied Catalysis A: General, 2015. 501: p. 27-40.

195. Akri, M., et al., Atomically dispersed nickel as coke-resistant active sites for methane dry reforming. Nat Commun, 2019. 10(1): p. 5181.

196. K. Nagaoka, M.O.a.K.-i.A., Titani supported rethenium as a coking-resistant catalyst for hight pressure dry reforming of methane. Catal. Commun., 2001. 2: p. 255–260.

197. McKenzie P. Kohn a, M.J.C., Robert J. Farrauto, Auto-thermal and dry reforming of landfill gas over a Rh/gAl2O3 monolith catalyst. Applied Catalysis B: Environmental, 2010. 94: p. 125–133.

198. Chen, S., J. Zaffran, and B. Yang, Dry reforming of methane over the cobalt catalyst: Theoretical insights into the reaction kinetics and mechanism for catalyst deactivation. Applied Catalysis B: Environmental, 2020. 270: p. 118859.

199. Tessonnier, J.P. and D.S. Su, Recent progress on the growth mechanism of carbon nanotubes: a review. ChemSusChem, 2011. 4(7): p. 824-47.

200. Daza, C.E., et al., High stability of Ce-promoted Ni/Mg–Al catalysts derived from hydrotalcites in dry reforming of methane. Fuel, 2010. 89(3): p. 592-603.

201.   Gardner, T.H., et al., CH4–CO₂ reforming over Ni-substituted barium hexaaluminate catalysts. Applied Catalysis A: General, 2013. 455: p. 129-136.

202.   Chein, R.-Y. and W.-Y. Fung, Syngas production via dry reforming of methane over CeO2 modified Ni/Al2O3 catalysts. International Journal of Hydrogen Energy, 2019. 44(28): p. 14303-14315.

203.   Fouskas, A., et al., Boron-modified Ni/Al2O3 catalysts for reduced carbon deposition during dry reforming of methane. Applied Catalysis A: General, 2014. 474: p. 125-134.

204.   Arkatova, L.A., The deposition of coke during carbon dioxide reforming of methane over

intermetallides. Catalysis Today, 2010. 157: p. 170–176.

205.   Stacchiola, S.D.S.J.A.R.D., Electronic Metal–Support Interactions and the Production of Hydrogen Through the Water-Gas Shift Reaction and Ethanol Steam Reforming: Fundamental Studies with Well-Defined Model Catalysts. Top Catal, 2013. 56: p. 1488–1498.

206.   Yang, R., et al., Promotional effect of La2O3 and CeO2 on Ni/γ-Al2O3 catalysts for CO2 reforming of CH4. Applied Catalysis A: General, 2010. 385(1-2): p. 92-100.

207.   Z. Wang, X.-M.C., J. Zhu, and P. Hu, Activity and coke formation of nickel and nickel carbide in dry reforming: A deactivation scheme from density functional theory. Journal of Catalysis, 2014. 311: p. 469–480.

208.   D. Ray, S.G., and A. K. Tiwari, Controlling Heterogeneous Catalysis of Water Dissociation Using Cu–Ni Bimetallic Alloy Surfaces: A Quantum Dynamics Study. The Journal of Physical Chemistry A, 2018. 122: p. 5698–5709.

209.   L. Xu, H.W., X. Jin, Q. Bing, and J. Liu, DFT study on dry reforming of methane over Ni2Fe overlayer of Ni(1 1 1) surface. Applied Surface Science, 2018. 443: p. 515–524.

210.   Liu, H.Y.Z., R.G.; Yan, R.X.; Li, J.R.; Wang, B.J.; Xie, K.C, Insight into CH4 dissociation on NiCu catalyst: A first-principles study. Appl. Surf. Sci., 2012. 258: p. 8177–8184.

211.   G. Kresse, J.F., Efficiency of ab-initio total energy calculations for metals and semiconductors using a plane-wave basis set. Comput. Mater. Sci., 1996. 6: p. 15–50.

212.   Li, H., et al., Oxygen Vacancy Structure Associated Photocatalytic Water Oxidation of BiOCl. ACS Catalysis, 2016. 6(12): p. 8276-8285.

213.   Wang, F., et al., Catalytic behavior of supported Ru nanoparticles on the {1 0 0}, {1 1 0}, and {1 1 1} facet of CeO2. Journal of Catalysis, 2015. 329: p. 177-186.

214.   Boaro, M., S. Colussi, and A. Trovarelli, Ceria-Based Materials in Hydrogenation and Reforming Reactions for CO2 Valorization. Front Chem, 2019. 7: p. 28.

215.   Derk, A.R., et al., Methane Oxidation by Lanthanum Oxide Doped with Cu, Zn, Mg, Fe, Nb, Ti, Zr, or Ta: The Connection Between the Activation Energy and the Energy of Oxygen-Vacancy Formation. Catalysis Letters, 2013. 143(5): p. 406-410.

216.   Krcha, M.D., A.D. Mayernick, and M.J. Janik, Periodic trends of oxygen vacancy formation and C–H bond activation over transition metal-doped CeO2 (111) surfaces. Journal of Catalysis, 2012. 293: p. 103-115.

217. Kumar, G., et al., Correlation of Methane Activation and Oxide Catalyst Reducibility and Its Implications for Oxidative Coupling. ACS Catalysis, 2016. 6(3): p. 1812-1821.

218. Jiang, B., et al., Hydrogen generation from chemical looping reforming of glycerol by Ce-doped nickel phyllosilicate nanotube oxygen carriers. Fuel, 2018. 222: p. 185-192.

219. Hinuma, Y., et al., Density Functional Theory Calculations of Oxygen Vacancy Formation and Subsequent Molecular Adsorption on Oxide Surfaces. The Journal of Physical Chemistry C, 2018. 122(51): p. 29435-29444.

220. Scheiber, P., et al., (Sub)Surface Mobility of Oxygen Vacancies at the ${\mathrm{TiO}}_{2}$ Anatase (101) Surface. Physical Review Letters, 2012. 109(13): p. 136103.

221. Huygh, S., A. Bogaerts, and E.C. Neyts, How Oxygen Vacancies Activate CO2Dissociation on TiO2Anatase (001). The Journal of Physical Chemistry C, 2016. 120(38): p. 21659-21669.

222. Han, B., et al., Strong Metal-Support Interactions between Pt Single Atoms and TiO2. Angew Chem Int Ed Engl, 2020.

223. Tracey van Heerden, a.E.v.S., Metal support interaction on cobalt based FT catalysts - a DFT study of model inverse catalysts. The royal society of chemistry, 2016: p. 1-7.

224. S. J. Tauster, S.C.F., and R. L. Garten, Strong Metal-Support Interactions. Group 8 Noble Metals Supported on Ti02. Journal of the American Chemical Society, 1978. 100(1): p. 170-175.

225. K. Liu, X.Z., G. Ren, T. Yang, Y. Ren, A. F. Lee, Y. Su, X. Pan, J. Zhang, Z. Chen, J. Yang, X. Liu, T. Zhou, W. Xi, J. Luo, C. Zeng, H. Matsumoto, W. Liu, Q. Jiang, K. Wilson, A. Wang, B. Qiao, W. Li, and T. Zhang, Strong metal-support interaction promoted scalable production of thermally stable single-atom catalysts. Nature Communications, 2020. 11 (1).

226. al., C.-J.P.e., Tuning/exploiting Strong Metal-Support Interaction (SMSI) in Heterogeneous Catalysis. Journal of the Taiwan Institute of Chemical Engineers, 2017: p. 1–33.

227. Akri, M., et al., Atomically dispersed nickel as coke-resistant active sites for methane dry reforming. Nat Commun, 2019. 10(1): p. 5181.

228. K. Nagaoka, M.O.a.K.-i.A., Titani supported rethenium as a coking-resistant catalyst for hight pressure dry reforming of methane. Catal. Commun., 2001. 2: p. 255–260.

229. McKenzie P. Kohn a, M.J.C., Robert J. Farrauto, Auto-thermal and dry reforming of landfill gas over a Rh/gAl2O3 monolith catalyst. Applied Catalysis B: Environmental, 2010. 94: p. 125–133.

227. Tracey van Heerden, e.a., Metal support interaction on cobalt based FT catalysts - a DFT study of model inverse catalysts. The royal Society of Chemistry, 2016: p. 1-7.

228. Valentina Perazzolo, e.a., DFT and Experimental Evidences of Metal-Support Interaction in Pt Nanoparticles supported on Nitrogen and Sulfur Doped Mesoporous Carbons: Synthesis, Activity and Stability. ACS Catal.

229. Shi-Tong Zhang, e.a., Density Functional Theory Study on the Metal–Support Interaction between Ru Cluster and Anatase TiO2(101) Surface. J. Phys. Chem. , 2014. 118: p. 3514–3522.

230. Jingde Li, e.a., Effect of Metal–Support Interface During CH4 and H2 Dissociation on Ni/γ-Al2O3: A Density Functional Theory Study. J. Phys. Chem., 2013. 117: p. 16907–16920.

231. Abdulrasheed, A., et al., A review on catalyst development for dry reforming of methane to syngas: Recent advances. Renewable and Sustainable Energy Reviews, 2019. 108: p. 175-193.

232. Roduner, E., Metal–Support Interaction for Metal Clusters in Oxides. Encyclopedia of Interfacial Chemistry, 2018: p. 520–526.

233. Zhang, M., et al., DFT study on the structure of Ni/α-Al2O3 catalysts. Applied Surface Science, 2013. 287: p. 97-107.

234. Hong, J., et al., Tuning the Metal–Support Interaction and Enhancing the Stability of Titania-Supported Cobalt Fischer–Tropsch Catalysts via Carbon Nitride Coating. ACS Catalysis, 2020. 10(10): p. 5554-5566.

235. Ji, W., et al., Strategy for stabilizing noble metal nanoparticles without sacrificing active sites. Chemical Communications, 2019. 55(48): p. 6846-6849.

236. van Deelen, T.W., C.H. Mejía, and K.P. de Jong, Control of metal-support interactions in heterogeneous catalysts to enhance activity and selectivity. Nature Catalysis, 2019. 2(11): p. 955-970.

237. Wu, P., et al., Harnessing strong metal–support interactions via a reverse route. Nature Communications, 2020. 11(1): p. 3042.

238. Mao, Z., et al., Ni Nanoparticles on CeO2(111): Energetics, Electron Transfer, and Structure by Ni Adsorption Calorimetry, Spectroscopies, and Density Functional Theory. ACS Catalysis, 2020. 10(9): p. 5101-5114.

239. Lustemberg, P.G., et al., Room-Temperature Activation of Methane and Dry Re-forming with CO2 on Ni-CeO2(111) Surfaces: Effect of Ce3+ Sites and Metal–Support Interactions on C–H Bond Cleavage. ACS Catalysis, 2016. 6(12): p. 8184-8191.

240. Han, Z.-K., et al., Unraveling the oxygen vacancy structures at the reduced $\mathrm{Ce}{\mathrm{O}}_{2}(111)$ surface. Physical Review Materials, 2018. 2(3): p. 035802.

241. Lustemberg, P.G., et al., Direct conversion of methane to methanol on Ni-Ceria surfaces: metal–support interactions and water-enabled catalytic conversion by site blocking. Journal of the American Chemical Society, 2018. 140(24): p. 7681-7687.

242. Wittich, K., et al., Catalytic Dry Reforming of Methane: Insights from Model Systems. ChemCatChem, 2020. 12(8): p. 2130-2147.

243. Tao, M., et al., Enhanced sintering resistance of bimetal/SBA-15 catalysts with promising activity under a low temperature for CO methanation. RSC Advances, 2020. 10(35): p. 20852-20861.

244. Rahmati, M., et al., Chemical and Thermal Sintering of Supported Metals with Emphasis on Cobalt Catalysts During Fischer-Tropsch Synthesis. Chem Rev, 2020. 120(10): p. 4455-4533.

245. Waldow, S.P. and R.A. De Souza, Is excess faster than deficient? A molecular-dynamics study of oxygen-interstitial and oxygen-vacancy diffusion in CeO2. Journal of Physics: Energy, 2020. 2(2): p. 024001.

246. Tsakoumis, N.E., et al., Deactivation of cobalt based Fischer–Tropsch catalysts: A review. Catalysis Today, 2010. 154(3-4): p. 162-182.

247. He, D., et al., Understanding the catalytic acceleration effect of steam on CaCO3 decomposition by density function theory. Chemical Engineering Journal, 2020. 379: p. 122348.

248. Goodman, E.D., et al., Supported Catalyst Deactivation by Decomposition into Single Atoms Is Suppressed by Increasing Metal Loading. Nat Catal, 2019. 2.

249. Bayram, E., et al., Agglomerative Sintering of an Atomically Dispersed Ir1/Zeolite Y Catalyst: Compelling Evidence Against Ostwald Ripening but for Bimolecular and Autocatalytic Agglomeration Catalyst Sintering Steps. ACS Catalysis, 2015. 5(6): p. 3514-3527.

250. Mette, K., et al., High-Temperature Stable Ni Nanoparticles for the Dry Reforming of Methane. ACS Catalysis, 2016. 6(10): p. 7238-7248.

251. Li, Z., et al., Design of highly stable and selective core/yolk–shell nanocatalysts—A review. Applied Catalysis B: Environmental, 2016. 188: p. 324-341.

252. H. A. Alarifi, M.A., C. Özdoğan3,A.Hu, M. Yavuz and Y. Zhou, Molecular Dynamics Simulation of Sintering and Surface Premelting of Silver Nanoparticles. Materials Transactions, 2013. 54: p. 884 - 889.

253. Zhao, H., et al., Molecular Dynamics Simulation of the Microscopic Sintering Process of CuO Nanograins Inside an Oxygen Carrier Particle. The Journal of Physical Chemistry C, 2018. 122(44): p. 25595-25605.

254. Xu, J., et al., Molecular dynamics simulation of Ni nanoparticles sintering process in Ni/YSZ multi-nanoparticle system. The Journal of Physical Chemistry C, 2013. 117(19): p. 9663-9672.

255. Henz, B.J., T. Hawa, and M. Zachariah, Molecular dynamics simulation of the kinetic sintering of Ni and Al nanoparticles. Molecular Simulation, 2009. 35(10-11): p. 804-811.

256. Chizallet, C. and P. Raybaud, Density functional theory simulations of complex catalytic materials in reactive environments: beyond the ideal surface at low coverage. Catal. Sci. Technol., 2014. 4(9): p. 2797-2813.

257. Chen, B.W., L. Xu, and M. Mavrikakis, Computational methods in heterogeneous catalysis. Chemical Reviews, 2020. 121(2): p. 1007-1048.

258. Witman, M., et al., Cutting materials in half: A graph theory approach for generating crystal surfaces and its prediction of 2D zeolites. ACS central science, 2018. 4(2): p. 235-245.

259. Sun, W. and G. Ceder, Efficient creation and convergence of surface slabs. Surface Science, 2013. 617: p. 53-59.

260. Wellendorff, J., et al., A benchmark database for adsorption bond energies to transition metal surfaces and comparison to selected DFT functionals. Surface Science, 2015. 640: p. 36-44.

261. Mallikarjun Sharada, S., et al., Sbh10: A benchmark database of barrier heights on transition metal surfaces. The Journal of Physical Chemistry C, 2017. 121(36): p. 19807-19815.

262. Ganduglia-Pirovano, M.V., The non-innocent role of cerium oxide in heterogeneous catalysis: a theoretical perspective. Catalysis Today, 2015. 253: p. 20-32.

263. Miran, H.A., et al., An Insight into Geometries and Catalytic Applications of CeO2 from a DFT Outlook. Molecules, 2021. 26(21): p. 6485.

264. Plata, J.J., A.M. Márquez, and J.F. Sanz, Communication: Improving the density functional theory+U description of CeO2 by including the contribution of the O 2p electrons. The Journal of Chemical Physics, 2012. 136(4): p. 041101.

265. Henderson, M.A., et al., Redox properties of water on the oxidized and reduced surfaces of CeO2(111). Surface Science, 2003. 526(1): p. 1-18.

266. Ozório, M.S., K.F. Andriani, and J.L.F. Da Silva, A hybrid-DFT investigation of the Ce oxidation state upon adsorption of F, Na, Ni, Pd and Pt on the (CeO2)6 cluster. Physical Chemistry Chemical Physics, 2020. 22(25): p. 14099-14108.

267. Lustemberg, P.G., et al., Vibrational Frequencies of Cerium-Oxide-Bound CO: A Challenge for Conventional DFT Methods. Physical Review Letters, 2020. 125(25): p. 256101.

268. Fabris, S., et al., Electronic and atomistic structures of clean and reduced ceria surfaces. The Journal of Physical Chemistry B, 2005. 109(48): p. 22860-22867.

269. Galea, N.M., et al., A GGA+U study of the reduction of ceria surfaces and their partial reoxidation through NO2 adsorption. Molecular Simulation, 2009. 35(7): p. 577-583.

270. Bennett, L.J. and G. Jones, The influence of the Hubbard U parameter in simulating the catalytic behaviour of cerium oxide. Physical Chemistry Chemical Physics, 2014. 16(39): p. 21032-21038.

271. , M. and T. Ziegler, The Electronic Structure and Chemical Properties of a Ni/CeO2 Anode in a Solid Oxide Fuel Cell: A DFT + U Study. The Journal of Physical Chemistry C, 2010. 114(49): v p. 21411-21416.

272. Rohrbach, A., J. Hafner, and G. Kresse, Molecular adsorption on the surface of strongly correlated transition-metal oxides: A case study for CO/NiO(100). Physical Review B, 2004. 69(7): p. 075413.

273. Heyd, J., G.E. Scuseria, and M. Ernzerhof, Hybrid functionals based on a screened Coulomb potential. The Journal of chemical physics, 2003. 118(18): p. 8207-8215.

274. Lutfalla, S., V. Shapovalov, and A.T. Bell, Calibration of the DFT/GGA+U Method for Determination of Reduction Energies for Transition and Rare Earth Metal Oxides of Ti, V, Mo, and Ce. Journal of Chemical Theory and Computation, 2011. 7(7): p. 2218-2223.

275. Salcedo, A. and B. Irigoyen, DFT insights into structural effects of Ni–Cu/CeO2 catalysts for CO selective reaction towards water–gas shift. Physical Chemistry Chemical Physics, 2021. 23(6): p. 3826-3836.

276. Xiao, Z., et al., Boosting hydrogen production from steam reforming of ethanol on nickel by lanthanum doped ceria. Applied Catalysis B: Environmental, 2021. 286: p. 119884.

277. Jiang, Y., et al., Hydrogen Oxidation Pathway Over Ni–Ceria Electrode: Combined Study of DFT and Experiment. Frontiers in Chemistry, 2021. 8(1116).

278. Ebnesajjad, S., Surface Treatment and Bonding of Ceramics. 2014: p. 283-299.

279. perathoner, G.c.a.S., adsorption and reactivity of NO on copper-on-alumina catalysts. journal of catalysts, 1995. 152: p. 93-102.

280. Lana, I.G.D., "Applied heterogeneous catalysis, by J.-F. Le Page eta al. institut Français du Petrole, 515 pages, 1987, edition: Technip, paris isbn 2-7108-0531-6. price: 825 french francs,". The Canadian Journal of Chemical Engineering, 1988. 66(6).

281. Knözinger, H. and P. Ratnasamy, Catalytic Aluminas: Surface Models and Characterization of Surface Sites. Catalysis Reviews, 1978. 17(1): p. 31-70.

282. Chuang, Q.Z.a.K.T., Alumina-Supported Noble Metal Catalysts for Destructive Oxidation of Organic Pollutants in Effluent from a Softwood Kraft Pulp Mill. Ind. Eng. Chem. Res., 1998. 37: p. 3343-3349.

283. Gu, Y.-Q., et al., Transition metal nanoparticles dispersed in an alumina matrix as active and stable catalysts for COx-free hydrogen production from ammonia. Journal of Materials Chemistry A, 2015. 3(33): p. 17172-17180.

284. Valand, J., et al., Transition metal oxide supported on alumina catalysts: a comparative study for the hydrogenation of octanal. South African Journal of Chemistry, 2018. 71: p. 135-139.

285. H. C. Stu31pf. Allen S. Russell, J.W.N.I., And C. 31. Tucker, Thermal Transfo ations of Aluminas and Alumina Hydrates. INDUSTRIAL AND ENGINEERING CHEMISTRY, 1950. 42(7): p. 1398-1403.

286. P. Souza Santos, H.S.S.P.T., Standard Transition Aluminas. Electron Microscopy Studies. Materials Research, , 2000. 3: p. 104-114.

287. γ-Alumina, T.S.o.t.D.P.o.B.t., Xe nophon Krokidis, Pascal Raybaud, Anne-Elisabeth Gobichon, Bernadette Rebours, Patrick Euzen and Herve Toulhoat. J. Phys. Chem. B, 2001. 105: p. 5121-5130.

288. Nachtigall, P. and C.O. Arean, Themed Issue on characterization of adsorbed species. Phys Chem Chem Phys, 2010. 12(24): p. 6307-8.

289. Turlier, P., et al., Influence of the nature of the support on the reducibility and catalytic properties of nickel: evidence for a new type of metal support interaction. Applied catalysis, 1985. 19(2): p. 287-300.

290. Digne, M., et al., Hydroxyl Groups on γ-Alumina Surfaces: A DFT Study. Journal of Catalysis, 2002. 211(1): p. 1-5.

291. Digne, M., Use of DFT to achieve a rational understanding of acid?basic properties of ?-alumina surfaces. Journal of Catalysis, 2004. 226(1): p. 54-68.

292. Varghese, J.J. and S.H. Mushrif, Insights into the C–H Bond Activation on NiO Surfaces: The Role of Nickel and Oxygen Vacancies and of Low Valent Dopants on the Reactivity and Energetics. The Journal of Physical Chemistry C, 2017. 121(33): p. 17969-17981.

293. Gu, J., J. Wang, and J. Leszczynski, Structure and Energetics of (111) Surface of gamma-Al2O3: Insights from DFT Including Periodic Boundary Approach. ACS Omega, 2018. 3(2): p. 1881-1888.

294. Fitzgerald, J.J., et al., Dehydration Studies of a High-Surface-Area Alumina (Pseudo-boehmite) Using Solid-State1H and27Al NMR. Journal of the American Chemical Society, 1997. 119(33): p. 7832-7842.

295. Raybaud, P., et al., Morphology and Surface Properties of Boehmite (γ-AlOOH): A Density Functional Theory Study. Journal of Catalysis, 2001. 201(2): p. 236-246.

296. J. H. De Boer, J.M.H.F., ' B. C. Lippens, And W. H. Meijs, Study of the (Nature of Surfaces with Polar Molecules of Water on Aluminas The Adsorption. journal of catalysis, 1963. 2: p. 1-7.

297. FILIMONOV, A.A.T.a.V.N., INFRARED SPECTRA OF SURFACE HYDROXYL GROUPS AND CRYSTALLINE STRUCTURE OF OXIDES. Joumal of Molecular Struciure,. 19: p. 579-589.

298. Ching, W.Y., et al., Ab initiostudy of the physical properties ofγ-Al2O3: Lattice dynamics, bulk properties, electronic structure, bonding, optical properties, and ELNES/XANES spectra. Physical Review B, 2008. 78(1).

299. Loyola, C., E. Menéndez-Proupin, and G. Gutiérrez, Atomistic study of vibrational properties of γ-Al2O3. Journal of Materials Science, 2010. 45(18): p. 5094-5100.

300. Paglia, G., et al., Determination of the structure ofγ-alumina from interatomic potential and first-principles calculations: The requirement of significant numbers of nonspinel positions to achieve an accurate structural model. Physical Review B, 2005. 71(22).

301. Menéndez-Proupin, E. and G. Gutiérrez, Electronic properties of bulkγ−Al2O3. Physical Review B, 2005. 72(3).

302. Wolverton, C. and K.C. Hass, Phase stability and structure of spinel-based transition aluminas. Physical Review B, 2000. 63(2).

303. Peri, J.B., A Model for the Surface of gamma-Alumina. The Journal of Physical Chemistry 1965. 69: p. 220-230.

304. Gianluca Paglia, C.E.B., Andrew L. Rohl, Robert D. Hart, Kartsen Winter, Andrew J. Studer, Brett A. Hunter,and John V. Hanna, Boehmite Derived γ-Alumina System. 1. Structural Evolution with Temperature, with the Identification and Structural Determination of a New Transition Phase, γ′-Alumina. Chem. Mater., 2004. 16: p. 220-236.

305. Dong, J., et al., Hydrogenous spinel gamma-alumina structure. Phys Chem Chem Phys, 2017. 19(40): p. 27389-27396.

306. F. A. Cotton, E., "Progress in Inorganic Chemistry," Progress in Inorganic Chemistry. jan.1996.

307. H. Krebs, Fundamentals of Inorganic Crystal Chemistry, McGraw-Hill, London, . 1968. .

308. Wischert, R., et al., gamma-Alumina: the essential and unexpected role of water for the structure, stability, and reactivity of "defect" sites. J Am Chem Soc, 2012. 134(35): p. 14430-49.

309. José J. Fripiat, L.J.A., Jorge Sánchez Sánchez,Evangelina Mart´ınez Morales, José M. Saniger , Norma Angélica Sánchez, Simulation of the infrared spectra of transition aluminas from direct measurement of Al coordination and molecular dynamics. Applied Catalysis A: General, 2001. 215: p. 91–100.

310. Beaufils, J.P., and Barbaux, Y.,, J. Chim. Phys. , (1981). 78, 347

311. Kwak, J.H., et al., (100) facets of γ-Al2O3: The Active Surfaces for Alcohol Dehydration Reactions. Catalysis Letters, 2011. 141(5): p. 649-655.

312. Liu, Z., et al., The effect of γ-Al2O3 surface hydroxylation on the stability and nucleation of Ni in Ni/γ-Al2O3 catalyst: a theoretical study. RSC Advances, 2014. 4(26): p. 13280.

313. Yunxiang Pan, ‡ Chang-jun Liu,*,‡ and Qingfeng Ge, Adsorption and Protonation of CO2 on Partially Hydroxylated γ-Al2O3 Surfaces: A Density

Functional Theory Study. American Chemical Society, 2008. 24: p. 12410-12419.

314.   Andrei Ionescu, A.A., Jean-Pierre Aycard, and Michel Rajzmann, Study of γ-Alumina Surface Reactivity: Adsorption of Water and Hydrogen Sulfide on Octahedral Aluminum Sites. J. Phys. Chem. B, 2002. 106: p. 9359-9366.

315.   Hu, C.H., et al., Modulation of catalyst particle structure upon support hydroxylation: Ab initio insights into Pd13 and Pt13/γ-Al2O3. Journal of Catalysis, 2010. 274(1): p. 99-110.

316.   Le6n, L.J.A.a.L.E., Computer Simulation of y-Al2O3 Microcrystal. J. Phys. Chem. B, 1995. 99: p. 17872-17876.

317.   Arrouvel, C., et al., Effects of morphology on surface hydroxyl concentration: a DFT comparison of anatase–TiO2 and γ-alumina catalytic supports. Journal of Catalysis, 2004. 222(1): p. 152-166.

318.   R. Wischert, C.C., F. Delbecq, and P. Sautet, Optimal Water Coverage on Alumina: AKey to Generate Lewis Acid– Base Pairs that are Reactive Towards the C H Bond Activation of Methane. Angewandte Chemie International Edition, 2011. 50: p. 3202–3205.

319.   Batista, A.T.F., et al., Beyond γ-Al2O3 crystallite surfaces: The hidden features of edges revealed by solid-state 1H NMR and DFT calculations. Journal of Catalysis, 2019. 378: p. 140-143.

320.   Roy, G. and A.P. Chattopadhyay, Dissociation of methane on Ni4 cluster-A DFT study. Computational and Theoretical Chemistry, 2017. 1106: p. 7-14.

321.   Rodríguez-Kessler, P.L. and A.R. Rodríguez-Domínguez, Stability of Ni Clusters and the Adsorption of CH4: First-Principles Calculations. The Journal of Physical Chemistry C, 2015. 119(22): p. 12378-12384.

322.   Andriani, K.F., J. Mucelini, and J.L.F. Da Silva, Methane dehydrogenation on 3d 13-atom transition-metal clusters: A density functional theory investigation combined with Spearman rank correlation analysis. Fuel, 2020. 275: p. 117790.

323.   Silaghi, M.-C., A. Comas-Vives, and C. Copéret, CO2 Activation on Ni/γ–Al2O3 Catalysts by First-Principles Calculations: From Ideal Surfaces to Supported Nanoparticles. ACS Catalysis, 2016. 6(7): p. 4501-4505.

324.   Zhang, L., et al., Theoretical investigation onto the reaction mechanism of dry reforming of methane on core–shell Cu-Ni-Pt ternary alloy clusters. Chemical Physics Letters, 2021. 781: p. 138975.

325.   Chen, S., X. Chen, and H. Zhang, Probing the activity of Ni13, Cu13, and Ni12Cu clusters towards the ammonia decomposition reaction by density functional theory. Journal of Materials Science, 2017. 52(6): p. 3162-3168.

326.   Roy, G. and A.P. Chattopadhyay, Methane Dissociation on Bimetallic AuNi3, Au2Ni2 and Au3Ni Clusters-A DFT Study. ChemistrySelect, 2018. 3(11): p. 3133-3140.

327.   Li, M.-R., Z. Lu, and G.-C. Wang, The effect of potassium on steam-methane reforming on the Ni4/Al2O3 surface: a DFT study. Catalysis Science & Technology, 2017. 7(16): p. 3613-3625.

328.   Zhang, M., Y. Yu, and Y. Zhang, DFT research of methane preliminary dissociation on aluminum catalyst. Applied Surface Science, 2013. 280: p. 15-24.

329. Wang, Y., et al., Mechanism of CO methanation on the Ni4/γ-Al2O3 and Ni3Fe/γ-Al2O3 catalysts: A density functional theory study. International Journal of Hydrogen Energy, 2015. 40(29): p. 8864-8876.

330. Ray, K. and G. Deo, A potential descriptor for the CO2 hydrogenation to CH4 over Al2O3 supported Ni and Ni-based alloy catalysts. Applied Catalysis B: Environmental, 2017. 218: p. 525-537.

331. Briquet, L.G.V., C.R.A. Catlow, and S.A. French, Structure and Reactivity of Aluminum Oxide Supported Nickel Clusters. The Journal of Physical Chemistry C, 2010. 114(50): p. 22155-22158.

332. Liu, Z., et al., The effect of γ-Al2O3 surface hydroxylation on the stability and nucleation of Ni in Ni/γ-Al2O3 catalyst: a theoretical study. RSC Advances, 2014. 4(26): p. 13280-13292.

333. Salaeh, R., et al., The Role of Metal Species on Aldehyde Hydrogenation over Co13 and Ni13 Supported on γ-Al2O3(110) Surfaces: A Theoretical Study. ChemistrySelect, 2020. 5(13): p. 4058-4068.

334. Akri, M., et al., Atomically dispersed nickel as coke-resistant active sites for methane dry reforming. Nature Communications, 2019. 10(1): p. 5181.

335. Tian, D., et al., DFT insights into oxygen vacancy formation and CH4 activation over CeO2 surfaces modified by transition metals (Fe, Co and Ni). Physical Chemistry Chemical Physics, 2018. 20(17): p. 11912-11929.

336. Prasetyo, N. and H.R. Wicaksono, Effect of Pt cluster size on CO2 adsorption and activation on (110) and (100) γ-alumina surfaces: insights from DFT using a periodic boundary approach. Journal of Molecular Modeling, 2022. 28.

337. Salcedo, A., et al., Reaction Pathway for Coke-Free Methane Steam Reforming on a Ni/CeO2 Catalyst: Active Sites and the Role of Metal–Support Interactions. ACS Catalysis, 2021. 11(13): p. 8327-8337.

338. ZHI Cuimei, Z.R., LING Lixia, WANG Baojun, Insight into the Effect of Particle Sizes for Ni Clusters Supported on ZrO2(111) During CO Methanation:A DFT Study*. http://ebcc.tyut.edu.cn/mtzhwx/2017/201704/%E7%85%A4%E7%82%AD%E8%BD%AC%E5%8C%96201704007.html, 2017.

339. Yang, W., et al., First principles study on methane reforming over Ni/TiO2(110) surface in solid oxide fuel cells under dry and wet atmospheres. Science China Materials, 2020. 63(3): p. 364-374.

340. Guo, Y., J. Feng, and W. Li, Effect of the Ni size on CH4/CO2 reforming over Ni/MgO catalyst: A DFT study. Chinese Journal of Chemical Engineering, 2017. 25(10): p. 1442-1448.

341. Zhang, Y. and G.-C. Wang, Significant Effect of Rh on the h-BN-Supported Ni Catalyst for Dry Reformation of CH4: Insights from Density Functional Theory and Microkinetic Analysis. The Journal of Physical Chemistry C, 2021. 125(48): p. 26530-26541.

342. Akça, A., CH4 dissociation on the Pd/Cu(111) surface alloy: A DFT study. Open Physics, 2020. 18(1): p. 790-798.

343. Li, H., et al., Co and Ni Incorporated γ-Al2O3 (110) Surface: A Density Functional Theory Study. Catalysts, 2022. 12(2): p. 111.

344. Zhang, H., et al., Combined Density Functional Theory and Reduction Kinetics Investigation of Enhanced Adsorption of Hydrogen onto Fe2O3 by Surface Modification with Nickel. Metals, 2019. 9(12): p. 1292.

345. Yang, N., et al., Sintering Activated Atomic Palladium Catalysts with High-Temperature Tolerance of ~1,000°C. Cell Reports Physical Science, 2021. 2(1): p. 100287.

346. Prats, H., et al., Room Temperature Methane Capture and Activation by Ni Clusters Supported on TiC(001): Effects of Metal–Carbide Interactions on the Cleavage of the C–H Bond. Journal of the American Chemical Society, 2019. 141(13): p. 5303-5313.

347. Li, K., et al., Interaction between bimetal cluster Ni2Co2 and MgO and its effect on H adsorption and H_2 dissociation: A DFT study. Applied Surface Science, 2016. 390: p. 7-16.

348. Hao, X., et al., The adsorption and dissociation of methane on cobalt surfaces: thermochemistry and reaction barriers. RSC Advances, 2014. 4(81): p. 43004-43011.

349. Wong, Y., et al., Dry Reforming of Methane on Cobalt Catalysts: DFT-Based Insights into Carbon Deposition Versus Removal. The Journal of Physical Chemistry C, 2021. 125(40): p. 21902-21913.

350. Tu, W., et al., Consequences of Surface Oxophilicity of Ni, Ni-Co, and Co Clusters on Methane Activation. Journal of the American Chemical Society, 2017. 139(20): p. 6928-6945.

351. Chatla, A., et al., An experimental and first principles DFT investigation on the effect of Cu addition to Ni/Al2O3 catalyst for the dry reforming of methane. Applied Catalysis A: General, 2020. 602: p. 117699.

352. An, W., X.C. Zeng, and C.H. Turner, First-principles study of methane dehydrogenation on a bimetallic Cu/Ni(111) surface. The Journal of Chemical Physics, 2009. 131(17): p. 174702.

353. Huynh, H.L., et al., Promoting effect of Fe on supported Ni catalysts in CO2 methanation by in situ DRIFTS and DFT study. Journal of Catalysis, 2020. 392: p. 266-277.

354. Li, L., et al., Controlled Surface Segregation Leads to Efficient Coke-Resistant Nickel/Platinum Bimetallic Catalysts for the Dry Reforming of Methane. ChemCatChem, 2015. 7(5): p. 819-829.

355. Wang, W.-Y., et al., Dry reforming of methane on Ni(111) surface with different Mo doping ratio: DFT-assisted microkinetic study. Applied Surface Science, 2022. 581: p. 152310.

356. Yoon, Y., H. Kim, and J. Lee, Enhanced catalytic behavior of Ni alloys in steam methane reforming. Journal of Power Sources, 2017. 359: p. 450-457.

357. Fan, C., et al., Origin of synergistic effect over Ni-based bimetallic surfaces: A density functional theory study. The Journal of Chemical Physics, 2012. 137(1): p. 014703.

358. Termentzidis, K. and J. Hafner, CO adsorption on a Au/Ni(111) surface alloy-a DFT study. Journal of physics. Condensed matter : an Institute of Physics journal, 2007. 19 24: p. 246219.

359. Zhuang, Y., et al., Pt3 clusters-decorated Co@Pd and Ni@Pd model core–shell catalyst design for the oxygen reduction reaction: a DFT study. Journal of Materials Chemistry A, 2018. 6(46): p. 23326-23335.

360. Liu, H., C. You, and H. Wang, Experimental and Density Functional Theory Studies on the Zeolite-Based Fe–Ni–W Trimetallic Catalyst for High-Temperature NOx Selective Catalytic Reduction: Identification of Active Sites

Suppressing Ammonia Over-oxidation. ACS Catalysis, 2021. 11(3): p. 1189-1201.

361. Kong, F., et al., Trimetallic Pt–Pd–Ni octahedral nanocages with subnanometer thick-wall towards high oxygen reduction reaction. Nano Energy, 2019. 64: p. 103890.

362. Yang, Y., et al., Design of binary and ternary platinum shelled electrocatalysts with inexpensive metals for the oxygen reduction reaction. International Journal of Hydrogen Energy, 2016. 41(30): p. 13014-13023.

363. Kang, J., et al., First-principles database driven computational neural network approach to the discovery of active ternary nanocatalysts for oxygen reduction reaction. Physical Chemistry Chemical Physics, 2018. 20(38): p. 24539-24544.

364. M. C. Silaghi, A.C.-V., and C. Copéret, CO activation on Ni/#-AlO Catalysts by First Principles 2 2 3 Calculations: From Ideal Surfaces to Supported Nanoparticles. journal of catalysis, 2016: p. 1-6.

365. L. Foppa, T.M., S. Min Kim, C. Mueller, C. Copéret, K. Larmier, and A. Comas-Vives, Confronting the Role of Ni/AlO Interfaces in 2 3 Water-Gas Shift and Dry Reforming of Methane. J. Am. Chem. Soc., 2017.

366. C.L. Luo, The structure of small nickel clusters: Ni2–Ni19, . Modelling Simul.Mater.Sci. Eng, 2000. 8: p. 95–101.

367. W. Song, W.L., C.Z. Wang, K.M. Ho Magnetic and electronic properties of the nickel clusters Nin (n 6 30). 2011. 798: p. 41–46.

Glossary

ΔE	Reaction energy	K-S	Kohn-Sham
AlN	Aluminum nitride	LDA	Local-density approximation
B3LYP	Becke,3-parameter,Lee–Yang–Parr	LUMO	Low occupied molecular orbital
BG	Band-Gap	MD	Molecular dynamics
CMC	Crystallite migration and coalescence	mEISA	Modified evaporation-induced self-assembly
CNTs	Carbon nanotube	NCs	Nano crystals
DBD	Dielectric barrier discharge	OR	Ostwald ripening
DFT	Density functional theory	ORR	Oxygen reduction reaction
DRM	Dry reforming of methane	OVs	Oxygen vacancies
E_Δ	Chemisorption energy	PDOS	Partial density of stat
N_{E_F}	Total d-density of states	QSAR	QSAR
E_a	Activation energy	RWGS	Reverse water gas shift
E_{ads}	Adsorption energy	SACs	Single-atom catalysts
E_b	Binding energy	SISSO	Sure independence screening and sparsifying operator
E_{diss}	Dissociation energy	SIE	Self-error interaction
E_{Ovac}	Oxygen vacation energy	SMSI	Strong metal support interaction
E_{surf}	Surface energy	ToF	Turn over frequency
GGA	Generalized gradient approximation	TPR	Temperature-programmed reduction
GHGs	Greenhouse gases	TS	Transition state
HF	Hartree-Fock	U	Hubbard parameter
H-K	Hohenberg & Kohn	WMSI	Weak metal support interaction
HOMO	High occupied molecular orbital	XC	Exchange correlation
HTS	high-throughput screening	ε_d	d-band center
IEA	International Energy Agency	Φ	Work function